UNIVERSITÀ DI SIENA 1240

UNIONE EUROPEA
FSE REACT-EU

MUR
Ministero dell'Università e della Ricerca

PON
RICERCA E INNOVAZIONE
2014 - 2020

Percorso dottorale sviluppato con il sostegno finanziario del programma PON REACT-EU

Dipartimento di Ingegneria dell'Informazione e Scienze Matematiche

Dottorato in Information Engineering and Science

XXXVII° Ciclo

Coordinatore: Prof. Mauro Barni

Surface Wave-based Metasurfaces for Smart Radio Environment

Settore scientifico disciplinare: : Ingegneria

Candidato:
Talha Arshed

Talha Arshed Digitally signed by: TALHA ARSHED
Location: Siena
Date: 26/03/2025 10:58:53

Firma digitale del candidato Data

Supervisori:
Prof. Stefano Maci
Prof. Enrica Martini

Supplente:
Prof. Eva Rajo Iglesias

Esperto:
Dr. Antonio Clemente, HDR

dell'esame finale
09/04/2025

Commissione giudicatrice
Prof. Manuel Arrebola Baena
Prof. Matteo Albani
Dr. David González Ovejero, HDR

Anno accademico di conseguimento del titolo di Dottore di ricerca
2024/2025

Contents

List of Figures

List of Tables

List of Acronyms

Abbreviation	Explanation
AR	Anomalous Reflection
BC	Boundary Condition
EM	Electromagnetism
FW	Floquet Wave
GHz	Gigahertz
IIBC	Impenetrable Impedance Boundary Condition
LW	Leaky-wave
LWA	Leaky-wave Antenna
MIMO	Multiple Input Multiple Output
MOM	Method of Moment
mmWave	Millimeter Wave
MTP	Metasprism
MTS	Metasurface
OIBC	Opaque Impedance Boundary Condition
OSB	Open Stop Band
PIBC	Penetrable Impedance Boundary Condition
RIS	Reflecting Intelligent Surface
SMIS	Sinusoidally Modulated Impedance Surfaces
SPW	Space Wave
SW	Surface Wave
TE	Transverse Electric
TM	Transverse Magnetic
TRE	Transverse Resonance Equation
VR	Visible Region

Abstract

This thesis investigates the design and application of metasurfaces (MTSs) to enhance electromagnetic wave manipulation for smart radio environments (SREs). Metasurfaces, as planar equivalent of metamaterials, provide efficient, low-cost solutions for wave control, making them ideal for next-generation wireless communication. A key focus of this work is transitioning from traditional reflecting intelligent surfaces (RIS), which rely on anomalous reflection, to surface wave (SW)-based RIS (SW-RIS) leveraging a double conversion process: converting space waves (SPWs) into guided SWs and back into SPWs. This novel approach offers superior reliability, reduced losses, and enhanced control over beamforming in challenging environments and at millimeter-wave (mmWave) frequencies.

The research begins with a comprehensive analytical framework for designing modulated MTSs capable of efficiently coupling SPWs and SWs. A systematic synthesis process based on a penetrable impedance boundary condition (PIBC) model is introduced to achieve high conversion efficiency and precise control over aperture fields. This approach enables the realization of MTS devices with smooth impedance modulation profiles, ensuring practical feasibility. Subsequently, advanced design techniques are proposed to overcome limitations of canonical sinusoidal modulation, such as the open-stopband issue and inefficiencies at broadside and forward radiation angles. By incorporating higher-order harmonics into the impedance modulation, the study demonstrates improved control over desired radiation modes and suppression of unwanted higher-order modes, achieving superior performance in SW-SPW conversion.

Building on these theoretical foundations, the thesis develops MTS configurations tailored for broadband and frequency-scanning applications. A three-section MTS design— comprising receiver, transition, and transmitter sections— demonstrates effective SW propagation, dispersion management, and frequency-dependent beam steering. The proposed designs are validated through extensive full-wave simulations, showcasing their efficiency and broad angular and frequency operation ranges. Additionally, the performance of SW-based MTS is benchmarked against conventional reflector-based designs, highlighting its advantages in addressing frequency dispersion and reducing radio blind spots. The investigation also includes the impact of SW dispersion on diffraction losses in bent transition sections, further advancing the understanding

of SW-based devices.

The final phase of the study explores reconfigurable MTS-based leaky wave antennas (LWAs) for continuous beam scanning at mmWave frequencies. By integrating mushroom structures with voltage-controlled varactors, the proposed LWAs achieve tunability and suppression of open-stopband effects. A detailed analysis of opaque and transparent impedance models provides insights into their accuracy in capturing the electromagnetic behavior of the mushroom structure, guiding the design of high-performance reconfigurable antennas.

This work establishes a solid foundation for the design and deployment of MTS-based SW-RIS and reconfigurable LWAs, addressing key challenges in beamforming, dispersion management, and energy efficiency. The findings have significant implications for SREs, offering scalable solutions for enhanced wireless communication in urban and broadband environments.

Acknowledgements

I would like to express my deepest gratitude to Professor Stefano Maci for providing me with this tremendous opportunity to pursue my doctoral studies under his guidance. Learning electromagnetics under his mentorship has been a privilege.

I am profoundly thankful to Professor Enrica Martini for her patience and unwavering support throughout my PhD journey. I greatly appreciate her generosity and dedication in helping me develop the necessary skills and expertise to successfully complete this work.

I would like to express my gratitude to Ms. Liana Smaldore for her assistance with administrative tasks and for making my life easier as an international student. Similarly, I extend my heartfelt thanks to our esteemed lab technicians, Mr. Davide Rossi and Mr. Stefano Frigerio, for their valuable support.

I am grateful to my thesis reviewers, Dr. David González Ovejero and Dr. Antonio Clemente, for their thorough review, valuable feedback, and insightful suggestions that have significantly contributed to improving this thesis.

I would also like to extend my heartfelt thanks to my lab mates: Ilir, Ravi, Federico, Joaquin, Iram, Laura, Kioumars, Yanwen, Aliza, Dona, Vydehi, Iraklis, Tassos, Dayan, and Xenofon. Their emotional and technical support has been invaluable throughout my academic journey. I will always cherish the walks and heartfelt discussions after I took a break with Ilir and Ravi, moments that provided both clarity and camaraderie.

To my family in Pakistan, your enduring support and strength have been my foundation. Enduring the challenges of Hijr made my achievements possible, and I owe this accomplishment to your sacrifices. I am especially grateful to my wife for her unparalleled support and understanding throughout this journey. Without her sacrifices, completing this degree would not have been possible. I am also profoundly thankful to God for blessing me with two angels, Areeha and Muhammad Arham, who bring immense joy and purpose to my life.

Chapter 1

Introduction

To control and manipulate electromagnetic waves is the driving force behind ongoing research and development in electromagnetism. Metamaterials, which offer superior control over electromagnetic (EM) waves, play a crucial role in this pursuit. These materials are typically engineered by arranging a set of electrically small elements (such as rings, rods, or other arbitrarily shaped inclusions) in a regular array within a three-dimensional space [1,2]. This configuration results in a bulk response that exhibits extraordinary interactions with EM waves [3]. In many applications, only a planar interface with EM waves is required, leading to the development of a two-dimensional version of metamaterials known as metasurfaces [4]. Metasurfaces, characterized by their small thickness compared to the operating wavelength, offer advantages such as simplified manufacturing, lower cost, and reduced dissipation losses compared to their three-dimensional counterparts [5].

Metasurfaces differ from other composite planar devices, such as frequency selective surfaces (FSS) and electromagnetic band-gap (EBG) structures, primarily due to the non-resonant nature of their contituent elements. Specifically, the size (a) and spacing (d) of these elements are electrically small, with dimensions less than half the wavelength ($a, d < \lambda/2$) [5]. A key characteristic of metasurfaces is that when an electromagnetic wave interacts with them, the wave perceives the surface as a homogenized interface governed by boundary conditions. In essence, all detailed information about the metasurface—including the geometry of its elements, their shape, size, and material properties—is incorporated into the effective surface parameters that define these boundary conditions [6]. A powerful homogenized model is the impedance boundary condition (IBC), which establishes a relationship between the tangential electric and magnetic fields on the surface [7]. The typical design process for metasurfaces to achieve extraordinary wave control involves synthesizing an impedance boundary condition that converts a given input field into a desired output field [8].

A distinctive feature of metasurfaces is that, while the spacing of their elements (d) remains uniform, the geometry of these elements—such as their size, shape, or orientation—is non-uniform. This flexibility in element design gives rise to a major subset known as modulated metasurfaces (MM), where the geometry of the elements is modulated over a spatial period and repeats periodically [9]. To clarify the terminology, the uniform spacing of elements is referred to as the micro-period (d), whereas the spacing associated with the modulation is called the macro-period (D) [10]. Crucially, the macro-period is comparable to the operating wavelength ($D > \lambda/2$), allowing MMs to be analyzed using Floquet-Bloch theory [5, 11]. At the same time, the basic elements can still be modeled locally using boundary conditions. By leveraging this double-scale approach in MM design, many advanced devices have been developed, further

extending the potential of metasurfaces for sophisticated electromagnetic wave manipulation.

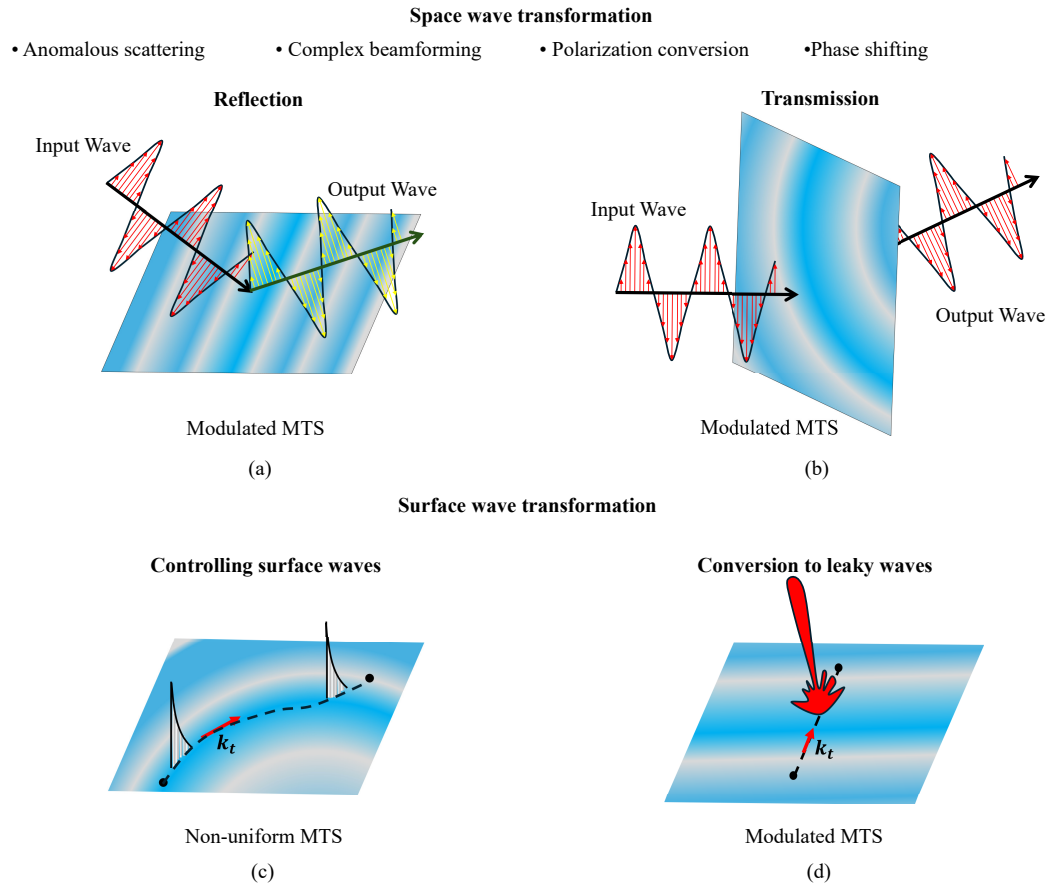

Figure 1.1: Notable wave transformation functions performed by modulated (or non-uniform) MTS: (a) reflection mode, (b) transmission mode, (c) SW routing and (d) conversion to leaky-waves.

Building on the wide range of capabilities discussed, metasurfaces enable powerful wave manipulation phenomena, as illustrated in Fig. 1.1. These phenomena span the entire electromagnetic spectrum, from high-frequency regions such as the optical [12, 13] and terahertz (THz) [14, 15] bands to the microwave range. However, the focus of this thesis is on the microwave region. For reflecting metasurfaces, the amplitude and phase of the impinging electromagnetic wave are transformed across the aperture, producing reflected waves with complex beamforms and anomalous reflection angles [16–23]. Additionally, by controlling the polarization of the field, metasurfaces can facilitate polarization conversion [24, 25]. Similarly, transmitting metasurfaces modify electromagnetic fields as waves pass through, resulting in anomalous transmission, complex beamforms, and polarization conversion [26–29]. One particularly significant phenomenon in metasurface research is the conversion of space waves (SPW) into guided waves

(or surface waves), which has gained considerable attention due to breakthroughs in achieving high conversion efficiency across the entire angular domain [30–34].

Similarly, the manipulation of surface waves (SWs) using metasurfaces has led to interesting applications. By controlling wave dispersion and anisotropy, metasurfaces can achieve spreading or focusing of the wavefront enabling the creation of planar meta-lenses [35–38]. Furthermore, conformal metasurfaces can guide waves around obstacles, presenting exciting potential for applications in both commercial communication and defense systems. While SW to SPW conversion is a well-known phenomenon in traditional leaky-wave antennas operating at microwave frequencies, metasurface-based leaky-wave structures have significantly expanded the capabilities of such systems [39]. These advancements offer improvements in gain, efficiency, complex beamforming, polarization diversity, and bandwidth [40–51]. In physical terms, this phenomenon is reciprocal to the SPW to guided-wave conversion. As metasurface technology continues to mature, the wave manipulation techniques illustrated in Fig. 1.1 have not only deepened our understanding of these interactions but also led to practical and commercial devices, marking the forefront of new developments in the field.

1.1 Motivation

1.1.1 Modulated Metasurfaces Based Reflecting Intelligent Surfaces

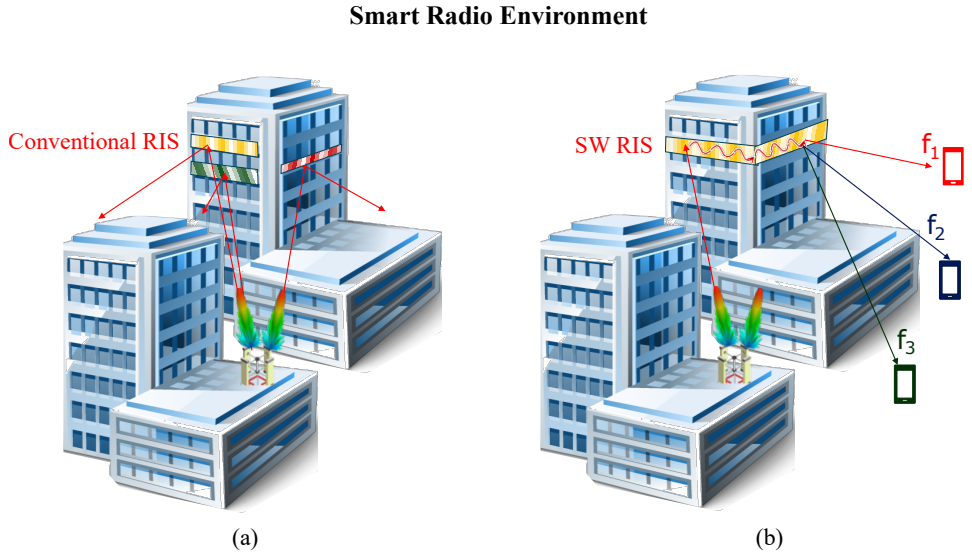

Figure 1.2: Working principle of Smart radio environment technology. (a) Conventional reflecting intelligent surface implementation. (b) Surface wave-based RIS implementation.

The development of smart radio environment (SRE) technologies is anticipated to signific-

antly enhance the overall performance of communication systems [52]. The core idea behind SRE is to tailor the communication channel (i.e., the environment) in conjunction with the design of transmitters and receivers. To this end, the concept of reflecting intelligent surfaces (RIS) has recently gained traction [53]. RIS are strategically placed on structures like buildings and billboards to redirect incoming signals, ensuring a maintained line-of-sight between the transmitter and receiver, as illustrated in Fig. 1.2. In electromagnetic terms, this "redirecting" function is an example of anomalous reflection, a process enabled by periodic MTSs. Numerous studies have explored this topic, particularly focusing on the efficiency and angular range of anomalous reflection [16–23].

Despite the advantages of MTS-based reflectors, they present several practical limitations. As reflectors, these surfaces reroute wireless signals to an opposing plane, which can create radio blind spots in certain areas of the communication environment. Additionally, the rerouted signals, remaining as unguided propagating waves, are susceptible to interference, free-space path loss, and obstructions—a concern especially pronounced in the mmWave frequency band. Frequency dispersion also has an impact on signal routing directions, as discussed in the literature [54]. While this dispersion can be leveraged for broadband applications to enable frequency division multiplexing at the physical layer, the anomalous reflection capability of MTS-RIS is intrinsically frequency-dependent due to the periodic modulation of the MTS structure.

In this context, an alternative approach involves using MTS-RIS based on a double conversion process — first, the incident space wave (SPW) is converted into a surface wave (SW), then, the SW is propagated along a desired path, and finally the SW is converted back into a radiating space wave [55, 56]. This method offers multiple advantages, as the generated surface waves can navigate bends and circumvent obstacles, enhancing communication reliability and extending coverage. Since SWs are guided, they suffer lower propagation loss and less interference compared to freely propagating SPWs. Additionally, the controlled dispersion of SWs allows for effective frequency-dependent beam-scanning of the reradiated SPW. For broadband applications, this approach can conveniently enable frequency division multiplexing at the physical layer. The double conversion process further allows precise control over the beamforming of rerouted wireless signals, making this configuration—referred to as surface-wave reflecting intelligent surfaces (SW-RIS)—highly promising for advanced communication systems.

This thesis provides a comprehensive study of MTS based SW-RIS, addressing the associated technical challenges, analytical modeling, design procedures, and numerical evaluations. Additionally, the performance of SW-RIS is compared with that of traditional reflection-based RIS, highlighting applications where the former offers superior advantages.

1.1.2 Efficient Space Wave to Surface Wave Conversion and Beamforming using Modulated Metasurfaces

The conversion between SPWs and SWs is central to the operation of the MTS technologies proposed in this thesis. Recent works highlight the potential of constant phase gradient MTSs as efficient SP-to-SW couplers [30, 31]. However, this concept can be generalized to different kinds of modulations, as suggested by the seminal theory presented by Hessel and Oliner in 1959 [57]. Their work introduced the concept that a slow wave traversing a sinusoidally modulated im-

pedance boundary can be converted into a leaky wave. It was demonstrated that when a slow wave interacts with the periodic IBC, the resulting wave behaves as a sum of infinite harmonics, known as Floquet-Wave (FW) modes. Under certain conditions, specific FW modes transition from the guided region to the visible region (VR), contributing to LW radiation. The practical realization of this theory in the form of a MTS-leaky-wave antenna (LWA) was subsequently demonstrated in 2011 [58]. Indeed, due to the small electrical dimension of their constitutive unit cells, MTSs can be conveniently modeled using a homogenized impedance boundary condition, which establishes a relation between the average tangential electric field on the MTS aperture and the average current flowing on the MTS [10].

The initial implementations of MTS-LWAs were limited to constant modulation indices and periods, resulting in a sub-optimal SW to SPW conversion efficiency. More sophisticated devices, capable of converting a cylindrical SW into a desired radiated field by employing two-dimensional impedance modulation were subsequently designed in [40–49]. In particular, [40–47] considered locally sinusoidal modulations and demonstrated that by appropriately designing the modulation index and period profiles, it becomes possible to control the leakage constant, α, and the phase constant, β, across the aperture, thus, allowing one to achieve highly efficient conversion and customized radiation patterns. In [42], the synthesis process for obtaining the target IBC profile was efficiently performed using a semi-analytical approach solving the local canonical problem through a generalization of the approach proposed in [57]. Such a process applies to circular apertures with a central probe to collect or launch the SW power [59]. However, in the context of SRE, it appears more convenient to consider rectangular apertures with 1D modulations for direct field manipulation, without antenna terminals.

The conversion of SPWs into SWs using finite MTSs with 1D modulations has been extensively investigated in the recent literature. Interestingly, for finite structures, conversion efficiency can be increased by resorting to non-strictly periodic modulations. As a matter of fact, the apparent inconsistency between the homogeneous plane wave considered in the conversion from SPW to SW and the inhomogenous plane wave arising in the conversion from SW to LW [60] is solved when one considers finite structures, for which reciprocity holds rigorously, and conversion efficiency can be unambiguously defined. Furthermore, through the use of finite MTSs with non strictly periodic modulations one can control the shape of the received/radiated beam. SW-to-SPW conversion from finite structures has been addressed in several recent papers, using predominantly numerical techniques to determine the required homogenized IBC profile [48, 61–68]. In In [62–64], a general optimization procedure was employed to determine the impedance profile able to receive/launch an arbitrarily shaped beam, demonstrating a remarkably high conversion efficiency. However, the synthesis process itself requires several hours and, due to its numerical nature, it does not provide much physical insight into the problem. Furthermore, the impedance profiles provided by this procedure exhibit fast spatial variations and assume extremes values (poles and zeros), which makes practical realization challenging. Additionally, another optimization technique, based on a surface integral formulation, was proposed in [65]. This technique exhibits good computational efficiency and can also be applied to conformal MTSs. However, similar to the previous studies, the resulting impedance profile in general exhibits quite fast spatial variations.

In this thesis, we present a quasi-analytical synthesis process for generating a practically realizable modulated impedance profile to achieve efficient conversion of a SW into a desired ra-

diated beam (or, by reciprocity, an arbitrarily shaped impinging beam into a SW) using MTSs. The impedance profile is described in closed form by a locally sinusoidal function with slowly varying modulation index and period. This non-uniform modulation approach guarantees the smoothness properties facilitating the SW-RIS practical implementation, while still offering a considerable flexibility in producing arbitrary radiating field distributions across the aperture.

1.1.3 Increasing Angular Range for Modulated Metasurface

Sinusoidally modulated impedance surfaces (SMISs) are a standard and widely used technique for designing MTS SW-SPW couplers [58]. In Chapter 2 of this thesis, we present a design technique based on SMIS to achieve an excellent SW-to-SPW conversion efficiency. Additionally, the simplicity of the sinusoidal function allows for the derivation of useful design equations. However, this approach has inherent limitations for some specific applications. In their seminal work, Hessel and Oliner noted that unwanted higher-order FW modes within the VR can significantly degrade the efficiency of SW-SPW conversion at specific forward angles. Additionally, they observed the presence of a stopband at broadside, further impacting performance. With the renewed interest in modulated IBCs driven by advances in metasurface technology, advanced modulation schemes and synthesis techniques have been developed to enhance conversion efficiency in these particular cases [33,34,62–67,69]. Expanding on the Oliner's method, in [10] the authors developed a tensor impedance model for anistropic modulated MTSs. The presented model accurately predicted the propagation characteristics for a given impedance tensor. In a more recent paper [69], the authors showed that an anisotropic sinusoidally modulated IBC offers better control as compared to its isotropic counterpart, the reason being that the tensor formulation has more independent degrees of freedom that can be exploited to achieve better performance. Specifically, they demonstrated that a properly modulated anisotropic impedance could effectively eliminate unwanted FW modes responsible for the open stopband (OSB) at broadside. Notably, each entry of the required modulated impedance tensor follows a sinusoidal function.

Exact IBC profiles for achieving perfect SW to SPW conversion, valid for all angles, were analytically derived in [33,34]. In [33], the synthesis of anisotropic tensorial impedance was considered for trasverse electric (TE)-SPW to transverse magnetic (TM)-SW conversion, achieving a remarkable 100% conversion efficiency as validated by numerical calculations and full-wave simulations. Notably, the derived impedance modulation consists of combination of sine and tangent functions. Relatedly, in [34], an isotropic impedance profile was analytically derived for perfect TM-SW to TM-SPW conversion. By employing Oliner's analysis for generalized modulation, first introduced in [70], the authors demonstrated that this impedance profile eliminates all the FW modes except those corresponding to the input SW and the radiating SPW. However, these solutions have limitations, including being unique to fixed values of the propagation constant and having extreme spatial variation in impedance values, which can limit practical implementation.

In recent impedance synthesis techniques, the challenge of SW-SPW conversion on finite MTS structures has predominantly been addressed using numerical optimization methods [62–67]. Among these, isotropic impedance-based MTSs are of particular interest, due to the easier treatment and implementation. A notable example in this class is the work in [65], which achieves

high conversion performance for both broadside and forward angles. The proposed approach offers advantages such as relative computational efficiency and compatibility with conformal structures. However, it generates impedance profiles with substantial spatial variations. Furthermore, it is worth noting that optimization-based synthesis techniques may not offer insights into the underlying physics, that are instrumental in effectively controlling the performance of the synthesized impedance.

In this thesis, we present a novel synthesis procedure for designing isotropic impedance modulation for high efficiency MTS wave-converters, with a primary focus on suppressing unwanted higher-order modes. To achieve this, we have worked with the Fourier-series formulation of the impedance modulation and derived a generalization of the Oliner's method in [57] for its analysis. This method, which is based on the Floquet-wave expansion of the fields over a modulation period of the homogenized impedance surface, allows one to calculate the complex amplitude of all the FW modes, thus, fully characterizing the SW to SPW conversion for any generalized modulated impedance. Significantly, this approach provides the necessary control over unwanted FW modes, allowing our SW-RIS to reliably receive and transmit wireless signals from virtually any angle. At the same time, it ensures a smooth and slow variation of the IBC, hus simplifying its practical implementation.

1.1.4 Controlling Surface Wave Dispersion in Modulated Metasurfaces

In antenna engineering, the conversion from guided SW to LW has recently led to a class of medium- to high-gain antennas known as modulated metasurface antennas [40–43]. The control of frequency dispersion in these antennas holds significance for two distinct applications: minimizing dispersion effects to achieve a stable beam across a desired frequency bandwidth [71–73], and, conversely, exploiting high dispersion to enable large frequency scanning [74]. In [72], a ridge gap waveguide-based LW antenna (LWA) was presented, utilizing a series of microstrip branches as phase delay lines to compensate for dispersion effects. This design demonstrated a fractional bandwidth with stable beam angle of 43%. Conversely, in another notable design [74], the LWA achieved a frequency scan of 152° within 2.2 GHz in X band (equivalent to a scanning rate of 69°/GHz). The required high dispersion was achieved through a combination of glide symmetry and a single-layer Goubau line. On the other hand, the significant control over the frequency dispersion of SWs offered by MTSs has not yet been exploited as a design tool for creating frequency dependent anomalous reflectors to be incorporated in multi-frequency communication systems.

Indeed, wave re-routing through SW-based MTSs has not been extensively investigated in the literature; exceptions include references [55, 75–77]. In these works, the proposed devices are based on three sections: a receiver, a transition, and a transmitter sections. An early design [75] demonstrated a planar MTS device intercepting a SPW impinging at 30° at one segment and transmitting another SPW at $-7.2°$ through the end segment, employing gradient surfaces for SPW-SW conversion. However, the overall re-routing efficiency achieved was limited to 10%. The work in [76] introduced an optimization approach to design impedance-modulated MTSs capable of receiving and re-transmitting Gaussian beams at desired selected

angles. Full-wave simulations of the MTS, modeled by a homogenized IBC, predicted an overall conversion efficiency close to 100%. However, the extremely rapid spatial variation in the synthesized impedance profile might hinder practical implementation. Notably, these designs focused solely on single-frequency operation rather than broadband scanning, revealing a gap in research regarding broadband applications.

An important application for SW-based MTS-RIS is the collection of impinging SPW power on one side of a building and re-routing to another shadowed side, to address radio blind spots. This concept was studied in [77] using an MTS device with a conformal transition section designed to transfer a SW around a rounded corner. The reported full-wave simulation of the structure, carried out with a homogenized IBC, demonstrated an overall transfer efficiency close to 97.5%. The adopted design procedure relied on the numerical optimization of impedance boundary conditions, and did not specifically addressed the relationship between SW dispersion and power transfer efficiency.

Unlike previous works in the literature, in this thesis we introduce a novel MTS device designed to receive a broadband wireless signal and, through double conversion, transmit it towards frequency-dependent angular directions. The latter property motivates the name "metaprism" (MTP) for our device. The focus is on manipulating and controlling the dispersion characteristics of surface waves on modulated IBCs to realize this innovative MTS device. The objective is to enable physical layer orthogonal frequency division multiplexing by properly assigning different subcarriers to various users [54].

Additionally, we propose a simple yet effective solution to extend the applicability of the proposed device to a scenario where the impinging SPW power is collected on one side of a building and must be re-routed to another shadowed side, to address radio blind spots. The design of the bent MTP is carried out by propagating the SW along a sharp corner, where power transfer efficiency is maximized by controlling the dispersion of the MTS covering the corner region

1.1.5 Accurate Design of Reconfigurable Modulated Metasurfaces

The last part of this thesis focuses on reconfigurable metasurfaces for LWA and SW-RIS applications. Reconfigurability is a critical feature for modern communication systems, enabling enhanced performance, particularly in dynamic environments. The design of modulated MTS relies on modifying the geometry of the unit cells distributed across the surface to achieve a target wave manipulation. To introduce reconfigurability, tunable elements are incorporated within each unit cell. Various practical approaches exist for electronically controlling the modulation parameters, including the integration of active devices (varactors and diodes) and the use of tunable substrates, such as liquid crystals.

In a pioneering work, Sievenpiper achieved reconfigurability in amushroom-type MTS by incorporating varactors in the gap between adjacent patches [78,79]. By controlling the capacitances of the varactors, the electromagnetic properties of the MTS unit cell, defined by equivalent IBC, were reconfigured. Importantly, the varactors were biased through the metallic vias of the mushroom structure, effectively separating the biasing layer from the top modulating layer. This technique has been used to construct tunable antennas, phase shifters, lenses, bandpass filters, and bandstop filters [80].

More recently, a similar approach has been used to construct various tunable LWAs with enhanced gain and beamforming capabilities through the use of modulated MTSs [81–84]. The designs presented in [81–84] operated below the mmWave band and did not explicitly consider the biasing vias in the design. However, at mmWave frequencies their contribution cannot be ignored.

As previously mentioned, two significant challenges in the design of modulated MTS-based LWAs are the mitigation of the open stopband (OSB) problem, that prevents radiation at broadside, and the control of higher-order modes, which can lead to the formation of undesired sidelobes when pointing to forward angles. For reconfigurable MTS LWAs, suppressing OSB is essential to achieve continuous beam scanning. Among the limited designs with continuous scanning reported in the literature, many have relied on the introduction of properly designed symmetry-breaking or reflection-canceling elements within the structure [85, 86]. However, recent studies have demonstrated the effectiveness of techniques based on a proper design of the impedance profile in suppressing OSB in static MTS LWAs [69, 87]. This approach offers the advantage of eliminating the need for an ad hoc optimization of non-radiating elements, enhancing the overall design efficiency. Furthermore, it is not restricted to broadside angles and can improve performance in forward angles as well.

For MTS antenna designs based on specific equivalent impedance profiles, the performance is critically dependent on the accuracy of the homogenized impedance model used to predict the electromagnetic behavior of the chosen implementation technology, such as microstrip patches, mushroom structures, or beds of nails. A commonly applied model relies on opaque impedance boundary conditions (OIBC), which are defined at the top layer of the MTS structure and account for the electromagnetic contributions of the entire structure. These IBCs can model arbitrary structures; at resonance, the impedance value is univocally related to the transverse wavenumber of the supported SW, which can be retrieved performing an eigenmode analysis of the unit cell with a full-wave simulator. For some configurations, particularly patches (and slots) on grounded dielectric substrates, one can also employ an alternative homogenized model, based on penetrable impedance boundary condition (PIBC). PIBC relates the tangential electric field to the discontinuity of the tangential magnetic field across the metallization, representing only the contribution of the patterned metallic layer. Notably, the impedance value of PIBC in an MTS unit cell is connected to the transverse wavenumber through the impedance (Green's functions) of the grounded slab. As shown in [10], PIBC provides more accurate predictions of leakage and phase constants in modulated MTS leaky-wave antennas (LWAs), primarily because of its ability to correctly account for the spatial dispersivity of the metasurface.

In [88], the authors derived a specific PIBC-type model for mushroom-type MTSs. The key structural difference between mushroom structures and printed patches is the presence of metallic vias. In their model, these vias in the grounded dielectric were treated as a wire medium (WM), and a corresponding homogenized impedance model was developed. This model accurately predicts the propagation constant of TM-polarized SW on uniform mushroom MTS, as well as its cut-off region. Given that reconfigurable MTS antennas are often realized using mushroom structures, it is valuable to explore the potential of the PIBC-WM model for predicting leaky-wave propagation constants in the case of modulated MTS designs.

In this thesis, we use both OIBC and PIBC-WM models, integrated with our generalized synthesis procedure, to design reconfigurable mushroom MTS LWA. Through extensive numer-

ical simulations of mushroom MTS LWAs, we compare the performance of these models across a range of wavenumbers. Based on the findings, we design a reconfigurable MTS antenna capable of scanning across a wide angular range while avoiding the loss of radiation efficiency typically occurring at broadside.

1.2 Outline of the Thesis

This first chapter has provided a brief introduction to modulated metasurfaces and outlined the main motivations and objectives of the work. The rest of this thesis is structured into four main chapters.

Chapter 2 presents an accurate analytically-based approach for the synthesis of modulated MTSs that efficiently convert an *arbitrary* impinging field into a SW with a given wavenumber, as well as convert a given SW into an *arbitrary* leaky-wave, to generate a radiating aperture field distribution with the amplitude and phase required to produce a desired radiation pattern. The considered MTSs consist of dense metallic claddings printed over a grounded dielectric slab, which are modeled through homogenized PIBC. The desired conversion is obtained through a proper locally periodic modulation of the PIBC, whose profile is designed through an effective systematic procedure based on analytical formulas. These latter are derived from the Floquet-wave expansion of fields and currents over the sinusoidally modulated impedance surface that locally matches the actual structure. This approach provides an accurate control of both amplitude and phase of the aperture field, which allows for high conversion efficiencies as well as as a general radiation pattern. Another advantage of the proposed analytically driven procedure is that it leads to impedance profiles with smooth spatial variations, which can be easily implemented through sub-wavelength patches of variable size. The effectiveness of the procedure is demonstrated by designing MTSs that couple SWs and SPWs in different scenarios. Moreover, MTSs are designed that first convert the impinging signal into a SW and then convert it back to a SPW with prescribed characteristics. This latter example can find application in future smart radio environments making it a valid alternative to reflector-RIS.

In Chapter 3, we extend the approach for the design of isotropic impedance modulated MTSs to provide enhanced control in SW to SPW conversion and vice versa. In particular, the proposed formulation aims at overcoming the limitations of sinusoidal impedance modulation, used in Chapter 2, for specific directions of the SPW (e.g. broadside radiation, exhibiting the open-stopband problem, or forward radiation angles leading to multiple Floquet modes in the visible region), while still guaranteeing a smooth impedance modulation represented through a closed-form expression. To this end, we develop a Floquet-wave theory based analytical model to describe SW-SPW conversion mechanism by any periodic impedance modulation, characterized by its Fourier-series. Through this model, we identify the limitations of the SW-SPW conversion through canonical sinusoidally modulated MTSs, especially at broadside and forward angles. Subsequently, we show how systematically adding harmonics in the modulation function of the impedance surface can provide control not only over the desired radiating mode, but also over unwanted higher-order modes, leading to improved conversion efficiency for arbitrary beam angles. Moreover, the design process allows for a flexible selection of the operating wavenumber of the SW, enabling control over MTS's dispersion and broadband performance. Subsequently,

we applied non-uniform modulation technique to our proposed functions to design finite length MTSs. Finally, the full wave analysis of a patch-based implementation of the MTS demonstrates the good performance of the proposed design technique, with an increased range of angles that the MTS can collect or radiate.

Chapter 4 presents a design technique for modulated metasurfaces, leveraging their dispersive properties to create additional functionalities. The proposed device is constituted by a passive and non-reconfigurable MTS comprising three sections. The first section (receiver) operates with low dispersion, receiving broadband signals coming from the base transceiver station (BTS) at a predefined angle and converting them into SW. The subsequent transition section gradually increases the dispersion of SW, guiding it towards the highly dispersive transmitter section, which finally converts the SW into space waves radiated towards frequency-dependent angular directions. The latter property motivates the name "metaprism" MTP. This device holds promise for enabling physical layer frequency multiplexing and addressing waves in radio blind-spots. The MTP is implemented by an array of sub-wavelength metallic patches printed on a grounded dielectric slab, initially modeled using a homogenized PIBC. The dispersion analysis of the MTS unit cell reveals the impact of patch geometry on dispersion characteristics, which is important for achieving broad scanning performance. The required conversion efficiency is obtained by accurately modulating the PIBC based on the results of Chapters 2 and 3. Full-wave simulations validate the design, demonstrating high power conversion efficiency and a reasonable frequency scan range. Moreover, the study compares the performance of SW-based MTP with that of a spatially dispersive reflecting intelligent surface (RIS), highlighting the advantages of the MTP. Additionally, it investigates an "around the corner" design, where the SW re-routes the signal around a bent transition section, shading light on the relationship between SW dispersion and power loss due to edge-diffraction.

Chapter 5 focuses on the design and numerical validation of a reconfigurable MTS-based LWA that achieves continuous angular scanning through broadside at a fixed frequency in the mmWave range. The proposed LWA uses a mushroom structure integrated with voltage-controlled varactors to achieve tunability. The mushroom configuration is chosen to ease the accommodation of biasing lines, which can be cumbersome at mmWave frequencies. The desired radiation pattern and suppression of the OSB at broadside, essential for achieving continuous beam scanning, are achieved through a proper design of the impedance modulation, as detailed in Chapter 3. Since this approach relies on a precise modeling of the equivalent impedance, we investigate two types of impedance boundary condition models —opaque and penetrable — to evaluate how accurately they can capture the electromagnetic behavior of the mushroom structure. Extensive full-wave simulations are conducted to assess the performance of these models in predicting leaky-wave properties. Based on the insights provided by this study, a reconfigurable LWA is designed and numerically analyzed, demonstrating continuous beam scanning and effective OSB suppression. The results highlight the potential of impedance-based design techniques and provide valuable insights for advancing high-performance reconfigurable antennas and SW-reflectors in mmWave systems.

Chapter 2

Direct Synthesis of Metasurfaces for Efficient Space Wave to Surface Wave Conversion and Beamforming

In this chapter [1], we propose a quasi-analytical synthesis process for generating a practically realizable modulated impedance profile to achieve efficient conversion of a SW into a desired radiated beam (or, by reciprocity, an arbitrarily shaped impinging beam into a SW) using MTSs. The impedance profile is described in closed form by a locally sinusoidal function with slowly varying modulation index and period; this approach guarantees the smoothness properties facilitating the MTS practical implementation, while still offering a considerable flexibility in producing arbitrary radiating field distributions across the aperture. For any desired field distribution, the procedure starts by defining the required profiles of the LW attenuation and phase constants; then, these profiles are converted into profiles of modulation index and period through the use of the local canonical problem of an infinite sinusoidally modulated IBC, which can be very efficiently solved numerically.

A novel contribution of this work is the derivation of accurate closed form formulas for the design parameters, modulation index m and period d, providing desired α and β values, which further speeds up the synthesis procedure. Using these formulas allows us to develop a direct synthesis procedure, thus, avoiding time consuming numerical techniques. The accuracy of the formulas is demonstrated through numerical examples. Although the idea of deriving the local modulation parameters from the analysis of the local periodic problem with 1D modulation still holds for bidimensional anisotropic modulation, as the one encountered in centrally fed metasurface antennas [41, 42], in that case the design procedure is a bit more complex, thus, not allowing for a fully analytical description.

The versatility and effectiveness of the proposed approach is verified by applying it to different waveforms for which the optimal distribution of the complex LW propagation constant can be written in closed form. By accurately defining the impedance modulation needed to match these profiles over the MTS aperture, we demonstrate SPW-to-SW conversion with an efficiency exceeding 98%. The approach is then also applied to scattering control by implementing smart anomalous reflectors able not only to deflect, but also to shape the reflected beam, similar to the ones numerically designed in [62] for impenetrable MTSs. To this end, the proposed approach

[1] This chapter has been published as "Direct Synthesis of Metasurfaces for Efficient Space- to Surface-Wave Conversion and Beamforming," in *IEEE Transactions on Antennas and Propagation* , 2024 [87].

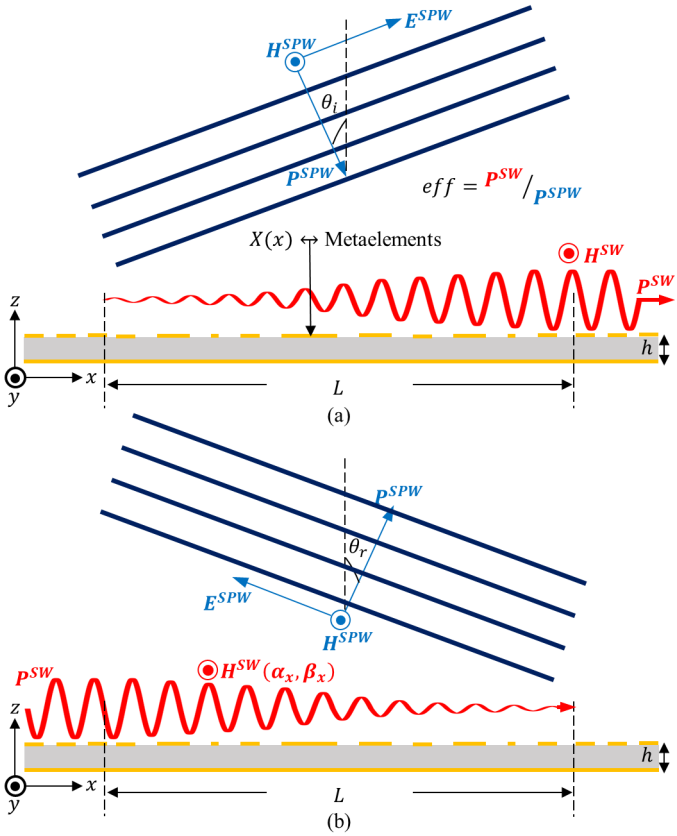

Figure 2.1: (a) Metasurface as a SPW-to-SW coupler in TM polarization. (b) Metasurface as a LW antenna fed by a TM SW.

is applied twice, to operate a double conversion. For both the applications, the practical feasibility of the design strategy is demonstrated by implementing the derived IBC profiles through electrically small patches printed on a grounded slab and performing full wave simulations of the resulting structure.

The chapter is organized as follows: Section 2.1 introduces a methodology for the effective analysis of modulated MTSs with a locally sinusoidal modulation. Section 2.2 presents a procedure for the design of efficient MTS-based SW-to-SPW and SPW-to-SW converters. Section 2.3 shows some application examples. Finally, conclusions are drawn in Section 2.4.

2.1 Analysis of Modulated MTSs

The geometry of the problem is illustrated in Fig. 2.1 for the two configurations of interest. In the first one (2.1(a)), an arbitrary electromagnetic beam impinges in the xz-plane on a MTS located in the xy-plane, and is converted into a SW. In the second one (2.1(b)) a SW propagates

along the x-axis on the same MTS, and is converted into a radiated beam with a prescribed radiation pattern. The MTS, which extends from $x = 0$ to $x = L$, consists of a layer of infinitely thin metallic elements located at $z = 0$ and is placed on a grounded dielectric slab with relative permittivity ϵ_r and thickness h. The printed elements, thanks to their small electrical dimension, are effectively replaced by their equivalent homogenized impedance during the design process. This equivalent impedance is assumed to be purely reactive, since losses are expected to be small in the microwave range, and their effect can therefore be evaluated *a posteriori* with a perturbative approach. The MTS is uniform and infinite along the y direction and finite and modulated along x. The truncation along the y direction is expected to simply provide a small perturbation of the currents at the edges.

For antenna applications, the finite structure can be fed through a beam forming network to create/receive the planar SW wavefront. As discussed in other publications from our group, the idea of deriving the local modulation parameters from the analysis of the local periodic problem with 1D modulation still holds for fully 2D anisotropic modulation, as the one encountered in centrally fed metasurface antennas. In that case, however, the design procedure is a bit more complex, thus, not allowing for a fully analytical description. On the other hand, for application to scattering control, the proposed solution allows for a seamless connection between the receiving and the transmitting parts, with no need for probes, cables and connectors, since we can assume the incident wave has a locally planar wavefront.

Without losing generality, we will consider in the following the case of transverse magnetic (TM) polarization, which is the one of the dominant mode supported by thin MTSs including a ground plane. A similar procedure can anyway be applied also to the case of transverse electric (TE) polarization, provided the MTS supports a TE SW.

The primary objective of this study is to achieve efficient conversion for the two configurations in Fig. 2.1. Since for any finite structure the two problems are equivalent by reciprocity, in the following the formulation will be presented referring to the transmission case, and its application to the SPW to SW converter will be discussed later.

2.1.1 Uniform MTS: Homogenized IBC Model and Transverse Resonance Equation

The MTS structure, as depicted in Fig. 2.2, is modeled using the homogenized penetrable impedance boundary condition (PIBC). This model establishes a relationship between the average tangential electrical field $E_t(x)$ on the MTS and the discontinuity of the average tangential magnetic field across it (or, equivalently, the current *J(x)* flowing on the metallic cladding) as follows:

$$E_x = jX(H_y|_{0^+} - H_y|_{0^-}) = jXJ \tag{2.1}$$

Here, $X(x)$ is the homogenized reactance of the penetrable MTS, which describes the EM behavior of the printed elements layer. When the reactance is uniform, i.e., $X(x)$=X_0, in the low frequency regime this structure supports a TM-polarized SW with transverse propagation constants $k_x = \beta_{SW} > k_0$, where k_0 is the free space wavenumber, and purely imaginary

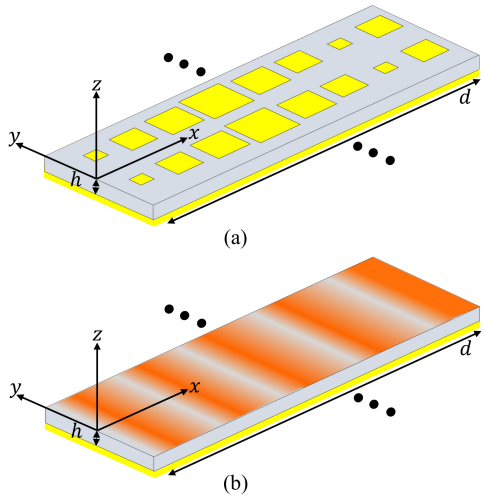

Figure 2.2: Geometry for the problem of the isotropic 1-D periodically modulated MTS. (a) Patch-type MTS and (b) its homogenized impedance version.

longitudinal propagation constant k_z. The transverse propagation constants is solution of the following transverse resonance equation:

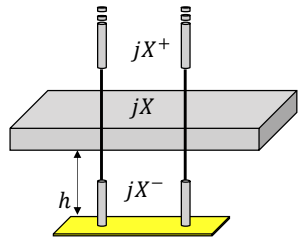

Figure 2.3: Equivalent transmission line model for patch-type MTS.

$$\frac{1}{X^+(\beta_{SW})} + \frac{1}{X^-(\beta_{SW})} + \frac{1}{X_0} = 0. \tag{2.2}$$

where $X^+(\beta_{SW})$ and $X^-(\beta_{SW})$ are the TM reactances of a z-directed transmission line toward free space and toward the ground, respectively, as shown in Fig. 2.3

$$X^+(\beta_{SW}) = -\zeta \frac{\sqrt{\beta_{SW}^2 - k_0^2}}{k_0} \tag{2.3}$$

$$X^-(\beta_{SW}) = \zeta \frac{\sqrt{\epsilon_r k_0^2 - \beta_{SW}^2}}{k_0 \epsilon_r} \tan\left(h\sqrt{\epsilon_r k_0^2 - \beta_{SW}^2}\right) \tag{2.4}$$

2.1.2 Periodically Modulated MTS: Floquet-wave Expansion

When an EM field interacts with a periodically modulated MTS it undergoes a transformation into a field comprising infinite space harmonics, known as Floquet-wave modes (FM). Electric current and field can therefore be expanded as follows:

$$J(x) = \sum_{n=-\infty}^{\infty} J^{(n)} e^{-jk_x^{(n)}x} \tag{2.5}$$

$$E_x(x) = \sum_{n=-\infty}^{\infty} E_x^{(n)} e^{-jk_x^{(n)}x} \tag{2.6}$$

where d is the modulation period, and

$$E_x^{(n)} = \frac{1}{d}\int_0^d E_x e^{jk_x^{(n)}x} dx, \quad J^{(n)} = \frac{1}{d}\int_0^d J e^{jk_x^{(n)}x} dx \tag{2.7}$$

$$k_x^{(n)} = k_x^{(0)} + \frac{2\pi}{d}n = \beta_{SW} + \Delta\beta - j\alpha_x + \frac{2\pi}{d}n \tag{2.8}$$

Conventionally, in periodic LW structures, the SW arising from the perturbation of the mode supported by the unmodulated structure is identified with the 0-indexed Floquet mode, and the modulation period is chosen so as to have (only) the -1-indexed Floquet mode associated with a LW. Accordingly, in (2.8) the phase constant of the 0-indexed Floquet mode, $\beta_x^{(0)}$, is expressed as the summation of the phase constant β_{SW} of the uniform MTS characterized by the average reactance and the term $\Delta\beta$, accounting for the perturbation induced by the modulation. By selecting appropriate values for β_{SW} and d, it is possible to achieve a -1-Floquet mode in the radiation (or SPW) region, i.e. to have $|k_x^{(-1)}| < k_0$. Under this condition, a SW launched on the structure is progressively transformed into a SPW. The leakage constant α_x, which is the same for all the Floquet modes, quantifies the relevant power conversion rate.

2.1.3 Sinusoidal Modulation: Oliner's Method

In this study, the periodic modulation will be locally sinusoidal. For this reason, the reference canonical problem is a periodic IBC, whose penetrable reactance is described by the following function:

$$X(x) = X_0\left[1 + m\cos\left(\frac{2\pi x}{d} + \psi_0\right)\right] \tag{2.9}$$

Here, X_0 represents the average reactance, m is the modulation index, d corresponds to the modulation period and ψ_0 is an arbitrary constant. These parameters are primarily associated with different physical properties: once the substrate is fixed, X_0 mainly determines the phase constant of the 0-mode $\beta_x^{(0)}$, thus governing the dispersion characteristics of the metasurface, while the modulation index m largely influences the leakage constant α_x and the correction factor $\Delta\beta$. Finally, the period d determines the radiation angle of the -1-indexed FM (or the received angle in the reciprocal problem) through the following relationship:

$$\theta^{(-1)} = \sin^{-1}\left(\frac{\beta_{SW} + \Delta\beta - \frac{2\pi}{d}}{k_0}\right) \tag{2.10}$$

A rigorous numerical approach for the solution of the canonical problem of a sinusoidally modulated impenetrable IBC was proposed in [57], and generalized to the case of a *penetrable* IBC in [89]. This approach is briefly outlined in the following; more details can be found in [10].

By combining (2.1), (2.5) and (2.9), and assuming $\psi_0 = 0$, we can express the tangential electric field $E_x(x)$ as follows:

$$E_x(x) = jX_0\left[1 + \frac{m}{2}e^{j\frac{2\pi}{d}x} + \frac{m}{2}e^{-j\frac{2\pi}{d}x}\right]\sum_{n=-\infty}^{\infty} J^{(n)}e^{-jk_x^{(n)}x} \tag{2.11}$$

On the other hand, each FM of the transverse electric field can be related to the corresponding FM of the current through the spectral Green's function (GF) of the grounded slab evaluated at the relevant transverse wavenumber $k_x^{(n)}$, thus, resulting in:

$$E_x(x) = \sum_{n=-\infty}^{\infty} E_x^{(n)}e^{-jk_x^{(n)}x} = \sum_{n=-\infty}^{\infty} jX_{GF}^{(n)}J^{(n)}e^{-jk_x^{(n)}x} \tag{2.12}$$

where:

$$X_{GF}^{(n)} = -\frac{X^+\left(k_x^{(n)}\right)X^-\left(k_x^{(n)}\right)}{X^+\left(k_x^{(n)}\right) + X^-\left(k_x^{(n)}\right)} \tag{2.13}$$

By combining equations (2.11) and (2.12) and projecting onto $e^{jq\frac{2\pi}{d}x}$ for $q = -\infty...\infty$, we obtain an infinite homogeneous system of equations where the generic q-th equation has the form:

$$\frac{m}{2}J^{(q-1)} + D^{(q)}J^{(q)} + \frac{m}{2}J^{(q+1)} = 0 \tag{2.14}$$

where

$$D^{(q)} = 1 - \frac{X_{GF}^{(q)}}{X_0} \tag{2.15}$$

The system of equations in (2.14) provides a comprehensive description of the modulated MTS, since its nontrivial solutions, which exist only when the determinant of the system matrix vanishes, correspond to the current modes supported by the structure. Hence, (2.14) establishes a univocal relationship between the modulation parameters m, d, and X_0, and the radiation characteristics β_{SW}, $\Delta\beta$, and α_x. Importantly, the infinite system can be truncated to a few terms with negligible loss of accuracy [57].

2.1.4 Constant Average Non-Uniform Modulation

In practice, in order to arbitrarily shape the radiation pattern (or to efficiently receive an arbitrary incoming field), it is necessary to change the modulation parameters across the aperture.

It is therefore important to generalize the formulation to the case of non-uniform modulation. This will allow us to achieve arbitrary α_x and β_x profiles, enabling high conversion efficiency and a versatile control of the MTS performance, as will be illustrated in the next Section.

Provided that the average reactance is kept constant and the variation of the modulation parameters is smooth, the approach described in Section 2.1.3 can still be locally applied to represent fields and currents through an adiabatic FW expansion. This approach has been successfully employed in [41] to analyze centrally fed MTS antennas. The modulation functions that will be considered in this work can be described as follows

$$X(x) = X_0 \left[1 + m(x)\cos\left(f(x)\right)\right] \tag{2.16}$$

After comparing (2.16) with (2.9) we define the local period as $d(x) = 2\pi \left(\dfrac{df}{dx}\right)^{-1}$.

Local attenuation and propagation constants can now be derived by the local modulation parameters. Then, the complex phase of the generic n-th FW can be retrieved by integrating the relevant propagation constant

$$\int_0^x k_x^{(n)}(x')dx' = \int_0^x \beta_x^{(0)}(x')dx' + \int_0^x \frac{2\pi n}{d(x')}dx' - j\int_0^x \alpha_x(x')dx' \tag{2.17}$$

The surface current along the non-uniformly modulated MTS can therefore be reconstructed as follows:

$$J(x) = \sum_{n=-N}^{N} J^{(n)}(x) e^{-j(\beta_{SW}x + f(x))} e^{-j\int_0^x \Delta\beta(x')dx'} e^{-\int_0^x \alpha_x(x')dx'} \tag{2.18}$$

Here, the coefficients $J^{(n)}(x)$ are derived from the entries of the local eigenvectors of the system in (2.14). We will demonstrate later in this paper, through a comparison with the results obtained from full-wave simulations, that, despite the local nature of the FW expansion, equation (2.18) has the capability to accurately predict the surface current behaviour across the MTS. This allows us to perform real-time performance analysis of the designed MTS.

2.2 Synthesis of Finite Length Apertures

In this section, we present a systematic and direct procedure for the synthesis of the modulated MTS providing a desired radiation pattern when excited by a SW. Based on the considerations developed in the previous section, the synthesis process consists in determining the profile of modulation index $m(x)$ and the phase function $f(x)$. By reciprocity, the same design procedure can be applied to efficiently convert to SW a given incident field by simply substituting the radiating aperture field with the projection of the impinging field over the aperture.

By applying the uniqueness theorem, the far-field radiation pattern can be uniquely determined based on the tangential field distribution over the aperture [90]. Numerous methods have been proposed in the literature to determine the aperture field that corresponds to a desired radiation pattern (see, for instance, [91]). We assume, therefore, that the objective radiating aperture field is known and represented as:

$$\boldsymbol{E}_{obj}(x) = A(x)e^{j\phi(x)}\hat{x} \tag{2.19}$$

where $A(x)$ and $\phi(x)$ are real functions, with $A(x) \geq 0$.

The key step of the synthesis procedure is the identification of this field with the -1-indexed mode of the adiabatic FW expansion (under the hypothesis that this is the only radiating FW). The amplitude and phase of this latter are determined by the distribution of the α_x and $\beta_x^{(-1)}$ constants across the aperture. In particular, the profile of α_x corresponding to a given aperture amplitude distribution of the -1 FW can be determined through the imposition of energy conservation by considering that the the radiated power must equate the power lost by the SW, as shown in the following section.

2.2.1 Derivation of Attenuation Constant Profile

The SW power flowing at the generic position x is related to the attenuation constant profile through the following integral relation

$$P_{SW}(x) = P_{SW}(0)e^{-2\int_0^x \alpha(x')dx'} \tag{2.20}$$

from which we get

$$\frac{dP_{SW}(x)}{dx} = -2\alpha(x)P_{SW}(x) \tag{2.21}$$

This quantity must be the opposite of the spatial derivative of the radiated power, which, for a unit length along y, equates the normal component of the Poynting vector of the aperture field. This latter can be estimated as follows

$$S_z(x) = \frac{A^2(x)}{2\zeta\sqrt{1-\left(\frac{1}{k_0}\frac{d\phi}{dx}\right)^2}} \tag{2.22}$$

The above formula is obtained by interpreting the gradient of the phase as the local transverse wave-vector.

Given a desired radiation efficiency e_r over an aperture length L, after integrating along x and rearranging the terms, one can derive the explicit equation of the α_x profile as a function of the objective power density distribution as

$$\alpha_x(x) = \frac{0.5S(x)}{\frac{1}{e_r}\int_0^L S(x')dx' - \int_0^x S(x')dx'} \tag{2.23}$$

From (2.23), we see that through the control of α_x we can tailor the magnitude of the radiating aperture field and match it to the one of the objective field.

2.2.2 Derivation of Phase Constant Profile

From (2.10), we observe that the tangential phase constant $\beta_x^{(-1)}$ of the -1 FW (the only mode in the visible region) is related to the local radiation angle $\theta(x)$. This latter is related to the gradient of the desired phase distribution $\phi(x)$. Using this relationship, we can express $\beta_x^{(-1)}$ as follows:

$$\beta_x^{(-1)} = k_0 \sin\left[\theta(x)\right] = -\frac{d\phi(x)}{dx} \tag{2.24}$$

Once the $\alpha(x)$ and $\beta(x)$ profiles are known, our goal is to translate them into profiles of the modulation parameters m and d. However, a significant bottleneck in the derivation of a direct synthesis procedure arises from the mathematical form of the determinantal equation for the system in (2.14), that does not allow for a direct solution. A possible approach consists in employing some iterative numerical technique to solve the resulting transcendental equation. However, it is possible to derive accurate simplified equations admitting an analytical solution. This process, which is illustrated in the next subsections, will directly provide the designer's equations for m and d.

2.2.3 Derivation of Modulation Index

A quite accurate estimate of the modulation index can be obtained assuming the presence of only one FW in the visible region, which is a standard requirement for periodic LW antennas. Under this assumption, the power radiated by the -1-mode (LW) must equate the power lost by the 0-mode (SW), being the active power carried by other higher order slow modes negligible with respect to the one carried by the dominant mode. This condition can be expressed in terms of the normal component of the relevant Poynting vectors:

$$\left|S_z^{(0)}\right| = \left|S_z^{(-1)}\right| \tag{2.25}$$

where:

$$S_z^{(n)} = -\frac{1}{2}\mathbf{Re}\left\{J^{(n)^*}E^{(n)}\right\} = -\frac{1}{2}\mathbf{Re}\left\{J^{(n)^*}X_{GF}^{(n)}J^{(n)}\right\} \tag{2.26}$$

By combining (2.25) and (2.26), we can express the ratio between the -1-mode and the 0-mode currents in terms of the problem Green's function evaluated at the relevant spectral points:

$$\frac{J^{(-1)}}{J^{(0)}} = \left|\sqrt{\frac{\mathbf{Re}\left\{X_{GF}^{(0)}\right\}}{\mathbf{Re}\left\{X_{GF}^{(-1)}\right\}}}\right| = \chi \tag{2.27}$$

Notice that in writing (2.27) we have assumed that $J^{(-1)}$ and $J^{(0)}$ are in phase, since this condition can always be obtained by properly selecting the phase ψ_0 in (2.9).

In order to find an estimate of the modulation index, we consider the equations in (2.14) for $n = -3, -2, -1$ assuming $J^{(-4)} = 0$. This latter assumption is a good approximation, thanks to the fast decay of the FW coefficients [57]. By expanding the three equations and utilizing the relationship in (2.27), we obtain a cubic equation for the modulation index m as follows:

$$\begin{aligned} 0.5m^3 + \chi\left(D^{(-1)} + D^{(-3)}\right)m^2 - 2D^{(-2)}D^{(-3)})m \\ -4\chi D^{(-1)}D^{(-2)}D^{(-3)} = 0 \end{aligned} \tag{2.28}$$

Solving (2.28) yields three complex roots for m. Among these roots, we select the one with the smallest imaginary part and a real part smaller than one; the other two have in general a non negligible imaginary part, and are therefore not consistent with the assumption made writing (2.9). Note that the variables χ and $D^{(n)}$ in (2.28) are calculated using α, $\beta_x^{(-1)}$, and β_{SW}.

The accuracy of (2.28) in predicting m for a given α will be demonstrated in the results section (2.3), by comparing these values with those obtained using the full system equation (2.14).

2.2.4 Derivation of Modulation Period

At this point in the design process, the modulation period d has been estimated by calculating the difference between $\beta_x^{(-1)}$ and β_{SW}. This is equivalent to assuming that $\beta_x^{(0)}$ is equal to β_{SW} by neglecting the perturbation term $\Delta\beta$. However, to obtain the correct value of d, we need to estimate $\Delta\beta$. In fact, although the perturbation term is small compared to $\beta_x^{(0)}$, neglecting it in the derivation of the modulation period would imply a phase error that accumulates along the wave path, finally leading to a noticeable performance degradation.

In order to estimate $\Delta\beta$, a 3×3 matrix is constructed from the equation system in (2.14) by considering three FW modes only ($n=-1,0,1$). The following equation is derived by equating the determinant of this matrix to zero:

$$D^{(-1)}D^{(0)}D^{(1)} - \frac{m^2}{4}[D^{(-1)} + D^{(-1)}] = 0 \tag{2.29}$$

Expanding $D^{(q)}$ in (2.29) in terms of Green's function X_{GF} according to (2.15) provides us:

$$\begin{aligned} -jc_1X_{GF}^{(-1)}X_{GF}^{(0)}X_{GF}^{(1)} - c_1X_0X_{GF}^{(-1)}X_{GF}^{(0)}X_{GF}^{(-1)} - c_1X_0X_{GF}^{(1)} \\ -c_1X_0X_{GF}^{(0)}X_{GF}^{(1)} + (jc_1X_0^2 - jc_2)X_{GF}^{(-1)} \\ +(jc_1X_0^2 - jc_2)X_{GF}^{(1)} + jc_1X_0^2X_{GF}^{(0)} + c_1X_0^3 - 2c_2X_0 = 0 \end{aligned} \tag{2.30}$$

where c_1 and c_2 are given in Table 2.1. In order to derive $\Delta\beta$, we expand the Green's functions in Taylor's series with respect to $\dfrac{\Delta\beta - j\alpha_x}{\beta_{SW}}$, as shown below:

$$X_{GF}^{(n)} = {c_3}^{(n)} + {c_4}^{(n)}\,(\Delta\beta - j\alpha_x) \tag{2.31}$$

Here, higher-order powers of $\dfrac{\Delta\beta - j\alpha_x}{\beta_{SW}}$ are ignored, as they are close to zero. The constants ${c_3}^{(n)}$ and ${c_4}^{(n)}$ are given in Table 2.1. By using the Taylor series expansion of $X_{GF}^{(n)}$ in (2.29) and ignoring higher-order terms, we obtain:

$$\Delta\beta = Re\left\{\frac{c_n}{c_d}\right\} \tag{2.32}$$

where c_n and c_d have a closed-form representation reported in Table 2.1. Finally, we use the above expression of $\Delta\beta$ to write the equation for d:

$$d = \frac{2\pi}{\beta_{SW} + Re\left\{\frac{c_n}{c_d}\right\} - k_0\sin\theta} \tag{2.33}$$

The accuracy of (2.33) in predicting d for given α and $\beta_x^{(-1)}$ will be demonstrated in the results Section 2.3 by comparing these values with those obtained solving numerically the determinantal equation for the full system in (2.14).

Once the local modulation parameters $m(x)$ and $d(x)$ are known, the phase function in (2.16) is retrieved by integrating equation (2.24), so as to account for the accumulation of phase along the MTS, leading to the following reactance profile

$$X(x) = X_0 \left[1 + m(x) \cos \left(\int_0^x \frac{2\pi}{d(x')} dx' \right) \right] \tag{2.34}$$

Table 2.1: Coefficients for calculating the modulation period

Coefficients	***Expressions***
c_1	$\frac{8}{m^3 X_0^3}$
c_2	$\frac{2}{mX_0}$
c_3	$-j\frac{{c_5}^{(n)}{c_6}^{(n)}\tan({c_7}^{(n)})}{{c_5}^{(n)}+{c_6}^{(n)}\tan({c_7}^{(n)})}$
c_4	$\frac{({c_5}^{(n)})\left({c_{11}}^{(n)}+{c_{10}}^{(n)}{c_8}^{(n)}\right)({c_5}^{(n)}+{c_{11}}^{(n)})-\left({c_{10}}^{(n)}{c_5}^{(n)}\right)({c_5}^{(n)}{c_8}^{(n)}+{c_{11}}^{(n)})}{({c_{10}}^{(n)}+{c_5}^{(n)})^2}$
c_5	$j\frac{\zeta_0\dot{\beta}^{(n)}}{k_0}\sqrt{\frac{k_0^2}{(\dot{\beta}^{(n)})^2}-1}$
c_6	$\frac{\zeta_0\dot{\beta}^{(n)}}{\varepsilon_r k_0}\sqrt{\frac{\varepsilon_r k_0^2}{(\dot{\beta}^{(n)})^2}-1}$
c_7	$h\dot{\beta}^{(n)}\sqrt{\frac{\varepsilon_r k_0^2}{(\dot{\beta}^{(n)})^2}-1}$
c_8	$\frac{-1}{\frac{k_0^2}{(\dot{\beta}^{(n)})^2}-1}$
c_9	$\frac{-1}{\frac{\varepsilon_r k_0^2}{(\dot{\beta}^{(n)})^2}-1}$
c_n	$jc_1{c_3}^{(-1)}{c_3}^{(0)}{c_3}^{(1)} + c_1X_0{c_3}^{(-1)}{c_3}^{(0)} + c_1X_0{c_3}^{(-1)}{c_3}^{(1)}$ $+c_1X_0{c_3}^{(0)}{c_3}^{(1)} - (jc_1X_0^2 - jc_2)\,{c_3}^{(-1)} - (jc_1X_0^2 - jc_2){c_3}^{(1)}$ $-jc_1X_0^2{c_3}^{(0)} - c_1X_0^3 + 2c_2X_0$
c_d	$-jc_1{c_3}^{(0)}{c_3}^{(1)}{c_4}^{(-1)} - jc_1{c_3}^{(0)}{c_3}^{(1)}{c_4}^{(0)} - jc_1{c_3}^{(-1)}{c_3}^{(0)}{c_4}^{(1)}$ $-c_1X_0{c_3}^{(0)}{c_4}^{(-1)} - c_1X_0{c_3}^{(-1)}{c_4}^{(0)} - c_1X_0{c_3}^{(1)}{c_4}^{(-1)}$ $-c_1X_0{c_3}^{(-1)}{c_4}^{(1)}{c_4}^{(1)} - c_1X_0{c_3}^{(1)}{c_4}^{(0)} - c_1X_0{c_3}^{(0)}$ $+\left(jc_1X_0^2 - jc_2\right){c_4}^{(-1)} + \left(jc_1X_0^2 - jc_2\right){c_4}^{(1)} + jc_1X_0^2{c_4}^{(0)}$

2.2.5 Synthesis Procedure

This section summarizes the steps of the synthesis process leading to the definition of the desired MTS. The magnitude and phase of the objective field are provided as inputs, along with the operating frequency f, the relative permittivity ϵ_r and thickness h of the dielectric slab, the length L of the MTS, the required radiation efficiency e_r and the SW wavenumber β_{SW}. Concerning this latter, the actual choice will depend on the specific application. In

general, large values of β_{SW} imply narrower bandwidth, higher losses and larger sensitivity to tolerances. On the other hand, there are limitations on the maximum achievable values of the LW attenuation constant for very low opaque impedance values [41]. In most of the cases, the choice $\beta_{SW} \simeq 1.3 - 1.4k_0$ represents a good trade-off among these contrasting requirements, which ensures an easy implementation through printed patches. However, for applications requiring rapid frequency scanning, β_{SW} will be chosen significantly larger than k_0. Conversely, when low dispersion is needed, β_{SW} will be set as close as possible to k_0. Regarding the radiation efficiency, it is worth noting that, while it can be theoretically set close to 100%, this choice may result in excessively high values of α_x, possibly leading to fabrication challenges. For this reason, an efficiency value around 94-97% is recommended to strike a practical balance.

Starting from these initial data, the value of X_0 and the profiles $\alpha_x(x)$, and $\beta_x^{(-1)}$ are calculated using equations (2.2), (2.23) and (2.24), respectively. Then, the length of the MTS is discretized with a small step size $dx \approx \lambda/25$ and at each step the modulation index and local period are calculated using (2.28) and (2.33). Notice that eq. (2.28) requires an estimate of $\Delta\beta$ for an accurate evaluation of the Green's function. At the first point ($x = 0$) this estimate is obtained by assuming $\Delta\beta = 0$. This choice is justified by the fact that the modulation is always started gradually, so that the modulation index is close to zero at the beginning of the structure. At the other points, the estimate is obtained using the solution at the previous step. Using (2.28) and (2.33) significantly reduces execution time. Once the local modulation parameters are found, the reactance profile is reconstructed through equation (2.34). The steps of the continuous impedance synthesis procedure are outlined in Table 4.1.

Finally, this profile is implemented though patches by using the procedure illustrated in [39]. This latter is based on the creation of impedance maps from simulation of the individual unit cells, assuming periodic boundary conditions as approximate boundaries for smoothly varying modulations.

2.3 Design Examples

This section illustrates the effectiveness of the proposed impedance synthesis process by showcasing different MTS configurations enabling efficient coupling between SPWs and SWs in various scenarios. To fully demonstrate the practical feasibility of the approach, the impedance profiles obtained through the procedure outlined in Section 2.2.5 are also implemented in a physical structure, that is analyzed through full wave simulations. In particular, we have considered H-shaped patches, whose dimensions are determined using the mapping procedure described in [39]. An operating frequency of 28 GHz and a dielectric slab characterized by $\epsilon_r = 6$ and $h = 0.508$ mm are chosen for all the examples.

Full wave simulations are performed using the commercial solver HFSS, employing the simulation setup depicted in Fig. 2.4. In accordance with the geometry introduced in Sections 2.1 and 2.2, the MTS sits in the $xy-$plane, and SW propagation is along x. Taking advantage of the 2D nature of the problem and the TM polarization of the field, only one unit cell enclosed among two perfect magnetic conductor (PMC) boundaries has been considered along y. A planar radiation boundary is set on the top wall. Excitation of the structure is achieved through two distinct sources: a waveport on the bare dielectric slab for the transmitting mode

Table 2.2: Synthesis process

Inputs: f_0, ϵ_r, h, L, e_r, β_{SW}, $\phi(x)$, $A(x)$				
#	***Inputs***	***StepDescription***	***Output***	***Eq.***
1	ϵ_r, h, β_{SW}	Get X_0	X_0	(2.2)
2	$A(x)$, e_r, L	Get the $\alpha_x(x)$ profile.	$\alpha_x(x)$	(2.23)
3	$\phi'(x)$, k_0	Get the $\beta_x^{(-1)}$ profile.	$\beta_x^{(-1)}(x)$	(2.24)
4	$\beta_x^{(-1)}(0)$, β_{SW}, $\alpha_x(0)$, ϵ_r, h	Get an estimate of the Green's function at the FW spectral points $\tilde{X}_{GF}^{(n)}(0)$, assuming $\Delta\beta(0) = 0$	$\tilde{X}_{GF}^{(n)}(0)$	(2.13)
5	$\tilde{X}_{GF}^{(n)}(0)$, X_0	Get the modulation index m at $x = 0$	$m(0)$	(2.28)
6	β_{SW}, $\alpha_x(0)$, $\theta(x)$, $m(0)$	Get the modulation period d at $x = 0$	$\Delta\beta(0)$, $d(0)$	(2.33)
Steps 7-10 will be performed for x_i varying between dx and L in steps of length dx				
7	$\Delta\beta(x_i - dx)$, β_{SW},$\beta_x^{(-1)}(x_i)$, $\alpha_x(x_i)$, ϵ_r, h	Get an estimate of the spectral Green's function evaluated at FW wavenumbers $\tilde{X}_{GF}^{(n)}(x_i)$	$\tilde{X}_{GF}^{(n)}(x_i)$	(2.13)
8	$\tilde{X}_{GF}^{(n)}(x_i)$, X_0	Get the modulation index	$m(x_i)$	(2.28)
9	β_{SW}, $\alpha_x(x_i)$, $\theta(x_i)$, $m(x_i)$	Get the modulation period	$\Delta\beta(x_i)$, $d(x_i)$	(2.33)
10	X_0, $m(x)$, $d(x)$	Get the impedance profile	$X(x)$	(2.34)

and an incident gaussian beam in the receiving mode. Waveports are positioned at both the input and output planes, parallel to the yz plane, in contact with PMCs on both sides to allow for the propagation of a TM-polarized SW.

In all the examples we have assumed that the desired aperture field distribution was known explicitly. When this is not the case, but only some constraints on the radiated/received field are provided, it could be applied in combination with some optimization technique able to provide the aperture field distribution (e.g. based on alternate projections), as an alternative to other synthesis approaches directly based on numerical optimization [65, 68].

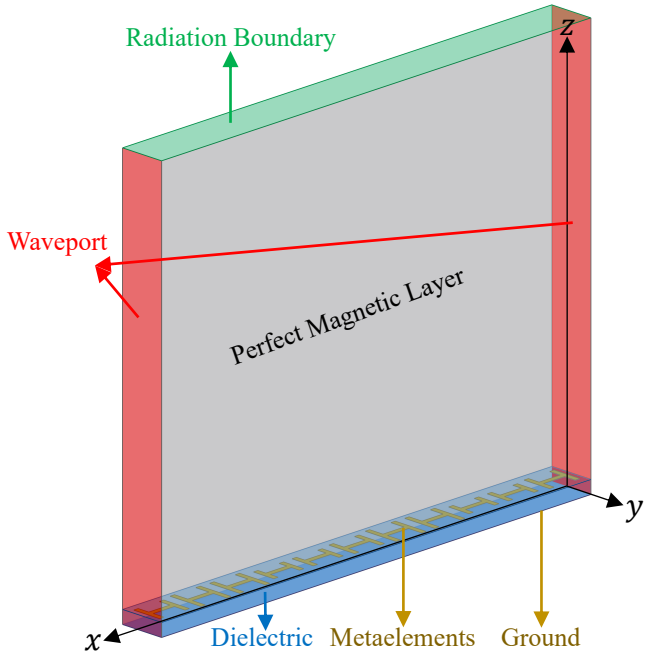

Figure 2.4: HFSS simulation setup.

2.3.1 Leaky-wave Antenna with Sector Beam

In this example, we design a MTS-based SW-to-SPW converter with a sector beam radiation pattern characterized by a beamwidth of 15°, extending from $\theta_0 = -10°$ to $\theta_1 = -25°$. The MTS length is chosen to be $L = 32\lambda$ mm, and the required radiation efficiency is $e_r = 97\%$.

The structure is tested in transmission, by exciting it with a TM SW. As a first design step, the SW propagation constant is chosen to be $\beta_{SW} = 1.3k_0$, corresponding to an average penetrable reactance of -130Ω. The procedure presented in [91] is applied to determine the objective radiating aperture field. Such procedure, given a certain aperture distribution, provides the phase distribution required to obtain the desired radiation pattern. It is noted here that several different techniques can be used to determine the aperture field distribution able to provide a given radiation pattern. The choice of such a technique is transparent to the proposed procedure, which only needs as input the desired aperture field distribution. As a general rule, among different aperture field distributions with the same radiation pattern, it is reasonable to choose the one with the slowest spatial variation. A Gaussian distribution with $\sigma = \frac{16}{3}\lambda$ is selected for the magnitude of the objective field

$$A(x) = Ae^{-(x-L/2)^2/2\sigma^2} \tag{2.35}$$

from which the attenuation constant profile is directly obtained using (2.23) (orange line in Fig. 2.5).

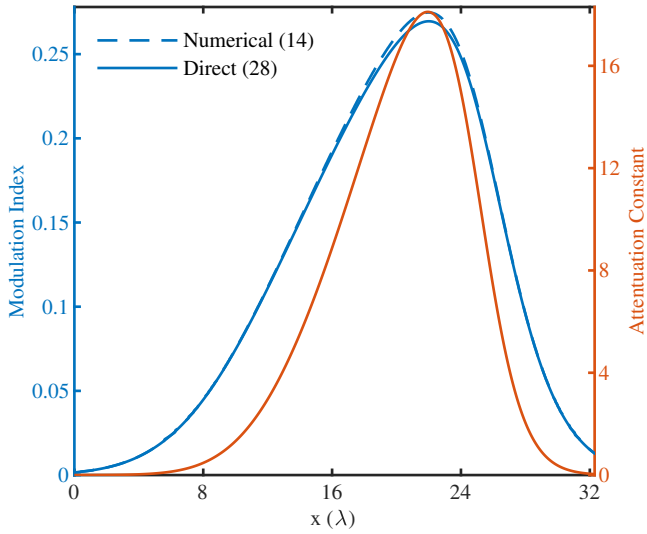

Figure 2.5: Attenuation constant and modulation index profiles for the MTS-LWA.

Then, following [91], the phase distribution is found as

$$\phi'(x) = \pi \frac{L}{\lambda} \left[-\sin\theta_0 - (\sin\theta_1 - \sin\theta_0) \frac{\int_{-1}^{x} |A(x')|^2 dx'}{\int_{-1}^{1} |A(x')|^2 dx'} \right] \tag{2.36}$$

Starting from the profiles in eqs. (4.4) and (2.36), the procedure illustrated in section 2.2 is applied to determine local modulation indexes and periods. Fig. 2.5 depicts the distribution of $m(x)$ obtained from the synthesis process and illustrates its relationship with the corresponding α profile. Importantly, Fig. 2.5 shows that $m(x)$ calculated directly from (2.28) and numerically from (2.14) are almost identical. The synthesized modulated reactance profile, $X(x)$, is shown in Fig. 2.6. It is evident that the envelope of $X(x)$ resembles the profile of $\alpha_x(x)$, and the modulation period decreases with higher values of $m(x)$. Here again, Fig. 2.6 shows that the reactance profiles from our proposed direct synthesis procedure and the numerical-based procedure are nearly identical.

As a preliminary verification step, the obtained profile was simulated in HFSS using piecewise ideal impedance BCs. Fig. 2.7 shows a comparison between the surface current provided by eq. (2.18) and the one obtained from HFSS simulation. The excellent agreement between the two results validates the accuracy of (2.18), which is based on the local use of (2.14).

Finally, the obtained $X(x)$ profile is implemented in a practical patch-type MTS. The reactance curve detailing the relationship between the patch dimensions and the corresponding equivalent reactance value, used for constructing the MTS, is illustrated in Fig. 2.8. The obtained MTS was simulated in HFSS with the setup depicted in Fig. 2.4. Fig. 2.9 showcases the simulated radiation pattern in the xz plane. The close agreement with the desired sector beam pattern and the good control of side lobes (at least 30dB below the peak) confirm the effectiveness of the proposed MTS design.

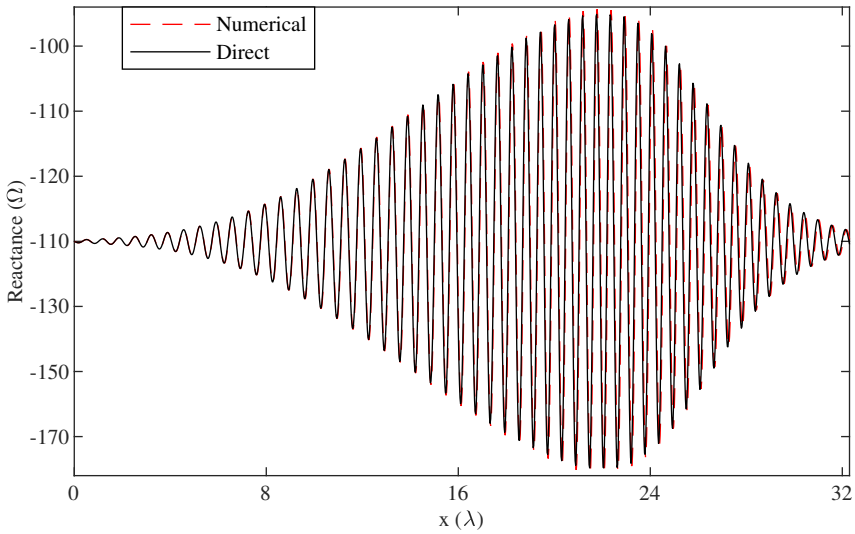

Figure 2.6: Synthesized reactance profile for the MTS-LWA.

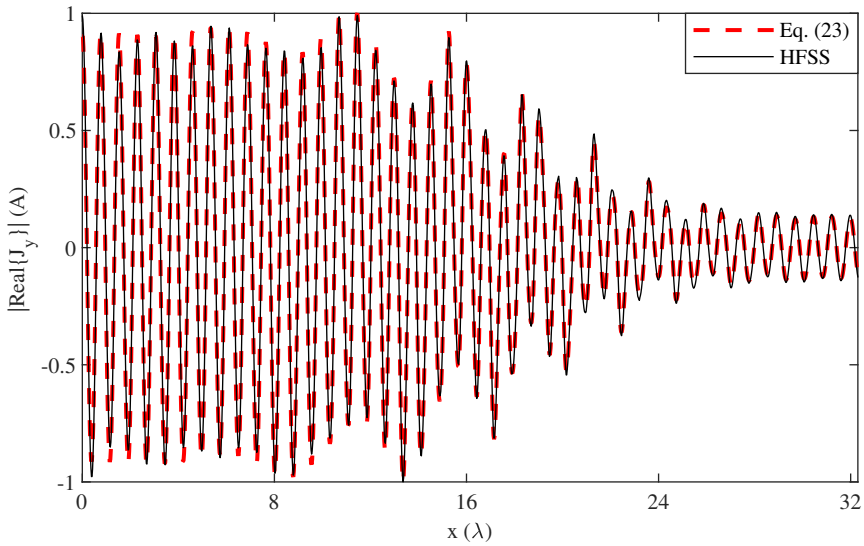

Figure 2.7: Surface current distribution along the MTS-LWA: comparison between the proposed pseudo-analytical approach (eq. (2.18)) and full wave simulations.

2.3.2 Space-wave to Surface-wave converter

In this example, we demonstrate the design of an MTS that achieves highly efficient conversion of an incident SPW into a SW. The incoming wave is modeled using a Gaussian beam (GB) with

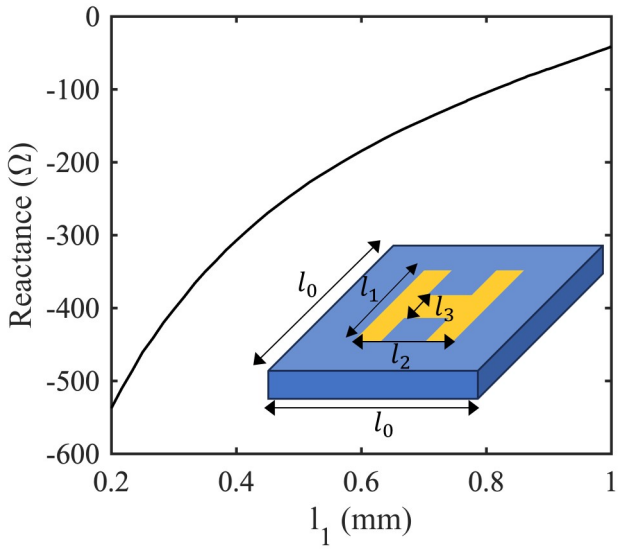

Figure 2.8: Variation of the reactance values with the parameter l_1 in the printed H-shaped patch, alongside the unit cell's geometry. The fixed dimensions of the unit cell are $l_0 = 1.2$ mm, $l_2 = 1$ mm, and $l_3 = 0.2$ mm.

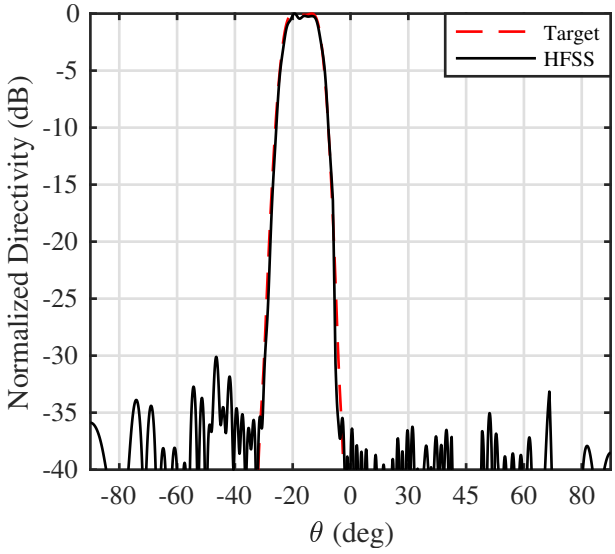

Figure 2.9: Normalized directivity pattern for the MTS-LWA: comparison between the target pattern and the results obtained through full-wave simulations of the MTS implementation.

its minimum waist centered at the point $x = L/2, z = 0$. The incident angle of the Gaussian beam is arbitrarily set at $\theta^i = -15°$, corresponding to a linear phase profile across the aperture. The magnitude of the objective tangential electrical field is still approximately given by Eq. (4.4), where σ is related to GB's minimum waist w_0 as $w_0 = \sqrt{2}\sigma$. Also in this case we choose $\sigma = \frac{16}{3}\lambda$, ensuring a reduction in field amplitude to 1.1% of the peak value at a distance of 16λ from the beam axis. The overall length of the MTS is chosen to be $L = 32\lambda$ mm and the required efficiency is $e_r = 98\%$. The SW propagation constant is $\beta_{SW} = 1.3k_0$.

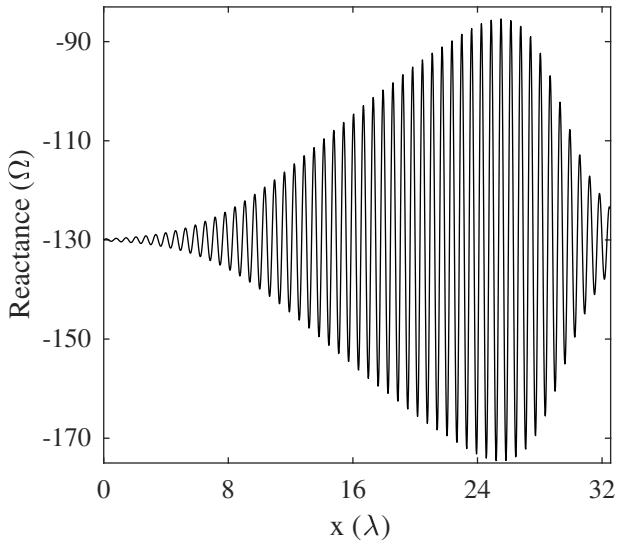

Figure 2.10: Synthesized reactance profile for the GB to SW converter.

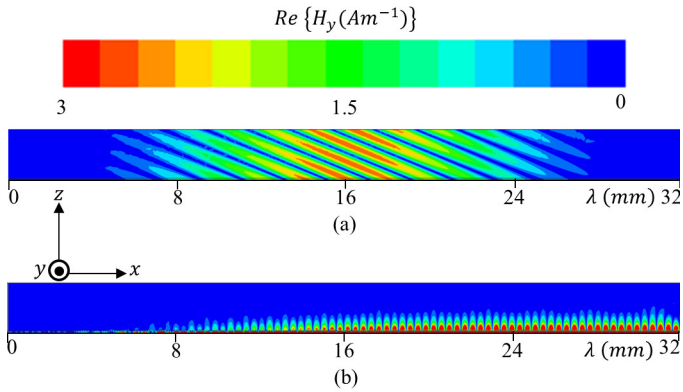

Figure 2.11: Simulated H-Field for SPW to SW converter. (a) Incident field. (b) Scattered field.

Fig. 2.10 illustrates the synthesized $X(x)$ profile for this specific case, which was subsequently implemented using metallic patches. Snapshots of the simulated incident and scattered H_y

fields are shown in Fig. 2.11. The incident power impinging on the MTS area is set as $P_i = 1$ W. Analysis of the scattered field reveals the generation of a SW with increasing magnitude propagating towards the positive x-axis. The total SW power accepted at the terminal port is numerically determined to be $P_{SW} = 0.98$ W, resulting in an excellent conversion efficiency of 98%.

2.3.3 Receiving and Transmitting EM waves using MTS Systems

In this example, we design an MTS that can convert an impinging SPW into a SW and then re-convert the SW into a SPW with a different launch angle and prescribed beamwidth. This structure offers an alternative solution to realize MTS-based anomalous reflectors, as the ones required in SRE to re-direct signal waves. With respect to conventional reflectarray solutions, based on the generalized Snell's law [16], the approach proposed here offers increased flexibility in field manipulation, thanks to the possibility to control also the amplitude distribution of the radiating aperture field. In fact, one advantage of the proposed design is that the power collected from the incident wave can be used to excite radiation with any desired beamform. For instance, the transmitter section of the MTS can be designed as a LWA with either a single or multiple pencil-beams, or with a sector-beam, making it suitable for serving single or multiple end-users in SRE applications.

In this section, we envision two primary usage scenarios for this MTS system. In the first scenario, only a portion of the MTS is exposed to the incident EM waves, which might happen in practice due to the presence of obstacles in the communication environment. In this case, a first portion of the MTS efficiently converts the incoming SPW into a SW, while a second part re-radiates the received power in a desired direction, covering radio blindspots of the primary source. In the second scenario, the entire MTS is exposed to the incoming EM wave. In this configuration, one half of the MTS functions as an SPW-SW converter, while the other half has a twofold function: on one hand it serves as a LW radiator for the SW collected by the first part, and on the other hand it provides a specular reflection for a portion of the impinging wave. This effectively results in the generation of two beams: one in the specular direction and the other one from LW radiation at a prescribed angle. This dual-beam functionality makes it particularly suitable for MIMO applications, as it creates an additional propagation path. For both the systems, the MTS is divided into three sections: a receiving section, a transition part and a transmitting section.

For the first example (System I), the receiving section is designed to convert an impinging Gaussian-beam into a SW. The input parameters for this section are: $\theta^i = -10°$, $L = 22\lambda$ mm, $e_r = 97\%$, and $\beta_{SW} = 1.55k_0$. The transition section has the function to support reflectionless propagation of the SW generated in the receiving section towards the transmitting section. For this reason, it is characterized by an unmodulated reactance, whose value is set equal to the average impedance of both the receiving and the transmitting sections. Finally, the transmitting section is designed to produce a pencil beam radiation pattern with high tapering efficiency. To this end, the magnitude of the tangential radiating field is to be maintained constant over the length of this section. In addition, the launch angle is set to 20°. The length of the transmitter is set to 32λ, longer than the one of the receiver section to provide a narrower beam. This is an example of the increased flexibility offered by this configuration with respect to a phase gradient

reflector. The rest of the input parameters are the same as the receiver part.

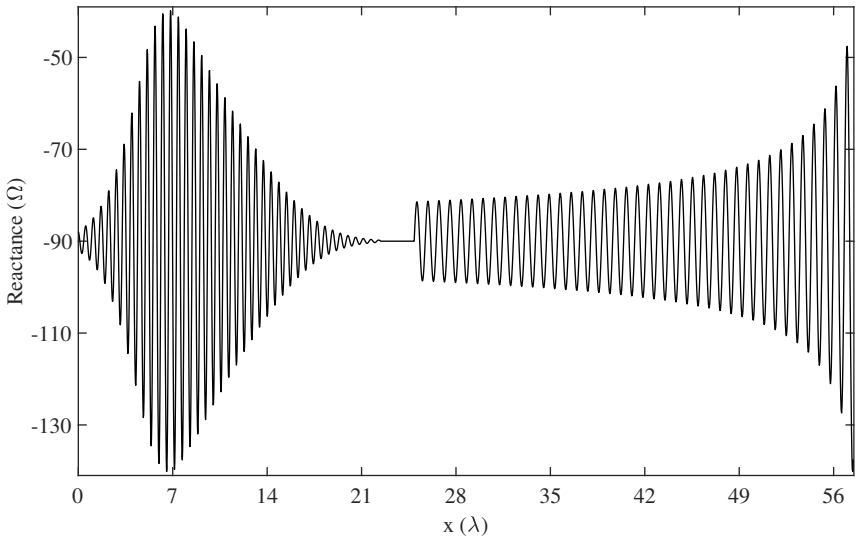

Figure 2.12: Synthesized reactance profile for the MTS system I.

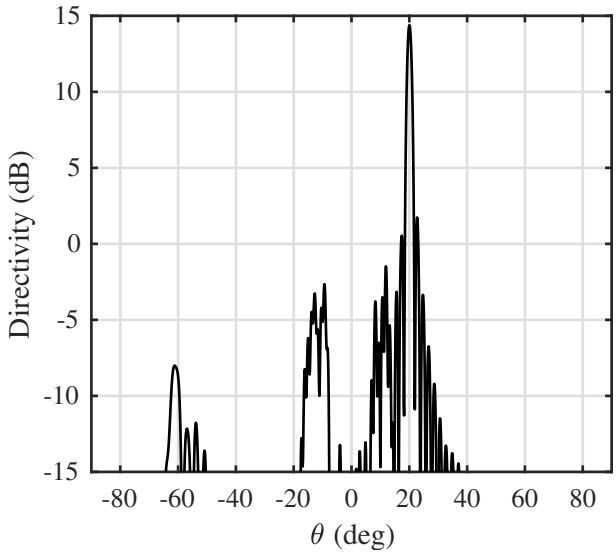

Figure 2.13: Directivity pattern for the MTS system I.

The synthesized profile of $X(x)$ based on the above requirements is shown in Fig. 2.12. The profile of $X(x)$ for the receiving section is similar to the one discussed for the SPW to SW converter example. On the other hand, in the portion of $X(x)$ corresponding to the transmitting

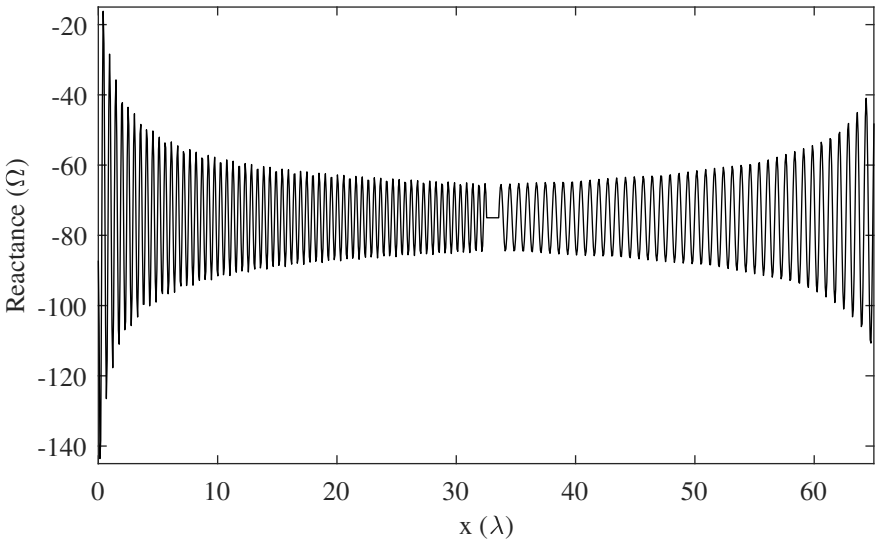

Figure 2.14: Synthesized reactance profile for the MTS system II.

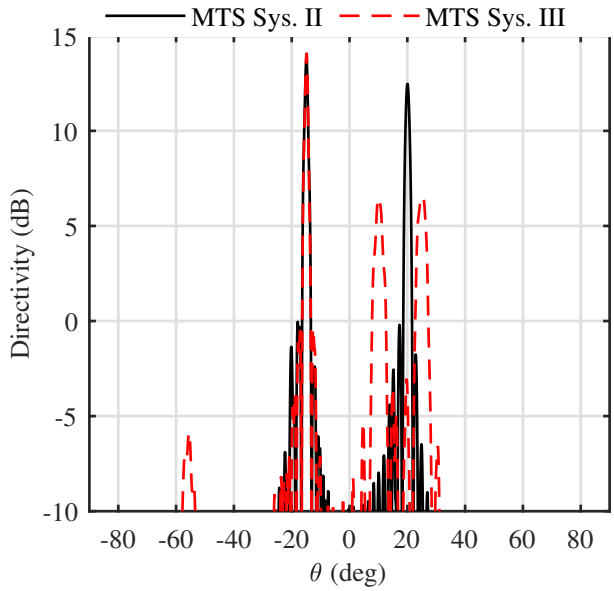

Figure 2.15: Directivity pattern for the MTS systems II & III.

section, the envelope amplitude has an initial gentle rise, followed by an exponential rise at the end. This increasing behaviour of the modulation index is needed to keep approximately constant the amplitude of the radiating aperture field, despite the exponential attenuation of the feeding SW due to radiation power loss.

The simulated directivity pattern is shown in Fig. 2.13. Notably, the main lobe, contributed by the transmitter section, is approximately 18 dB higher than the lobe located at $-10°$, representing the unwanted specular reflection of the wave impinging onto the receiver section. Achieving a maximum directivity of 14.4 dB, this main lobe corresponds to an aperture efficiency of 91% for the length of the transmitter section.

Next, we design the MTS system for the multibeam case. In this configuration, the receiving section is designed for a plane wave excitation, with impinging angle of $-15°$, while the transmitting section is optimized for pencil beam radiation at $20°$. The required reactance profile is shown in Fig. 2.14. The radiation pattern, shown in Fig. 2.15, clearly illustrates the creation of two distinct beams. Notably, the beam associated with specular reflection exhibits a higher directivity, being 1.2 dB more directive than the beam resulting from LW radiation, as it receives contributions from the entire structure. To showcase the versatility of our design in creating additional propagation paths, we also designed and simulated a third system (MTS system III) in which the transmitting section is optimized to generate two beams at $10°$ and $25°$ respectively. The relevant radiation pattern is also shown in Fig. 2.15.

2.4 Conclusion

We presented a systematic approach for designing MTS that efficiently convert SPW to SW and enable SW-based beamforming. First, we developed an analytical framework to model SPW-SW coupling on MTS, based on non-uniformly modulated impedance surfaces. This model established a direct mapping between arbitrary fields—quantified by the distribution of magnitude and phase across the aperture—and the local impedance boundary values. Notably, we derived a novel designer's equation that links the impedance modulation index and period to the field's attenuation and phase constants. Furthermore, the final impedance profile was synthesized using a closed-form expression, resulting in a direct synthesis procedure that is both computationally efficient and fast.

The effectiveness and flexibility of our synthesis procedure were demonstrated through the design of MTS for various applications. These MTS designs, realized with metallic patches on a dielectric substrate, were validated using full-wave simulations. The results revealed a high conversion efficiency, with a remarkable 98% of the incoming waves successfully converted into SW. Additionally, when used as leaky-wave antennas, the MTS designs produced both highly efficient pencil beam and sector beam radiation patterns. The close matched between the target and simulated radiation patterns confirmed the accuracy of our model in predicting α and β across the aperture. Furthermore, the simulated surface currents on the MTS closely matched those predicted by our model.

Significantly, we used our method to design SW based MTS-RIS for SRE applications. In this design, the first section of the MTS efficiently converts an incoming wireless EM signals into a SW, while a different section radiates a beam towards the intended user. We designed the proposed MTS for various piratical scenarios, including different incoming signal waveforms such as Gaussian beams and plane waves. Additionally, we designed the MTS to support different radiation patterns: a pencil beam for single end-user scenarios and dual beams for MIMO applications.

It is important to emphasize that we did not make any a priori assumptions about the frequency behavior of the metasurface. Instead, we implemented the metasurface using printed microstrip technology and employed state-of-the-art full-wave simulations to validate its performance. Printed microstrip technology is a mature platform for metasurface synthesis, whose performance has been well-validated in literature. Moreover, the dimension selected for printed unit-cells in our design followed the minimum achievable line width and spacing available commercially. For future work, the presented design will be used to create fabricated metasurface by microstrip technology and deployed in smart radio environment application.

Chapter 3

Using Generalized Impedance Modulation for Enhanced Control in Metasurface Design

In this chapter, we present a novel synthesis procedure for designing isotropic impedance modulation for high efficiency MTS wave-converters, with a primary focus on suppressing unwanted higher-order modes. To achieve this, we work with the Fourier series formulation of the impedance modulation function and derive a generalization of the Oliner's method for the analysis. This method, based on the Floquet-wave expansion of the fields over the homogenized impedance surface, allows one to calculate the complex amplitude of all the FW modes for any periodically modulated impedance profile, from which the performance of SW to SPW conversion can be fully characterized.

To synthesize smooth impedance profiles, we proceed by progressively adding terms in the Fourier transform of the MTS's impedance profile and optimizing their coefficients to obtain a desired behaviour. We begin by analyzing the performance of modulated MTSs with only three non vanishing Fourier coefficients (FCs) (sinusoidal modulation), highlighting their limitations at broadside and forward angles. Subsequently, we investigate potential solutions involving modulation functions with five FCs. We demonstrate that, with a systematic design, this modulation can effectively suppress unwanted modes at broadside and certain forward angles. Advantageously, this modulation also allows control over the dispersion behavior of the designed MTS. Following this, we synthesize a new impedance profile with seven FCs and showcase its extended angular range. Importantly, the required FCs are calculated in a systematic process.

To develop efficient finite-length MTS devices, we then generalize the design technique to the case of non-uniform modulation parameters, extending the procedure developed in Chapter 2 to the newly developed modulation schemes. As a result, we get closed-form expressions of the required impedance profile for the desired field configurations. Lastly, based on the synthesized impedance profiles, we design practically realizable patch-type MTS devices. Full-wave simulations of the resulting structure demonstrate high conversion efficiency for challenging broadside and forward angles.

3.1 Generalized Oliner's Method

In this section, we derive the equations describing the propagation and radiation characteristics of waves supported by an isotropic impedance surface with a generic periodic modulation. The proposed approach is a generalization of the procedure presented in [57] for sinusoidally

modulated impenetrable IBC (IIBC) to the case of a penetrable IBC (PIBC) with an arbitrary periodic modulation. As previously noted, the PIBC represents an accurate model for printed metallic layers typically used for MTS implementation in the microwave range [10]. The case of IIBC with generic periodic modulation was studied in [70].

In the following, we will consider a PIBC sitting on a single grounded dielectric slab with dielectric constant ε_r and tickness h, which represents the simplest and most commonly used MTS implementation in the microwave range. For these structures, the dominant mode is transverse magnetic (TM). For this reason, we focus our analysis on the case of TM polarization. The procedure, however, can be straightforwardly extended to the case of TE polarization.

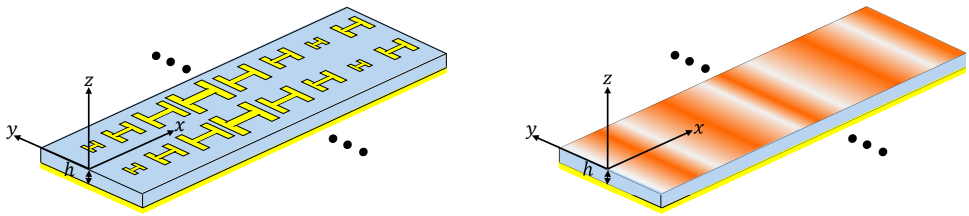

(a) (b)

Figure 3.1: Geometry for the problem of the isotropic 1-D periodically modulated Patch-type MTS (a) and its equivalent 'generalized' impedance modulation model (b).

We introduce a Cartesian reference system with its xy-plane coincident with the PIBC plane (Fig. 3.1). The PIBC reactance, denoted as X, is defined as the imaginary part of the ratio between the average tangential electric field and the average current flowing in the metallic cladding (see Eq. 2.1 in Chapter 2). The penetrable reactance is periodically modulated along x with period d and invariant along y; we consider wave propagation along the x-axis. The periodic function $X(x)$ can be represented through a Fourier series as follows:

$$X(x) = \sum_{q=-\infty}^{\infty} X^{(q)} e^{-j\frac{2\pi q}{d}x} \tag{3.1}$$

Owing to the periodicity, the fields and currents supported by the structure can be expressed as summation of harmonics, or Floquet-wave modes:

$$J(x) = \sum_{n=-\infty}^{\infty} J^{(n)} e^{-jk_x^{(n)}x} \tag{3.2}$$

$$E_x(x) = \sum_{n=-\infty}^{\infty} E_x^{(n)}(x) e^{-jk_x^{(n)}x} \tag{3.3}$$

where

$$E_x^{(n)} = \frac{1}{d}\int_0^d E_x e^{jk_x^{(n)}x} dx \tag{3.4}$$

$$k_x^{(n)} = k_x^{(0)} + \frac{2\pi}{d}n = \beta_x^{(0)} - j\alpha_x + \frac{2\pi}{d}n = \beta_{SW} + \Delta\beta - j\alpha_x + \frac{2\pi}{d}n \tag{3.5}$$

Here, β_{SW} is the transverse propagation constant of the input SW supported by the average impedance $jX^{(0)}$. From Eq. (3.5), it is evident that for appropriate values of d, the -1-indexed FW mode enters the visible region (VR), giving rise to a LW. To maximize conversion efficiency, the power carried by the 0-indexed FW mode, which is slow, must entirely convert into radiative power carried by the -1-FW mode. Critically, if multiple modes coexist within the VR, the power becomes distributed among them, leading to reduced efficiency.

By combining (2.1), (3.1) and (3.2) we get:

$$E_x(x) = j \sum_{q=-\infty}^{\infty} X^{(q)} e^{-j\frac{2\pi q}{d}x} \sum_{n=-\infty}^{\infty} J^{(n)} e^{-jk_x^{(n)}x} \tag{3.6}$$

The Green's function (GF) of the grounded slab, which relates the equivalent current to the tangential electric field, provides additional equations in the mathematical model:

$$E_x^{(n)} = jX_{GF}\left(k_x^{(n)}\right) J^{(n)} \tag{3.7}$$

where,

$$X_{GF}\left(k_x\right) = \frac{\zeta\sqrt{(k_x^2 - k_0^2)(\varepsilon_r k_0^2 - k_x^2)}\tan\left(h\sqrt{\varepsilon_r k_0^2 - k_x^2}\right)/k_0}{-\varepsilon_r\sqrt{k_x^2 - k_0^2} + \sqrt{\varepsilon_r k_0^2 - k_x^2}\tan\left(h\sqrt{\varepsilon_r k_0^2 - k_x^2}\right)} \tag{3.8}$$

ζ and k_0 being the free space impedance and wavenumber, respectively. By combining (3.6) and (3.7), and projecting onto $e^{j\frac{2\pi n}{d}x}$, we get

$$\sum_{q=-\infty}^{\infty} X^{(q)} J^{(n-q)} - X_{GF}\left(k_x^{(n)}\right) J^{(n)} = 0 \quad n = 0, \pm 1, \pm 2, .. \tag{3.9}$$

The set of equations in (3.9) provides a comprehensive description of the MTS operation, establishing the relationship between the impedance Fourier coefficients $X^{(n)}$ and the phase and attenuation constants β_x and α_x that characterize the supported modes. Importantly, the nontrivial solution of (3.9) for $J^{(n)}$, which only exists when the determinant of the linear system vanishes, corresponds to the current modes supported by the structure. For any given reactance profile, these equations can be solved to find the field configuration. Reversely, the synthesis process consists in determining the values of the reactance coefficients providing the desired values of β_x and α_x while eliminating the unwanted modes $J^{(n)}$.

3.2 Sinusoidally Modulated Impedance

For the case of sinusoidal modulation, the reactance of the MTS is given by:

$$X(x) = X^{(0)}\left(1 + \frac{M}{2}e^{j\frac{2\pi}{d}x} + \frac{M}{2}e^{-j\frac{2\pi}{d}x}\right) \tag{3.10}$$

where M is the modulation index. Notably, the Fourier series consists of three coefficients.

3.2.1 Forward Radiation

Consider the case when there are two modes, $n = -1$ and $n = -2$, in the VR, which may happen for forward pointing direction of the -1 FW. Solving eq.(3.9) with $n = -2$ for $J^{(-2)}$ and ignoring the FW terms outside the we get:

$$J^{(-2)} = -\frac{1}{2}\frac{MX^{(0)}J^{(-1)}}{X^{(0)} - X_{GF}\left(k_x^{(-2)}\right)} \tag{3.11}$$

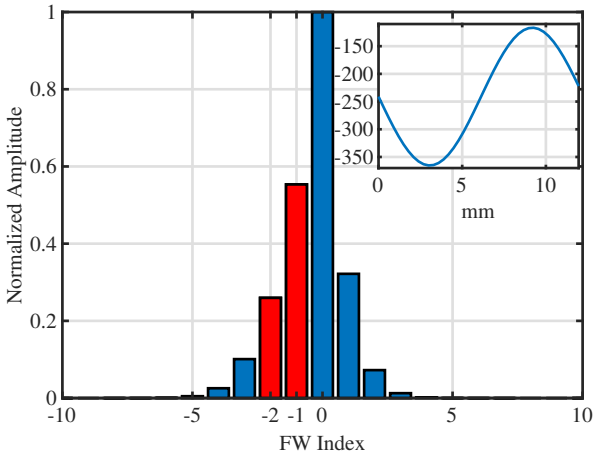

Figure 3.2: Amplitude of the spectral components (FWs) of the current flowing in the sinusoidally modulated MTS designed to radiate at 10°. Inset: Reactance profile.

It is clear from Eq. (3.11) that this coefficient is different from zero for any non vanishing value of the modulation index. Indeed, a limitation of the sinusoidal modulation lies in the fact that there is only one term in the numerator in Eq. (3.11), consequently making it impossible to achieve $J^{(-2)} = 0$. To illustrate this behaviour, consider the following example: we want to design an MTS antenna operating at $f = 26$ GHz, with a slab characterized by $\epsilon_r = 6$, $h = 0.508$ mm, SW propagation constant $\beta_x = 1.11k_0\ m^{-1}$, -1 FW mode pointing angle $\theta^{(-1)} = 10°$ and attenuation constant $\alpha = 7\ m^{-1}$. By solving the equation system (3.9), we obtain the following design values: $M = 0.516$, $d = 12.256$ mm, and $X^{(0)} = -241\ \Omega$. It can be easily verified that with this choice of the period, the -2 FW also falls in the VR, at an angle $\theta^{(-2)} = -50°$. Fig. 3.2 depicts the amplitude of the FW coefficients of the current (the eigen solution of Eq. (3.9)), with the reactance profile shown in the inset. Notably, the amplitude of the unwanted FW mode $J^{(-2)}$ is 47% of the amplitude of the desired FW mode $J^{(-1)}$.

In Eq. (3.11), it is evident that $J^{(-2)}$ exhibits a non-linear dependency on the transverse propagation constants, α_x and β_x. For deeper insights, we conducted an analysis of an MTS antenna with $\theta^{(-1)} = 10°$, varying the values of α_x and β_x as illustrated in Fig. 3.3. Notably, α_x is predominantly influenced by parameter M, while β_x is determined by $X^{(0)}$. As observed in Fig. 3.3, for a fixed α_x, the magnitude of $J^{(-2)}$ diminishes with increasing values of β_x. This

observation implies that achieving forward radiation in sinusoidally modulated MTS antennas demands large SW wavenumbers, typically associated to high dispersion, which may restrict broadband operation. Lastly, for a constant value of β_x, the magnitude of $J^{(-2)}$ increases with higher values of α_x.

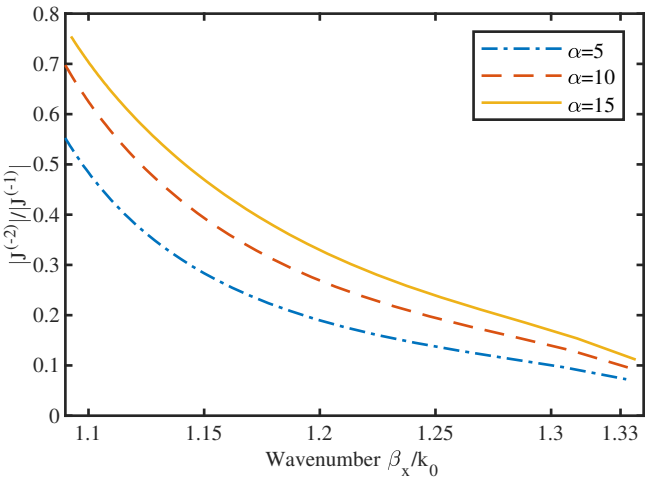

Figure 3.3: Amplitude of the ratio between the FW currents $J^{(-2)}$ and $J^{(-1)}$ against β_x for different values of α_x.

3.2.2 Broadside Radiation

MTS antennas with isotropic sinusoidal modulation exhibit an open stopband (OSB), characterized by a reduction of α to zero at the frequency of broadside radiation. This behavior, which stems from the coupling between the $n = -2$ and $n = 0$ FW modes, has been systematically documented in [69]. Further substantiation of this effect is provided by the FW current distribution of a sinusoisally modulated MTS designed to radiate at broadside, depicted in Fig. 3.4, which clearly demonstrates that $\left|J^{(-2)}\right|$ equals $\left|J^{(0)}\right|$, while $\left|J^{(-1)}\right|$ is close to zero.

3.3 Five Fourier Coefficients Modulated Impedance

In the next phase of this study, we evaluate the performance of a modulation described by five Fourier coefficients, expressed in the general form as shown in Eq. (3.12):

$$X(x) = X^{(0)} + \frac{X^{(0)}M_1}{2}(e^{j\frac{2\pi}{d}x} + e^{-j\frac{2\pi}{d}x}) + \frac{X^{(0)}M_2}{2}(e^{j\frac{4\pi}{d}x+j\phi} + e^{-j\frac{4\pi}{d}x-j\phi}) \tag{3.12}$$

The equation for $J^{(-2)}$ for this modulation is derived and presented in Eq. (3.13):

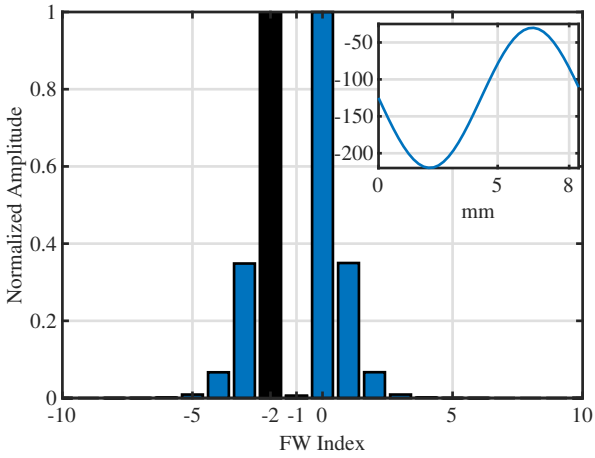

Figure 3.4: Amplitude of the spectral components (FWs) of the current flowing in the sinusoidally modulated MTS designed to radiate at broadside.

$$J^{(-2)} = -\frac{1}{2}\frac{M_1 X^{(0)} J^{(-1)} + M_2 e^{j\phi} X^{(0)} J^{(0)}}{X^{(0)} - X_{GF}^{(-2)}} \tag{3.13}$$

Advantageously, this expression contains two terms in the numerator, offering the possibility to choose the modulation parameters such that the two terms cancel each other, thus, significantly reducing the magnitude of $J^{(-2)}$. Furthermore, Eq. (3.13) imposes no limitations on the range of achievable α and β.

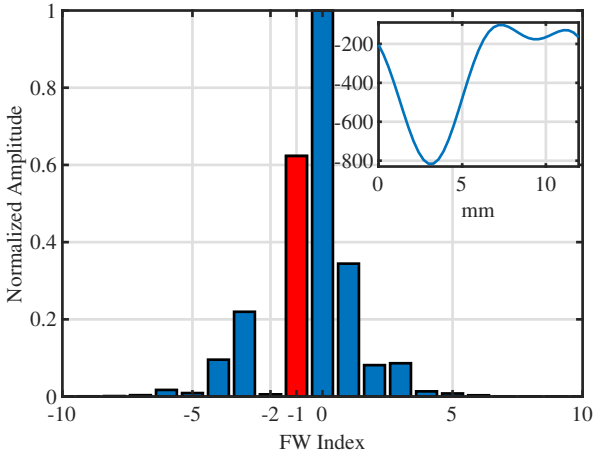

Figure 3.5: Amplitude of the FWs of the current flowing in the MTS with a modulation described by five FCs radiating at 10°. Inset: Reactance profile.

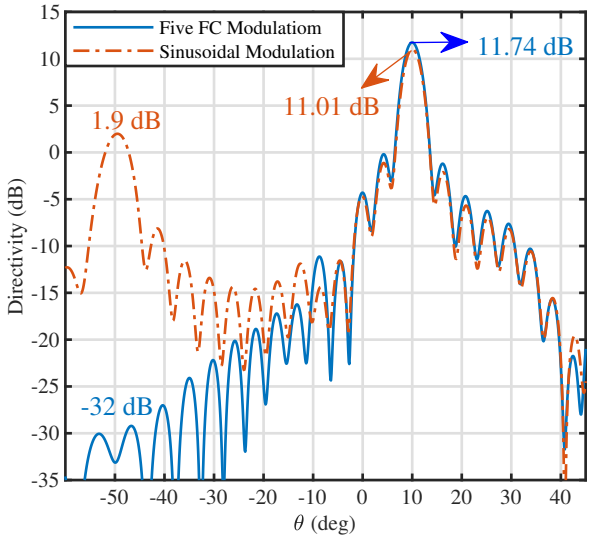

Figure 3.6: Simulated radiation pattern for uniformly modulated MTS antennas. Comparison between different modulation schemes.

3.3.1 Forward Radiation

To assess the performance of this modulation, we design an MTS antenna using the same input parameters as for the sinusoidal case. Also in this case we solve Eq. (3.9), with an additional condition to minimize Eq. (3.13). The resulting design values are $M_1 = 0.918$, $M_2 = 0.42$, $\phi_2 = 264°$, $d = 12.257$ mm, and $X^{(0)} = -400\ \Omega$. The amplitude values of the FW current are depicted in Fig. 3.5. Notably, the magnitude of the unwanted term $J^{(-2)}$ is reduced by a factor 46 compared to the sinusoidal case. Moreover, the functional form of this modulation is shown in the inset of Fig. 3.5, with the reactance profile displaying a reasonably smooth spatial variation within its period.

For a more comprehensive assessment, we conducted a full-wave analysis of these two cases. We realized two uniformly modulated MTS antennas spanning 15λ using the design values calculated above and simulated them in the HFSS software. The simulated radiation patterns are presented in Fig. 3.6. Notably, the radiation lobe corresponding to the $n = -2$ mode exhibits a 34 dB reduction for the five Fourier coefficient modulation compared to the sinusoidal modulation. As a consequence, the directivity of the main lobe surpasses that of the sinusoidal case.

3.3.2 Broadside Radiation

As discussed in Section 3.2.2, the occurrence of an open stopband during broadside radiation is primarily attributed to the excitation of the $n = -2$ FW mode. Our approach efficiently

suppresses $\left|J^{(-2)}\right|$, thus, providing an effective solution to the OSB issue. As a demonstration, let us consider a broadside radiating antenna characterized by a propagation constant $\beta_x = 1.33k_0$ and an attenuation constant $\alpha_x = 7$. The modulation parameters synthesized for this scenario are as follows: $M_1 = 0.162$, $M_2 = 0.04$, $\phi = 179°$, $d = 8.65$ mm, and $X^{(0)} = -110\ \Omega$. The resulting FW currents, illustrated in Fig. 3.7, confirm the successful suppression of undesired FW mode.

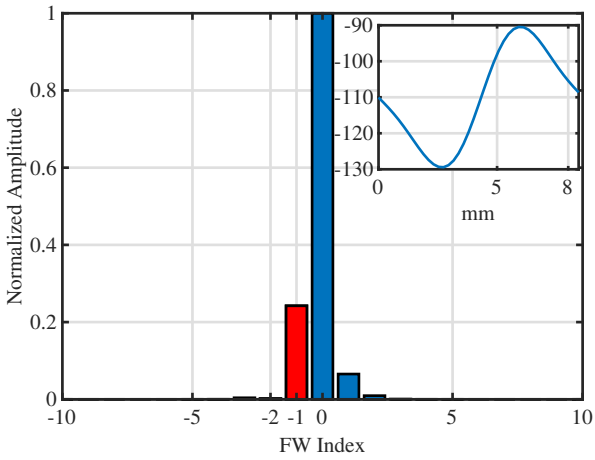

Figure 3.7: Amplitude of the FWs of the current flowing in the five FCs modulated MTS radiating at broadside. Inset: Reactance profile.

Additionally, we conduct a numerical analysis on the dispersion behavior of the modulated impedance surfaces introduced above within a frequency range around the broadside frequency. The design parameters for the two modulations are the same used for generating Fig. 3.4 and Fig. 3.7. The propagation constant and current values plotted in Fig. 3.8 are obtained by solving 3.9. As expected, for the sinusoidal case (orange curve), α approaches zero at the broadside frequency, while its β_x curve exhibits discontinuity around this frequency. In contrast, for the five FC modulation, reasonably well-behaved α_x and β_x curves are observed. These results align with the significant suppression of the -2-FW mode in the five FC modulation case, as illustrated in Fig. 3.8 (c).

3.4 Seven Fourier Coefficients Modulated Impedance

The preceding analysis of two modulation methods suggests that increasing the number of Fourier coefficients can enhance control over radiating FW modes. This augmentation proves especially advantageous in the design of MTS antennas with large forward radiation angles, where also ne $n = -3$ FW mode can enter the visible region, leading to additional undesired radiation. In this context, we investigate modulation employing seven FC, as defined in (3.14).

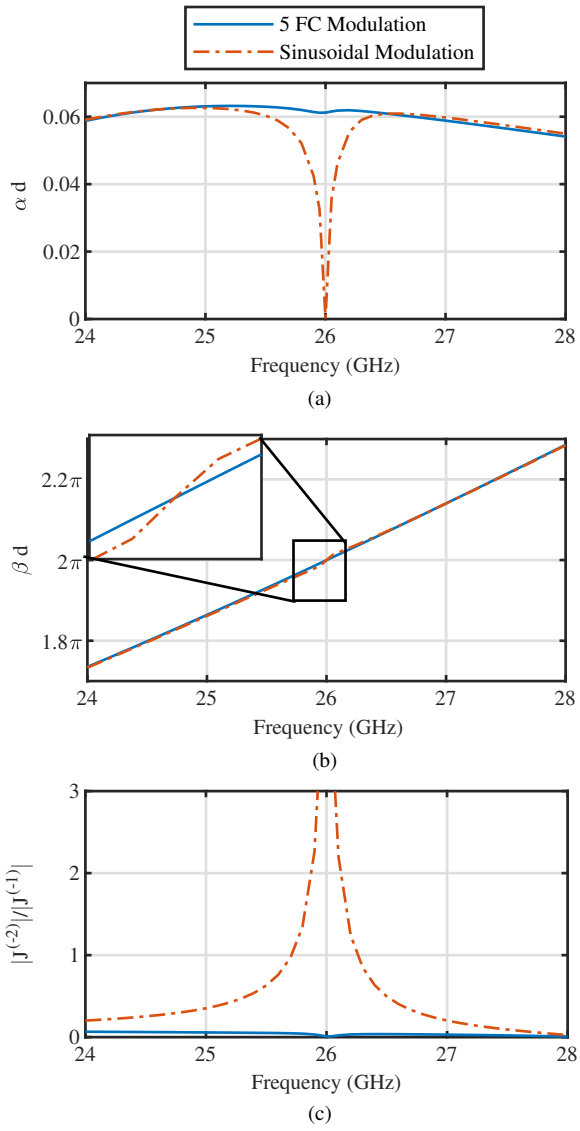

Figure 3.8: Dispersion analysis of the five FCs modulated (blue curve) MTS and sinusoidally modulated (orange curve) MTS radiating at broadside. (a) Normalized attenuation constant (αd). (b) Normalized propagation constant (βd) of the 0-FW mode. (c) Relative magnitude of the -2-FW mode with respect to -1-FW mode.

$$X(x) = X^{(0)} + X^{(+1)}e^{-j\frac{2\pi}{d}x} + X^{(-1)}e^{j\frac{2\pi}{d}x} + X^{(+2)}e^{-j\frac{4\pi}{d}x} + X^{(-2)}e^{j\frac{4\pi}{d}x} + X^{(+3)}e^{-j\frac{6\pi}{d}x} + X^{(-3)}e^{j\frac{6\pi}{d}x} \tag{3.14}$$

where,

$$X^{(\pm 1)} = \frac{X^{(0)} M_1}{2}, X^{(\pm 2)} = \frac{X^{(0)} M_2 e^{\mp j\phi_1}}{2}, X^{(\pm 3)} = \frac{X^{(0)} M_3 e^{\mp j\phi_2}}{2} \tag{3.15}$$

Our main focus is on the efficient suppression of $J^{(-2)}$ and $J^{(-3)}$ FW modes. To accomplish this, we derive their equations in terms of modulation coefficients, represented by Equations (3.16a) and (3.16b) as follows:

$$J^{(-2)} = \frac{X^{(1)} J^{(-3)} + X^{(-1)} J^{(-1)} + X^{(-2)} J^{(0)} + X^{(-3)} J^{(1)}}{-X^{(0)} + X_{GF}^{(-2)}} \tag{3.16a}$$

$$J^{(-3)} = -\frac{X^{(-1)} J^{(-2)} + X^{(-2)} J^{(-1)} + X^{(-3)} J^{(0)}}{X^{(0)} - X_{GF}^{(-3)}} \tag{3.16b}$$

The synthesis process to get the required reactance profile involves solving (3.9) while minimizing the values of (3.16a) and (3.16b). As a validation of this method, we employ the seven FC modulation to design an MTS antenna radiating at a large angle of 60°. The resulting FW modes, depicted in Fig. 3.9, affirm the suppression of undesirable modes.

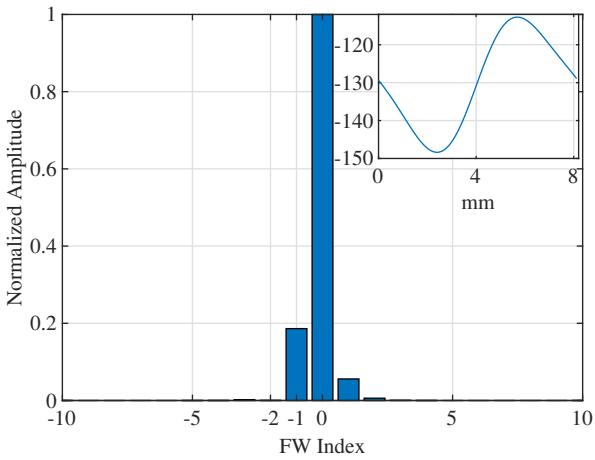

Figure 3.9: Amplitude of the FWs of the current flowing in the seven FC modulated MTS radiating at 60°. Inset: Reactance profile.

3.5 Design of Finite Length MTSs

For finite-length MTS devices, an effective transmission (or reception) of waves necessitates a variable distribution of modulation parameters across the device's aperture, a technique known as constant average non-uniform modulation. This technique was used to design sinusoidally modulated MTSs in our Chapter 2. Here, we apply this technique to our proposed generalized modulation scheme. Fig. 3.10 presents the flowchart outlining the main steps of the design

technique. Although we refer here to the case of a SW-SPW converter, it is understood that the same procedure can be also applied to SPW-SW converter.

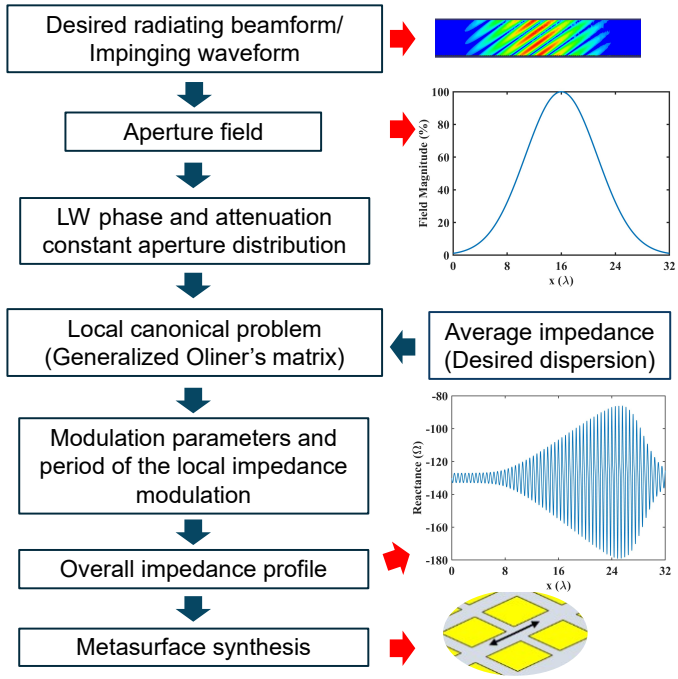

Figure 3.10: Flow chart of non-uniform modulation synthesis procedure for finite-length MTS SW-SPW (or SPW-SW) converter.

Firstly, requirements are specified for the radiation pattern associated with a certain aperture distribution. By identifying the radiating field with the -1 indexed term of the generalized FW expansion, the aperture field distribution is translated into corresponding distributions of the LW constants α_x and β_x. Subsequently, local impedance modulation parameters for a desired dispersion value (determined by average impedance) are calculated using (3.9) to excite the LW with desired characteristics. Once local FC values are known, we obtain the overall reactance profile using the following closed-form expression:

$$X(x) = \sum_{q=-N}^{N} X^{(q)}(x) e^{-jq \int_0^x \frac{2\pi}{d(x')} dx'} \quad n = 1, 2, 3 \tag{3.17}$$

Finally, practical implementation is achieved by printing electrically small patch elements on a grounded dielectric slab. A rigorous analysis of the proposed reactance modulation schemes can then be obtained by performing full-wave simulation on patch-type MTS.

The determination of the dimensions and shapes of the metallic patches providing a given reactance profile follows established procedures documented in the literature [39]. In the design presented here, the patches lie in the xy-plane, with the SW propagation considered along the x-axis. Since the structure is assumed to be invariant along y, only one unit cell with perfect

magnetic boundary conditions is considered in that direction; as a consequence, the width of the simulated MTS structure along y matches the dimensions of one unit cell of the patch element. The dielectric slab used in simulations features a relative permittivity of $er = 6$ and a thickness of $h = 0.508$ mm. The micro-period unit cell is square with a size of 1.2 mm. All analyses are conducted at 26 GHz using the HFSS simulator.

3.5.1 MTS-SPW-to-SW Converter for Broadside Incidence

In the first scenario, we designed a SPW to SW converter to receive a wave incoming from broadside direction. The incoming SPW was modeled as a Gaussian Beam (GB) with a beamwidth of $15\sqrt{2\lambda}$. The length and SW's wavenumber of the MTS are set as 45λ and $1.3k_0$, respectively. For the above design requirements, we employed a five FCs modulation to synthesize the required reactance profile. As described in design flowchart (Fig. 3.10), the $\alpha_x(x)$ distribution is first derived from the desired tangential field (GB distrubtion). Following that, the modulation parameters (M_1, M_2, ϕ_2, d) are obtained. Based on the modulation parameters, the overall reactance profile is synthesized using Eq. 3.17,; the result is shown in Fig. 3.11. The reactance profile exhibits a smooth variation around the average reactance $X^{(0)}$ of -110Ω and was effectively realized using a patch-type MTS. Fig. 3.12 displays the simulated magnetic fields of the SPW to SW conversion performed by the MTS. It is evident that a well-defined SW is generated, propagating along the x-axis. The conversion efficiency was calculated by comparing the power associated with the impinging GB to the power received at port 1 through the SW, resulting in an impressive efficiency of 94%.

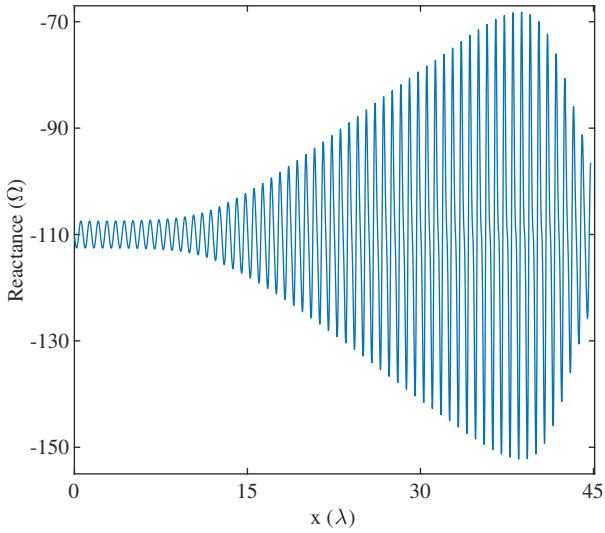

Figure 3.11: Reactance profile for five FC modulated MTS based SPW to SW converter.

Additionally, we introduce a new MTS converter designed with a lower operating wavenumber of $1.1k_0$, corresponding to an average reactance (X^0) of -400Ω. Figure 3.13 presents the

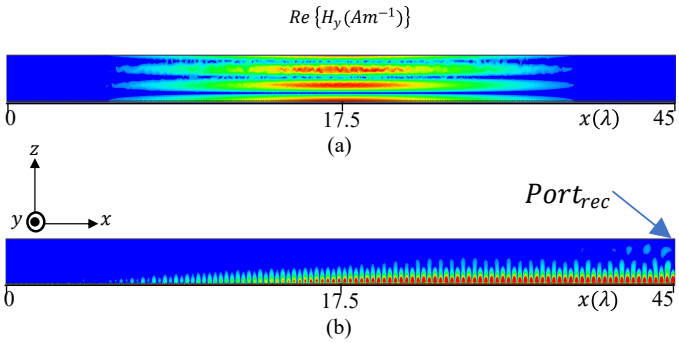

Figure 3.12: Simulated magnetic field for MTS based SPW to SW converter. (a) Incidence field. (b) Scattered field.

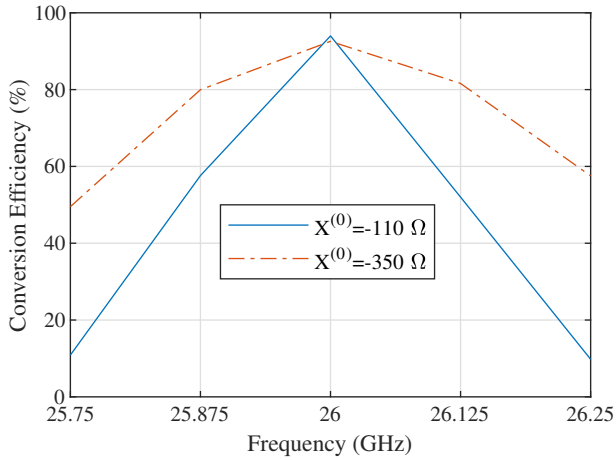

Figure 3.13: Conversion efficiency versus frequency responses for MTS based SPW to SW converters with different average reactance: $X^{(0)} = -400\Omega$ (blue lines) and $X^{(0)} = -130\Omega$ (red lines).

comparison of the frequency behaviour over a 500 MHz band of the conversion efficiency between this new design and the previous one ($X^0 = -400\Omega$). As expected, the MTS converter with the lower wavenumber exhibits reduced dispersion, evidenced by a 31% drop in conversion efficiency at the edge frequency, in contrast to the 81% decrease observed in the other design. This validates our design process's efficacy in significantly controlling the dispersion characteristics of the created MTS devices.

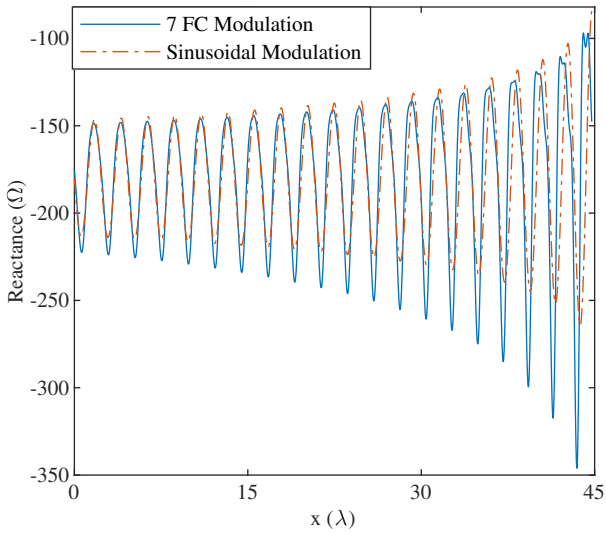

Figure 3.14: Reactance profile for seven FC modulated MTS LWA.

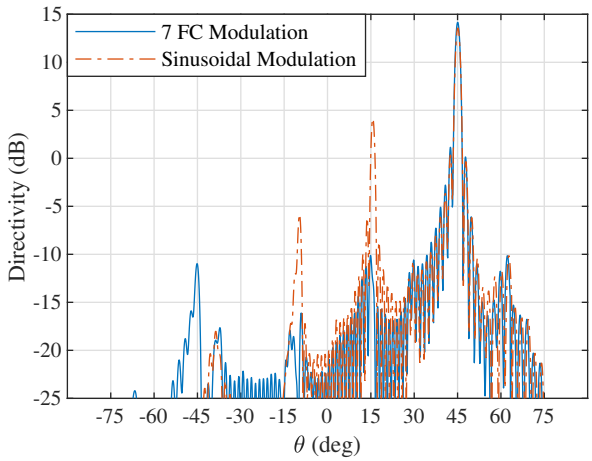

Figure 3.15: Simulatied radiation pattern for MTS LWA.

3.5.2 MTS-LWA in Forward Radiation

In this example, we design an MTS-LWA radiating at 45°. The input SW operates at a wavenumber of $1.3k_0$. Under these parameters, there are three FW modes whose wavenumber falls in the VR: $n = -1$, $n = -2$ and $n = -3$. Among them, only the first one is desired. To suppress the other two modes, we employ a seven FCs modulation to obtain the correct MTS design. A highly efficient pencil-beam is selected as the desired radiation pattern for the MTS, which corresponds to constant magnitude of field across the MTS.

Based on the design requirements, all the modulation parameters, including the modulation indexes $M_1(x)$, $M_2(x)$, and $M_3(x)$, are calculated. Following that, the overall reactance profile $X(x)_{7FC}$ is obtained, as shown in Fig. 3.14. For comparison, the reactance profile $X(x)_{sin}$ based on sinusoidal modulation is generated for the same design requirements. For each local period, the maximum and minimum values of $X(x)_{7FC}$ are consistently higher than those of $X(x)_{sin}$. These differences become more prominent towards the end, where values of α are significantly high. Subsequently, we design a patch-type MTS based on this reactance profile and conduct full-wave simulations. The resulting radiation pattern for 7 FC modulation based MTS, illustrated in Fig. 3.15, demonstrates high directivity, with a calculated radiation efficiency of 97%. For sinusoidally modulated MTS this value drops to 91%. Moreover, it is observed that the seven FC-modulated MTS suppresses the -2-FW mode and -3-FW mode by -15 dB and -17 dB, respectively.

3.6 Conclusion

An analytical impedance synthesis procedure to design an MTS-based SPW-SW coupler, capable of receiving or transmitting signals at virtually any angle, has been presented. The proposed synthesis procedure, along with its inverse analysis procedure, was derived by deriving the expression of the Floquet-wave expansion coefficients of the target fields as a function of the Fourier series coefficients of the modulated reactance. We first established that the conversion inefficiency observed at broadside and forward angles for the basic sinusoidally modulated MTS was primarily attributed to the excitation of specific FW modes. As a solution, we used five FCs modulated impedance for MTS design and showed that its modulation parameters can be chosen to effectively suppress one unwanted FW mode. Importantly, we found the exact modulation parameters using analytical equations. Next, we demonstrated the possibility to further increase the angular range of MTS couplers using seven FC modulation. Furthermore, we applied these proposed modulations to design finite-length MTS structures using non-uniform modulation. Through full-wave analysis of patch-type MTSs implementing the synthesized reactance profiles in two scenarios, we showcased the practical applicability and robustness of this approach.

Chapter 4

Controlling Surface Wave Dispersion in Modulated Metasurfaces for Smart Radio Environments

This chapter introduces a novel passive and static MTS device designed to receive a broadband wireless signal and transmit it towards frequency-dependent angular directions by employing a double conversion to/from SW. The objective is to enable physical layer orthogonal frequency division multiplexing by properly assigning different subcarriers to various users [54]. Our MTS design relies on the design of continuous IBC profiles, that are finally implemented through printed patches on grounded dielectric. The process of attaining efficient SW-SPW conversion via the appropriate impedance profile has been detailed in Chapter 2 and Chapter 3. Here, we expand upon this foundation, focusing on manipulating and controlling the dispersion characteristics of SWs on modulated IBC to create this innovative, simple, and low-cost 'Metaprism' (MTP). As in other studies related to SW-based re-routing, we adopt a three-part configuration comprising a receiver, a transition, and a transmitter sections. To obtain the intended functionality, three distinct dispersion profiles are devised for each section: dispersion is very limited in the first section, to enable the simultaneous reception of multiple frequencies, while it is high in the transmitting section, to enhance frequency scanning. The transition section provides a smooth transition between the two regimes. After a first design was done at homogenized impedance level, a realistic implementation through patches printed on a grounded slab was carried out. An important result of this study is the correlation between SW dispersion and both the homogenized impedance values and the synthesized patch shapes. Comprehensive full-wave simulations were conducted on the final MTS device, confirming its effective performance. Broadband performance are compared with the one of MTS-RIS using direct anomalous reflection.

Additionally, we propose a simple yet effective solution to extend the applicability of the proposed device to a scenario where the impinging SPW power is collected on one side of a building and must be re-routed to another shadowed side, to address radio blind spots. The design of the bent MTS is carried out by propagating the SW along a sharp corner, where power transfer efficiency is maximized by controlling the dispersion of the MTS covering the corner region.

The chapter is organized as follows. Section 4.1 formulates the problem and illustrates the working principle and design procedure for the proposed MTP. Section 4.2 presents numerical results. Next, Section 4.3 details the deesign and analysis of bent-MTS. Finally, Section 4.4

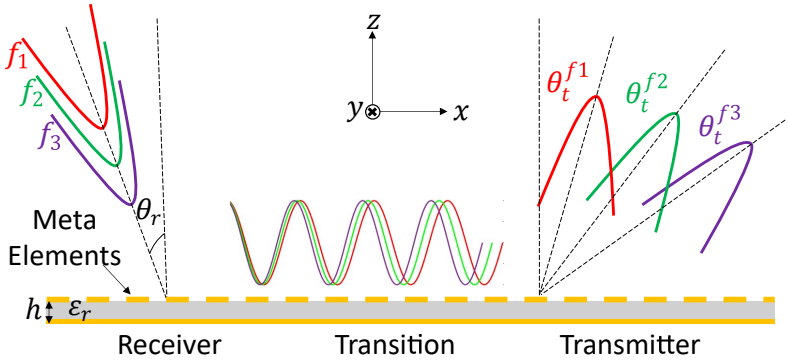

Figure 4.1: The functionalities of the proposed Metaprism, which includes SPW to SW conversion, SW guidance and beam-steering.

provides a summary of the conclusions and insights derived from this work.

4.1 Working Principles and Design of Metaprism

4.1.1 Problem Geometry

Fig. 4.1 shows the geometry and illustrates the fundamental working principle of the MTP proposed in this paper. The planar MTP is placed on the $xy-$plane of a Cartesian reference system. A linearly polarized incident wave impinges on the MTS at a pre-defined angle with an arbitrary amplitude distribution. This incident beam is envisioned as originating from a base transceiver station (BTS) and it has a frequency bandwidth capable of accommodating multiple subchannels, which will ultimately be rerouted to different users. Obstruction-induced masking effects (e.g., due to buildings) confine the beam propagation to a finite portion of the MTP, denoted as the receiving section. The key challenges within this segment lies in effectively collecting the incoming power and transferring it to a surface wave, while minimizing losses due to scattering. In this respect, maintaining consistent conversion efficiency across the whole frequency band poses a challenge, due to the inherent dispersion of the modulated MTS, which should be minimized in this receiving section.

The transition section is intended to collect the SW from the receiving section and guide it along $+x-$axis without radiation while progressively adjusting its wavenumber to match the one supported by the transmitting section. Finally, the transmitting section is designed to emulate the performance of a high frequency scanning rate LWA by using a highly dispersive MTS. In general, the frequency dispersion of printed MTSs can be easily controlled through the characteristics of the substrate. However, the challenge here is that the choice of the substrate will also affect the receiving section, for which frequency dispersion must be minimized. For this reason, the shape and size of the meta-elements will be used to control the dispersion, as well as the leakage constant.

4.1.2 Overview of Design Process for SW-SPW Conversion

This section provides a succinct overview of the SW to SPW conversion methodology employing modulated impedance, based on our adaptation of Oliner's Method to non-uniform modulation and PIBC. Recognizing the reciprocal nature of SPW to SW conversion, the design process revolves around designing SW to SPW converters, adaptable to reverse scenarios.

For implementation, a patch-type MTS is considered due to its compatibility with low-cost microstrip technology. This structure comprises infinitesimally thick metallic sub-wavelength patches printed on a planar grounded dielectric characterized by height h and dielectric constant ε_r. The patches are periodically modulated to achieve SW-SPW coupling. Considering the case of linearly polarized waves, common in communication models, the patches are accordingly modulated in one direction ($x-$axis) and remain invariant in the other ($y-$axis). The electromagnetic behavior of the printed layer of patch-type MTS is accurately modeled using the penetrable impedance boundary condition (PIBC), $X(x)$.

For an array of uniform patches, represented by constant reactance $X(x) = X^{(0)}$, the structure supports a TM-polarized SW with with currents $J(x) = J^{(0)}e^{-jk_x x}$. The SW is a slow wave with transverse propagation constants $k_x = \beta_{SW} > k_0$, where k_0 is the free space wavenumber, and purely imaginary longitudinal propagation constant k_z. The transverse resonance equation of the structure, given in (2.2), allows characterization of the dispersive quality β_{SW} of SW at frequency point $k_0(\omega)$. In the literature, several methods exist to evaluate X for a particular dimensions of a patch (denoted as unit cell).

Typically, a source-generated SW, supported on a constant impedance surface with a specific propagation constant $k_x^{(n)} = \beta_{SW}$, undergoes transformation upon entering a modulated structure. This transformation results in a wave represented as an infinite series comprising harmonics, specifically termed Floquet wave (FW) modes. Notably, the propagation constant of the n^{th} FW mode is defined as $k_x^{(n)} = \beta_x^{(0)} + 2\pi n/d + \alpha_x$. For proper design, one of the FW modes (usually $n = -1$) enters the visible (radiating) region accompanied by a leakage constant α_x, implying a power transfer from SW to LW . Achieving precise distributions of $\alpha_x(x)$ and $\beta_x^{(-1)}(x)$ profiles across the x-aperture is essential in realizing the desired SW-SPW conversion.

The design process follows a specific sequence: first, extracting the magnitude $A(x)$ and phase $\phi(x)$ of the aperture field from the intended radiation pattern. Next, deriving $\alpha(x)$ and $\beta_x^{(-1)}(x)$ from $A(x)$ and $\phi(x)$. Subsequently, obtaining local modulation indexes $M_n(x)$ and period $d_n(x)$ from $A(x)$ and $\beta_x^{(-1)}(x)$. Finally, calculating the overall impedance profile $X(x)$ through its closed-form Fourier series expression given in Eq. (4.1).

$$X(x) = \sum_{q=-n}^{n} X^{(q)} M_q(x) \exp\left(-j\phi_q\right) \exp\left(-jq \int_0^x \frac{2\pi}{d(x')} dx'\right) \quad n = 3 \tag{4.1}$$

Each parameter in Eq. (4.1) plays a distinct role in the conversion (or radiation) process. The number of Fourier terms, which is $2n+1$, is chosen to be 7, as it covers almost all the cases of practical interest. Parameters M_q and d are associated with α and θ, respectively. Relevant to our study, the phase constant $\beta_x^{(-1)}(x)$ predominantly relies on $X^{(0)}$ with adjustement provided by $d(x)$. Once $X(0)$ is selected, the dispersion equation $\beta_x = \beta_x(\omega)$ is obtained from (2.2).

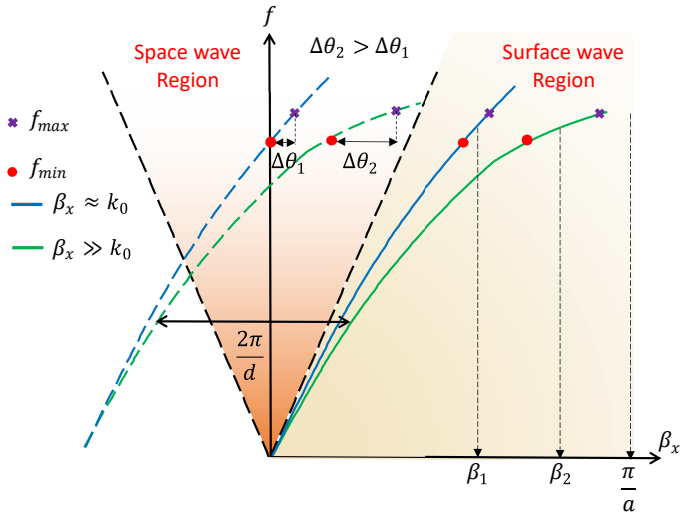

Figure 4.2: Dispersion diagram of TM modes $(0, -1)$ supported by patch type MTS characterized by microperiod (a) and macroperiod (d).

4.1.3 Dispersion Diagram

The dispersion diagram serves as a valuable tool for analyzing the frequency dispersion of a MTS. For modulated MTSs, we consider the dispersion curve associated with the average reactance $X^{(0)}$.

As an illustrative example, the blue and green continuous lines in Fig. 4.2 depict the dispersion curves of two SWs supported by MTSs with different values of penetrable reactance $X^{(0)}$ and the same unit cell size a. In particular, the green curve is associated to a lower absolute value of $X^{(0)}$ (i.e. a larger capacitance), and therefore it exhibits a lower slope, which corresponds to a lower group velocity v_g. The values of β_x at two frequencies (f_{min}) and (f_{max}) delimiting the operative bandwidth can be linked each other by the following equation, using a first order Taylor-type linear approximation:

$$\beta_x(f_{max}) \simeq \beta_x(f_{min}) + \frac{2\pi\Delta f}{v_g} \tag{4.2}$$

where $\Delta f = f_{max} - f_{min}$ and v_g is the group velocity at the minimum frequency. Equation (4.2) clearly indicates that the lower the group velocity, the greater the frequency dispersion of the structure.

When a periodic modulation of period d is introduced, the dispersion curve of the dominant mode is almost unperturbed, while other replica shifted by integer multiples of $(2\pi)/d$ appear. In particular, the curves relevant to the -1-indexed mode are shown in Fig. 4.2 by the dashed lines. Part of these curves falls within the visible region (VR), delimited by the two dashed black lines. For a given frequency, each point in the VR corresponds to a different LW pointing angle θ, referred to hereafter as the *scanning angle*, according to the relationship $\beta_x^{(-1)} = k_0 \sin(\theta)$. The relationship between the maximum angle $\theta_{max} = \theta(f_{max})$ and the minimum angle $\theta_{min} =$

$\theta(f_{min})$ of the scanning range is therefore:

$$f_{max}\sin\theta_{max} - f_{min}\sin\theta_{min} \simeq \frac{c_0}{v_g}\Delta f \tag{4.3}$$

where c_0 is the speed of light in free space. Eq. (4.3) shows that a lower group velocity (i.e a greater dispersion) leads to a larger angular scanning. The implication is that, for an effective MTP implementation, a low group velocity is required in the receiving section, while a high group velocity is needed in the transmitting section.

4.2 Numerical Calculations and Results for Metaprism

In this Section, we illustrate the design of a MTP operating at a central frequency of 26 GHz (5G mmWave band) with a bandwidth of 500 MHz. For MTS implementation, we consider a grounded substrate with relative dielectric constant $\epsilon_r = 6$ and height $h = 0.508$ mm. A modulated MTS implemented with printed elements exhibits a double periodicity scale [10]. The sub-wavelength micro-period (a) pertains to the constitutive unit cell, and is used to synthesize the desired homogenized penetrable impedance. On the other hand, the macro-period (d) is used to implement the local modulation, under the assumption of homogenized impedance. Following the conclusion of Section 4.1.3, different average reactance values are chosen for the receiving and the transmitting section, with the first one being much bigger in magnitude. In the transmitting section, the geometry of the patch elements plays a fundamental role in the determination of the frequency dispersion properties, as illustrated in the next section.

4.2.1 Dispersion Analysis of the MTS Unit Cell

This Section discusses the choice of the patch geometry for obtaining enhanced frequency dispersion in the transmitting section. As illustrated in Fig. 4.2, the dispersion curve becomes highly dispersive when β_x approaches the limit of the first Brillouin zone $\beta_x \approx \pi/a$. However, in practice, that region is also characterized by large sensitivity to fabrication inaccuracies and possibly enhanced losses. As a compromise, aiming at a unit cell size in the range $[\lambda/10, \lambda/5]$, a representative wavenumber for the transmitting section can be $\beta_x = 1.85k_0$, which, according to (2.2), corresponds to $X^{(0)} = -50\ \Omega$.

An H-shaped patch, whose geometry is reported in Fig. 4.3, is chosen for the unit cell. This unit cell is first rigorously analyzed in a periodic environment through the spectral method of moments (MoM) formulated in [92]. After identifying different combinations of geometrical parameters providing the desired equivalent reactance at the working frequency, frequency dispersion is investigated.

Table 4.1 summarizes the results of our numerical investigations. The dispersion characteristics are quantified by $\frac{\Delta f}{\Delta\beta_x}\cdot\frac{2\pi}{c_0} \simeq v_g/c_0$, calculated using our MoM routine. Data from Set I show that, for a square unit cell ($a = b$), increasing the size leads to a larger dispersion, as increasing a brings the operation point on the dispersion curve closer to the edge of the first Brillouin zone. Data from Set II show that a distinctive feature of the H-shaped patch is that, for a given unit cell size, increasing the parameter l_y instead of l_x leads to a greater dispersion. Finally, data from set III explore the impact on dispersion of adopting a rectangular unit

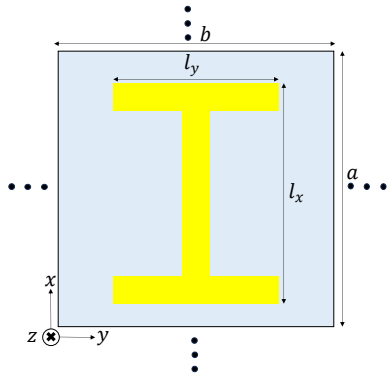

Figure 4.3: Geometry of the H-shaped patch unit cell designed to support TM SW propagating along $x-$axis.

cell instead of a square one. As expected, for a fixed length of l_y, a larger side (a) along the propagation direction, accompanied by a larger value of l_x, increases the dispersion, although the difference is less remarkable than for the previous two sets.

Table 4.1: Group velocity as a function of geometrical parameters for the H-shaped patch.

Input Parameters $f_c = 26\ GHz$, $\epsilon_r = 6$, $h = 0.508\ mm$, $X^{(0)} = -50\ \Omega$				
Set I				
$\boldsymbol{a(mm)}$	$\boldsymbol{b(mm)}$	$\boldsymbol{l_x(mm)}$	$\boldsymbol{l_y(mm)}$	$\boldsymbol{v_g/c_0}$
1.2	1.2	1.15	1.15	0.229
1.7	1.7	1.3	1.3	0.115
Set II				
1.7	1.7	1.17	1.6	0.092
1.7	1.7	1.6	0.88	0.204
Set III				
1.4	1.7	1.21	1.3	0.157
1.7	1.4	1.34	1.3	0.134

4.2.2 Full-Wave Analysis of Patch-type MTP Implementation

This Section presents the design and full wave simulation of a planar MTP. The planar structure extends along the xy-plane and is modulated along the x-axis. The incoming signal is here

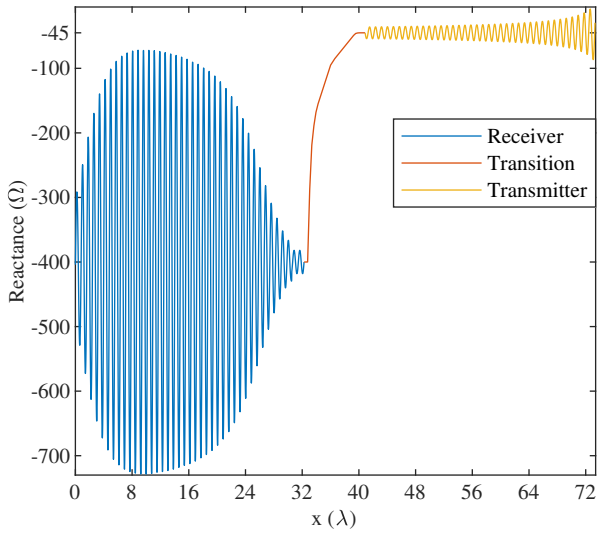

Figure 4.4: Synthesized reactance profile for the Metaprism.

modeled as a Gaussian-beam waveform impinging from the direction is set to $\theta_r = -10°$, leading to the following amplitude distribution for the incident field on the MTP plane

$$A(x) = Ae^{-(x-L/2)^2/2\sigma^2} \tag{4.4}$$

with a beam-waist of $\sigma\sqrt{2} = \sqrt{2} \times 16\lambda/3$. This model describes a scenario where an external obstacle produces a partial masking of the field radiated by the BTS, so that only a portion of the MTS is exposed to the impinging wave.

The length of the receiver section is set to $L_r = 32\lambda$. For this section, the tangential wavenumber $\beta_r^{(0)} = 1.08k_0$ is chosen to guarantee low dispersion. Similarly, for the transmitter section, the length is set to $L_t = 32\lambda$, while the tangential wavenumber is chosen to be $\beta_t^{(0)} = 1.98k_0$ to enhance frequency dispersion. The transmission angle is set to 45° for the central frequency. Finally, the transition section is required to progressively adapt the SW wavenumber in the receiving section to the one of the transmitting section. To ensure a smooth matching while keeping the length of the transition section limited, we set the length to $L_{tm} = 9\lambda$. Consequently, in this section the SW wavenumber varies with a constant gradient of $0.21k_0$ per λ.

The penetrable reactance profile ($X(x)$) synthesized by applying Eq. (4.1) with the above input parameters is shown in Fig. 4.4. The receiver, transition, and transmitter reactances are represented in blue, orange, and yellow lines, respectively. The average reactance for the receiver and transmitter sections are $X_r^{(0)} = -400\Omega$ and $X_t^{(0)} = -45\Omega$, respectively, while the transition profile is non-modulated and is designed to gently transition from the first average reactance to the second one.

As a next step, the synthetized reactance profile is implemented by H-shaped patches. Based on the analysis carried out in Section 4.2.1, the implementation of the reactance profile for the

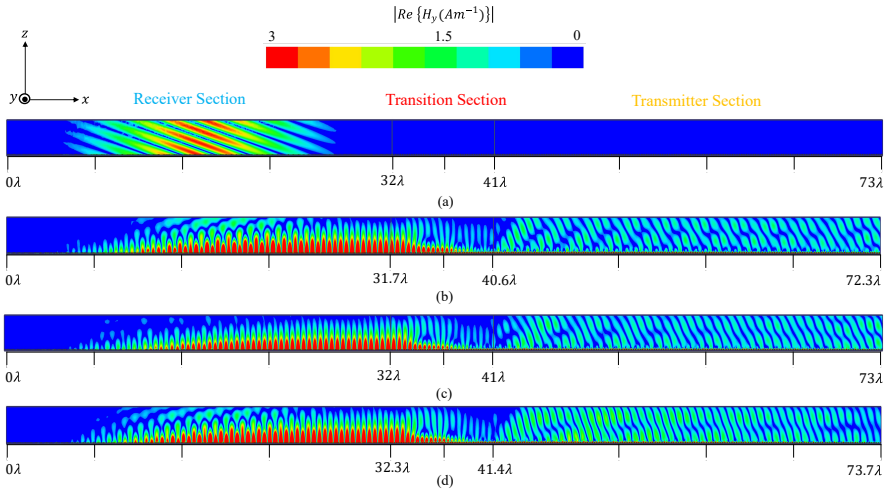

Figure 4.5: Simulated H-Field for the Metaprism. (a) Incident field. (b) Scattered field at 25.75 GHz. (c) Scattered field at 26 GHz. (c) Scattered field at 26.25 GHz.

receiver section requires the use of low values of l_y and high values of l_x. Conversely, the transmitter section requires higher values of l_y. Moreover, rectangular unit cells are used for the receiver section, with a smaller side along the propagation direction, to achieve lower dispersion and, thus, increased angular stability. More specifically, based on the dispersion analysis, the dimensions of the unit cells for the receiver and transmitter sections are set to 1.2×1.7 mm^2 and 1.7×1.7 mm^2, respectively. The number of patch elements for the receiver, transition, and transmitter sections are 310, 58, and 220, respectively.

Full-wave simulations of the resulting structure are finally performed using the Ansys HFSS software package. There, perfect magnetic boundaries are placed orthogonal to the y direction exploiting the periodicity along the y-axis, and the TM nature of the wave,

Fig. 4.5 depicts the magnitude of the incident tangential magnetic field (H_y) obtained at f_c from the simulation. Fig. 4.5 (a) shows the incident field at the central frequency f_c, corresponding to the scattered field reported in Fig. 4.5 (c). Fig. 4.5 (b) and (d) show the scattered field at the minimum and maximum frequency of the considered band, respectively.

In the scattered field pictures we can see the SW propagating along the x-axis with a gentle progressive increase in magnitude over the receiver section, due to the gradual conversion of power density from the impinging Gaussian beam to the local SW. Furthermore, it is observed that as the SW crosses the transition section, it becomes increasingly confined to the surface, indicating an increase in its SW wavenumber. Finally, a radiated SPW emerging from the transmitter section in a frequency dependent direction is observed.

Table 4.2 shows the conversion efficiencies at different frequencies across the considered bandwidth. In this table, the symbols have the following meaning:
P_{in} = Power of the impinging SPW
$P_{SW}^{(rx)}$ = Power of SW exiting the receiver section
$P_{SW}^{(tx)}$ = Power of SW exiting the transition section

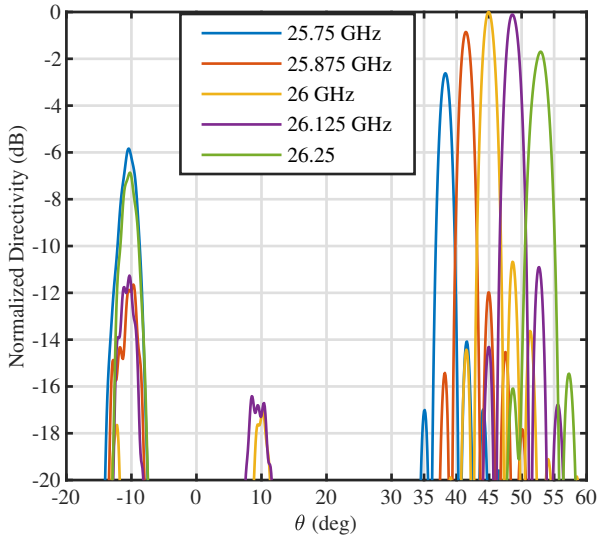

Figure 4.6: Normalized directivity pattern for the Metaprism across the frequency band.

$P_{SPW}^{(tx)}$ = Power of SPW radiated by the transmission section

At the central frequency f_c, the incident Gaussian beam carries a power $P_{in} = 1$ W, and the SW power calculated in the $x = 32\lambda$ plane is $P_{SW}^{(rx)} = 0.936$ W, resulting in an SPW-SW conversion efficiency of 93.6%. The radiated power calculated in the $z = 1.5\lambda$ plane is $P_{SPW}^{(tx)} = 0.846$ W, resulting in an overall SPW-SW-SPW conversion efficiency of 84.6%. The overall efficiency drops by 27.6% at the lower edge of the bandwidth.

Table 4.2: Calculated Conversion Efficiencies for the Metaprism

Freq. (GHz)	**25.75**	**25.875**	**26**	**26.125**	**26.25**
$P_{SW}^{(rx)}/P_{in}$	63.1%	86.2%	93.6%	84.4%	72%
$P_{SW}^{(tx)}/P_{in}$	60.8%	83%	90%	81.3%	69%
$P_{SPW}^{(tx)}/P_{in}$	57%	76%	84.6%	76.2%	67.5%

Fig. 4.6 illustrates the simulated directivity patterns at five frequencies across the considered bandwidth. For each frequency, along with the intended transmitted beam a specularly reflected beam is also observed, due to non-perfect conversion of the impinging wave. At f_c, the ratio of the transmitted lobe to the reflected lobe is -17.8 dB. Importantly, the pointing angle of the main beam scans the range of 14.6° (from 38.3° to 52.9°) across the bandwidth. These results clearly demonstrate the MTP scanning capability, thus, validating the design.

4.2.3 Comparison with a Non-specular Reflective Surface

Non-specular reflective surfaces based on MTSs currently constitute the prevalent technology for implementing RIS. Unlike the SW-based structure proposed here, in a MTS-based non-specular reflector the entire structure can collect the incoming SPW power and redirect it non-specularly thanks to a linear variation of the reflection coefficient phase. This implies a higher aperture efficiency at a single frequency. However, this solution presents a limited capability for physical layer frequency multiplexing, as will be shown in this section. The standard approach to achieve AR employs the generalized Snell's law as detailed in [16]. For given intended incidence (θ_i) and reflected (θ_r) angles, this leads to the following design equation for the reactance $X_I(x)$ of the impenetrable impedance boundary condition (IIBC):

$$X_I(x) = Z_0^{TM} \cot\left[\frac{k_0 x}{2}\left(\sin\theta_i - \sin\theta_r\right)\right] \tag{4.5}$$

where $Z_0^{TM} = \zeta\frac{k_{z0}}{k_0}$, with $k_{z0} = k_0\cos\theta_i$, represents the TM free space impedance for the incident wave. In order to incorporate dispersion effects, and hence obtain better accuracy [18], the reactance of the IIBC in (4.5) is transformed into a penetrable reactance X_P on top of a grounded slab by:

$$X_P = \left[\frac{1}{X_I} - \frac{\epsilon_r \cot\left(k_0 h\sqrt{\epsilon_r - \sin^2\theta_i}\right)}{\zeta\sqrt{\epsilon_r - \sin^2\theta_i}}\right]^{-1} \tag{4.6}$$

In this case, the reflection angle is completely determined by the incidence angle, the frequency and the modulation period, with no additional degrees of freedom, as opposed to the MTP, where one can play with MTS dispersion (see Eq. (4.3)). Indeed, the angular range of frequency scanning in the band $[f_1, f_2]$ is given by

$$\Delta\theta_r = \sin^{-1}\left(\sin\theta_i - \frac{c_0}{f_2 d}\right) - \sin^{-1}\left(\sin\theta_i - \frac{c_0}{f_1 d}\right) \tag{4.7}$$

In order to numerically compare this solution with the proposed MTP, eqs. (4.5)-(4.6) are applied to obtain the reactance profile corresponding to $\theta_i = -10°$ and $\theta_r = 45°$ keeping the other input parameters (f_c, h, and ϵ_r) and excitation consistent with those of the SW-based MTP. Subsequently, an H-shaped patch-type MTS is designed based on this profile and simulated in HFSS. The structure length is kept the same as the length of the transmitter section of the SW-based MTS, i.e. 32λ. The simulated directivity patterns of the field scattered by the non-specular reflective surface-based MTS at different frequencies are shown in Fig. 4.7. As predicted by Eq. (4.7), the obtained frequency scanning range is around 1.5°, which is significantly smaller than that for the SW-based MTS.

4.3 Analysis and Design of a Bent MTS Guiding a SW

In this section, we investigate the design and analysis of a bent MTS for SW guiding. In scenarios where the system architecture requires it, the transition section must be capable of supporting

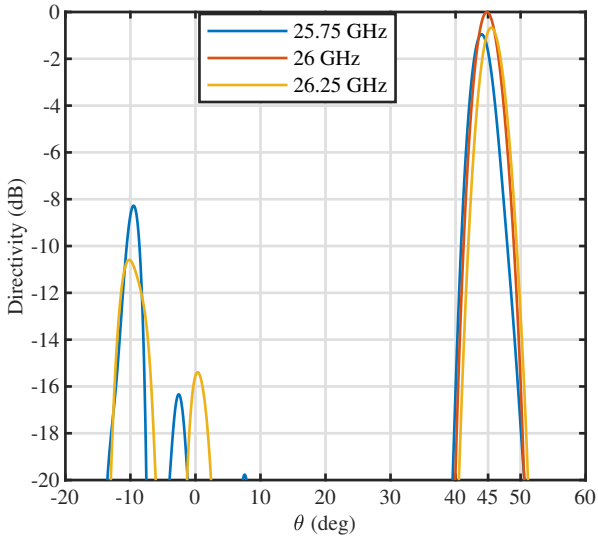

Figure 4.7: Normalized directivity pattern for the non-specular reflective surface-based MTS across the frequency band.

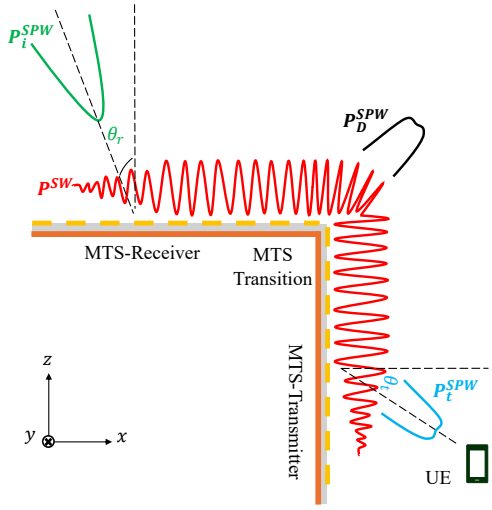

Figure 4.8: Illustration of the functionalities of the bent MTS system, which includes SPW to SW conversion, SW guidance around obstacle and re-radiation.

sharp bends. The key challenge is to ensure that the SW traveling through the bend experiences minimal power loss due to diffraction. In this study, we focus on the relationship between SW wavenumber and power loss due to diffraction at the bend. Our design strategy builds on the work by the authors in [93], who studied SW diffraction by an impedance wedge. Their findings

demonstrated that power loss due to diffraction decreases for impedance surfaces supporting SWs with higher wavenumbers. In this work, we leverage the fact that the electromagnetic behavior of an impedance surface can be replicated by its MTS implementation.

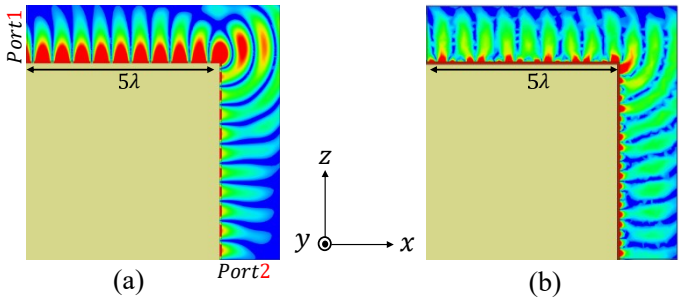

Figure 4.9: Simulated H-Field for uniform Bent-MTS. (a) $X^{(0)} = -300\ \Omega$ case. (b) $X^{(0)} = -25\ \Omega$ case.

Fig. 4.9 illustrates the HFSS simulation setup of an unmodulated MTS ($X(x) = X^{(0)}$) implementing the bent SW carrier. The structure is divided into two parts: the first part is oriented along the xy-plane with a length of 5λ along the x-axis, while the second part is oriented in the zy-plane with a length of 5λ, connected by a sharp 90° bend at $x = 5\lambda$. A SW propagates along the $+x$-axis and enters the MTS from $Port_1$ at $x = 0$. In the ideal case, as the SW traverses the bend, it continues its propagation along the $-z$-axis until reaching $Port_2$ at $z = -5\lambda$.

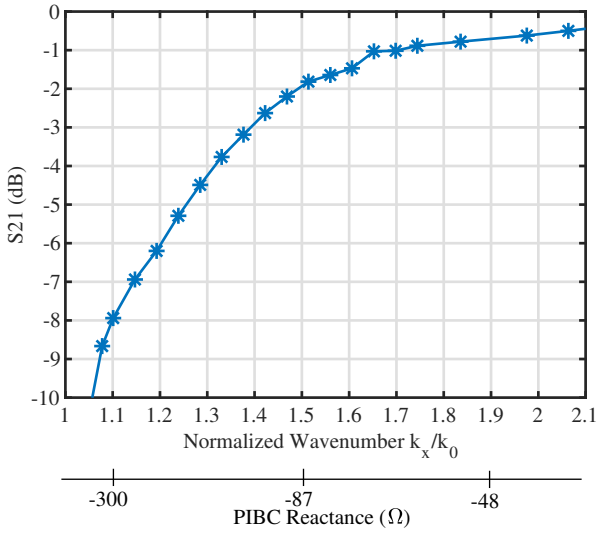

Figure 4.10: Extracted S_{21} for uniform Bent-MTS as a function of PIBC $X^{(0)}$ values.

Full-wave simulations are conducted for a uniform Bent-MTS with different PIBC values.

Notably, the SW dispersion, β_x, is inversely related to the PIBC, $X^{(0)}$, of the MTS. The calculated diffraction loss, S_{21}, shown in Fig. 4.10, demonstrates that diffraction loss is highest for large values of $X^{(0)}$ and lowest for smaller values of $X^{(0)}$. Furthermore, as $X^{(0)}$ decreases, the diffraction loss (in dB scale) initially decreases almost linearly until the value of $X^{(0)}$ that corresponds to a SW wavenumber of $\beta_x = 1.6k_0$. Beyond this point, the decrease in diffraction loss becomes more gradual as β_x continues to increase.

For more insight, the simulated magnetic field results for two MTSs are illustrated in Fig. 4.9. In the first case, $X^{(0)} = -300\,\Omega$, supporting a SW with propagation constants $\beta_x = 1.07k_0$ and $\alpha_z = -0.38k_0$ in the first part of the structure. In the second case, $X^{(0)} = -25\,\Omega$, the corresponding values of β_x and α_z are $2.15k_0$ and $-1.9k_0$, respectively. The simulated magnetic field results in Fig. 4.9 reveal greater diffraction for the first case, with S_{21} losses of -8 dB and -0.5 dB for the two cases, respectively. This difference is attributed to the tighter confinement of SW fields to the surface in the second case, due to larger attenuation along the z-axis, α_z, resulting in lesser power leakage to diffraction as the waves traverse the bend. These results suggest that a simple yet effective method of guiding SWs around the corner consists of using values of impedance corresponding to large SW wavenumber. In this connection, we can re-use results from the previous sections, where we demonstrated the ability to precisely achieve any desired value of the SW wavenumber on the patch-type MTS, guided by our MOM routine.

The approach described above is applied to design two examples of MTS with beyond-the-corner wave-routing capability. The receiver and transmitter sections are now on two different faces of a 90° wedge, with the transition section across the edge. Input parameters for the receiver and transmitter sections of the first example are kept identical from the planar MTP case. For this design, the transition section is slightly elongated, with its bent region designed to support SWs with a high wavenumber ($\beta_t^{(0)} = 1.98k_0$). The simulated $H-$field of the structure at the central frequency is shown in Fig. 4.12. We can see that the majority of the power incident on the xy aperture is collected, guided through the corner and finally radiated from the xz aperture. Based on the full-wave analysis, the calculated overall space-routing efficiency of the MTS implemented with H-shaped patches was 80%. The directivity pattern analysis (not included here for brevity) reveals that the radiation lobe corresponding to the re-routed wave is 13.4 dB higher than the diffraction lobe. Additionally, the bent metaprism design retains its frequency-scanning functionality over the operational bandwidth.

Building on the previous example, the next design focuses on a more challenging scenario: re-routing SPWs that impinges normal to the receiver section and radiates normal to the transmitter section. This configuration further tests the flexibility and robustness of the bent-MTS approach. The input parameters for the receiver and transmitter sections are kept identical: $f_c = 26\,\text{GHz}$, $\epsilon_r = 6$, $h = 0.508\,\text{mm}$, $L_r = L_t = 32\lambda$, $\theta_i = \theta_t = 0°$, $\beta_r^{(0)} = \beta_t^{(0)} = 1.82k_0$, and the aperture amplitude distribution $A_r(x) = A_t(x) = Ae^{-(x-L/2)^2/2\sigma^2}$, with $\sigma = \frac{16}{3}\lambda$.

To ensure efficient wave-guiding through the corner, the transition section requires a high wavenumber value of $\beta_{bent}^{(0)} = 2.15k_0$. The synthesized impedance profile for the MTS structure along the xy-plane is presented in inset of Fig. 4.11, with the xz-plane profile being its mirror image. The simulated magnetic field ($H-$field) of the structure, shown in Fig. 4.12, demonstrates efficient collection of power on the xy-aperture, guiding it across the bent region, and radiating it from the xz-aperture. The full-wave analysis quantifies the performance: the overall space-routing efficiency reaches 93% for homogenized impedance surfaces, and 81% for

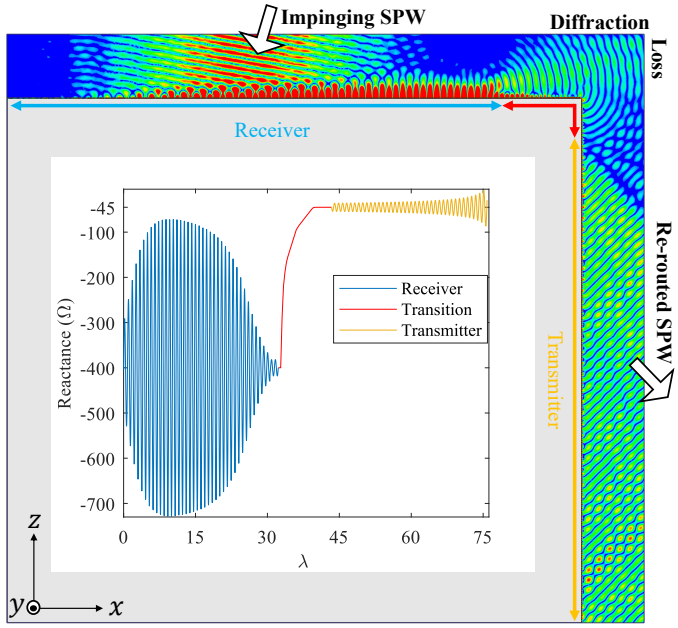

Figure 4.11: Simulated H-field for the MTS-bent-I at a 90-degree angle at the central frequency. Inset: Impedance profile.

implementations using microstrip patch-based realizations.

4.4 Conclusion

The designs of a passive non-reconfigurable MTS device able to re-route different subcarriers of an incident beam towards different users (Metaprism) has been proposed. The device exploits a double conversion process, from SPW to SW and back to SPW, and leverages the dispersion properties intrinsic to SW propagation. Moreover, it has been demonstrated that appropriate dispersion control can minimize diffraction losses for SW propagating along a non planar path, thereby facilitating the rerouting of SPW around the wedges of buildings.

The proposed concept was implemented using readily accessible microstrip technology, featuring metallic patches on grounded dielectric. For the initial design, the structure has been modeled using PIBC, and the relevant modulation parameters are determined based on the requirements of SW-SPW conversion at the center frequency and dispersion properties over a given bandwidth. Then, the dimensions of patch elements are determined through detailed numerical dispersion analysis of the patch unit cell. Importantly, these design steps can be adapted for other fabrication technologies resorting to an IIBC model.

Full-wave analysis has been conducted on the patch-type MTSs using HFSS simulator for validation. In the case of the Metaprism, the overall transmission efficiency was found to be 84.6% at the central frequency of 26 GHz, decreasing to 57% at the bandwidth edge (25.75

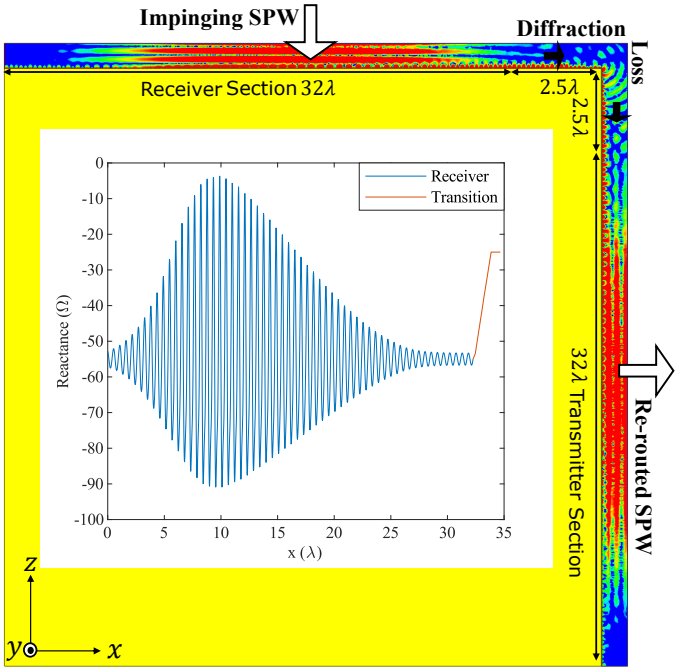

Figure 4.12: Simulated H-field for the MTS-bent-II at a 90-degree angle at the central frequency. Inset: Impedance profile.

GHz), with an angular scanning range of 14.6° over a 1.22% fractional bandwidth. Although the incoming signal was modeled as a Gaussian-beam waveform, the design approach can be generalized to accommodate any arbitrary waveform. For the sake of comparison, simulations were also performed for a MTS-based anomalous reflector. In that case, the calculated angular scanning range was 1.5° for similar parameters. Furthermore, the design of a Metaprism featuring a 90° bent was also presented, with the ability to receive an incident SPW at one plane and subsequently radiate the captured power from the perpendicular plane. In this case, full wave simulations showed an overall efficiency of 80%.

Based on the findings of this study, the proposed Metaprism concept shows potential for smart radio environment applications by enabling physical-layer frequency multiplexing. Additionally, frequency-dependent wireless signal rerouting can be applied in the wireless localization domain. Additional functionalities can be obtained by incorporating active reconfiguration into the SW-based MTS.

Chapter 5

Accurate Design of Reconfigurable Mushroom Metasurface

This chapter presents the design of reconfigurable modulated MTS for leaky-wave antennas and SW-RIS applications. The design of radiation properties of the MTS, from input surface-wave to leaky-wave, is based on periodic modulation of impedance surface. Tunable impedance modulation is achieved using varactors, with the entire device realized on a mushroom structure. The mushroom structure offers a key advantage: its metallic vias enable biasing of the varactors, effectively isolating the biasing network from the high-frequency electromagnetic layer.

For modulated MTS based LWA, the accuracy of homogenized impedance models in predicting the electromagnetic behavior of the selected implementation technology is crucial. Therefore, the rigorous investigation of this accuracy is the main objective of this chapter. We select two impedance boundary condition (IBC) to model the structure. A first model is based on an "opaque" impedance, defined by BCs at the MTS-air interface. While the second one uses a "penetrable" impedance sheet describing the homogenized BCs imposed by the metallic patches connected to wire medium.

In first part of the work, a simpler case of non-reconfigurable (without varactors) muhsroom MTS is studied. The two IBC models are employed in the standard double-scale synthesis approach to design modulated MTS. In a first step, the unit cell of MTS (assuming local uniformity) is modelled using the selected impedance homogenized model. In a second step, the homogenized impedance is periodically modulated to generate target LW's propagation constant based on the adiabatic Floquet-wave model.

To evaluate the accuracy of the impedance modulation models, full-wave simulations (using HFSS) were conducted on several MTS designs. The primary evaluation criterion is the ability of the impedance models to predict the leaky-wave (LW) leakage and phase constant values, tested across a range from low to high values. Additionally, for more rigorous assessment, MTS LWA designs were created to radiate at broadside, as the suppression of the stopband in this region relies on the accurate realization of an advanced impedance profile. The full-wave simulation results reveal that the OIBC-based mushroom MTS model performs well for low to mid-range values of the complex propagation constant. However, as the leakage constant increases, the OIBC model begins to overestimate its values compared to those obtained from full-wave simulation. Similarly, as the phase constant increases, the accuracy of the OIBC model in predicting the leakage constant diminishes, and its effectiveness in suppressing the OSB decreases. A similar trend was observed for the PIBC model, with improved accuracy when operating with large phase constant.

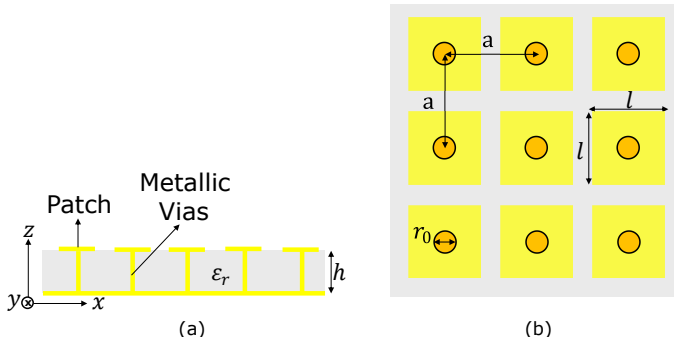

Figure 5.1: Geometry for the mushroom MTS. (a) Side view. (b) Top view.

In the last part of the work, the design of a reconfigurable mushroom MTS is presented. Here, the MTS unit cell is composed of two adjacent symmetrical mushrooms, connected by a varactor at one edge. The MTS LWA is designed to achieve continuous beam scanning by adjusting the varactor values, which correspond to different impedance profiles. Building upon the findings of modulated mushroom MTS, a low operating wavenumber is chosen to optimize performance. The key contribution of this design lies in its ability to scan seamlessly across a wide angular range without encountering radiation nulls at broadside. Additionally, the use of the mushroom structure ensures that the biasing vias are effectively integrated into the design, addressing a crucial factor that becomes significant at higher frequencies. This aspect will be particularly valuable for future work, as the effects of biasing vias cannot be overlooked in advanced high-frequency designs.

5.1 Homogenized Impedance Models for Uniform Mushroom MTS

5.1.1 Problem Geometry

Figure 5.1 illustrates the geometry of the mushroom structure under investigation. The structure consists of an array of symmetrical metallic patches printed on a grounded dielectric substrate, with the height and dielectric constant represented by h and ϵ_r, respectively. Each patch is connected to the ground through metallic vias located at the center of the patch. The distance between adjacent patches, denoted by a, is equal to the distance between adjacent vias. In literature, wires embedded in grounded dielectric is refereed to as wire medium. In this study, we focus on the case of TM-polarized surface waves, which is the first mode supported by a uniform mushroom structure. The propagation of the TM surface wave (TM-SW) is considered along the x-axis.

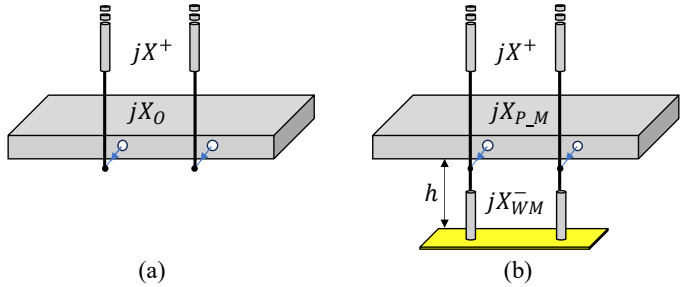

Figure 5.2: Transmission line models of Mushroom MTS. (a) OIBC Model. (b) PIBC model.

5.1.2 Opaque IBC

Opaque IBC is a versatile homogenization model suitable for a wide range of metasurface (MTS) configurations, as it is defined at the interface between air and the top layer of the MTS structure. In this case, the OIBC is derived by relating the average tangential electric field to the average tangential magnetic field at $z = 0^+$. This model accounts for the electromagnetic contributions from both the metallic patches and the grounded wire medium (WM).

$$E_x(z = 0^+) = jX_O H_y|_{0^+} \tag{5.1}$$

The dispersion relationship between the opaque surface reactance, jX_O, and the transverse wavenumber (β_{SW}) of the propagating TM surface wave (TM-SW) can be derived using the transverse resonance technique at the MTS-air interface. This relationship is expressed as follows:

$$X_O = -X^+ = \zeta \frac{\sqrt{\beta_{SW}^2 - k_0^2}}{k_0} \tag{5.2}$$

The corresponding equivalent transmission line model, which is based on equation (5.2), is depicted in Figure 5.2(a).

5.1.3 Penetrable IBC

In the following, we present the penetrable IBC model for uniform mushroom MTS, reproduced from the work covered in [88]. The key distinction between this and the previous model is that PIBC, denoted as X_{P_M}, accounts specifically for the contribution of the top patch layer, while the rest of the structure, the wire medium (WM), is modeled separately by X^+WM. This division of contributions is illustrated in the transmission line model shown in Figure 5.2(b). The values of X_{PM} and X^-_{WM} are retrieved by applying the TRE technique, as given in (5.3). Notably, X_{PM} exhibits capacitive characteristics, whereas X^-_{WM} is inductive for the TM mode.

$$\frac{1}{X^+} + \frac{1}{X^-_{WM}} + \frac{1}{X_{PM}} = 0 \tag{5.3}$$

where

$$\frac{1}{X^-_{WM}} = \frac{\varepsilon_{zz}^{TM} k_0}{\gamma_{TM}\eta_0} \cot(\gamma_{TM} h) + \frac{k_0(\varepsilon_{zz}^{TM} - \varepsilon_r)}{k_0\sqrt{\varepsilon_r}\eta_0} \coth(k_0\sqrt{\varepsilon_r} h) \tag{5.4}$$

$$(k_p a)^2 = \frac{2\pi}{\ln\left(\frac{a}{2\pi r_0}\right) + 0.5275} \tag{5.5}$$

$$\gamma_{TM} = \sqrt{k_z^2 + k_p^2 - k_0^2 \varepsilon_r^2} \tag{5.6}$$

$$\varepsilon_{zz}^{TM} = \varepsilon_r^2 \left(1 - \frac{k_p^2}{k_p^2 + k_x^2}\right) \tag{5.7}$$

A novel contribution of this work is the application of this model to the case of a modulated mushroom MTS, where k_x will take on complex values due to the impedance modulation. This extension is crucial for analyzing leaky-wave properties and surface-wave conversion in modulated metasurfaces.

5.2 Modelling of Modulated Muhsroom MTS

Once the structure has been homogenized by a impedance model, the next step is to synthesize impedance modulation profile for the MTS structure for desired leaky-wave properties. In this work, we employ synthesis procedure based on Floquet-wave expansion of waves on periodically modulated IBC. This procedure was covered extensively in Chapter 2, 3 where it was derived for PIBC modelled printed patches on grounded dielectric. To apply this synthesis process to mushroom MTS, we modify the system equation (3.9) for the OIBC, resulting in equation (5.8). Here, X is replaced with X_O, and X_{GF} with X_{GF-O}, where X_O and X_{GF} are defined in equations (5.1) and (5.11), respectively.

$$\sum_{q=-\infty}^{\infty} X_O^{(q)} J^{(n-q)} - X_{GF-0}\left(k_x^{(n)}\right) J^{(n)} = 0 \quad n = 0, \pm 1, \pm 2, .. \tag{5.8}$$

$$X_{GF-0} = -X^+ \tag{5.9}$$

The design procedure follows the same steps outlined in Chapters 2 and 3, where the target values for α_x and β_x are provided to the system equation (5.8). After solving the system, the modulation parameters are retrieved. Similarly, the synthesis equation for PIBC-modeled mushroom MTS is formulated as shown in (5.8).

$$\sum_{q=-\infty}^{\infty} X_{PM}^{(q)} J^{(n-q)} - X_{GF-PM}\left(k_x^{(n)}\right) J^{(n)} = 0 \quad n = 0, \pm 1, \pm 2, .. \tag{5.10}$$

where,

$$X_{GF-PM} = -\frac{X^+\left(k_x^{(n)}\right) X_{WM}^-\left(k_x^{(n)}\right)}{X^+\left(k_x^{(n)}\right) + X_{WM}^-\left(k_x^{(n)}\right)} \tag{5.11}$$

In the following sections, full-wave simulations will be performed to validate the accuracy of equations (5.8) and (5.10) in modeling modulated mushroom MTS.

5.3 Full Wave Analysis of Modulated Muhsroom MTS

For the numerical investigation, we selected high central frequency value of 26 GHz. This is motivated by the need to study the effects of biasing lines for reconfiguration MTS at this band. The values of mushroom MTS paramteres shown in Fig. 5.1 are $a = 0.65\ mm$ ($\lambda/10$), $r0 = 0.05\ mm$, $h = 0.508\ mm$ and $\varepsilon_r = 6$.

5.3.1 Unit Cell and Impedance Maps

In this section, full-wave simulations will be performed to validate the accuracy of equation (5.8) in modeling modulated mushroom MTS. Following the double-scale approach outlined earlier, we first establish a mapping between the impedance values, both PIBC and OIBC, and specific geometry of the mushroom MTS. To achieve this, we performed an eigenmode analysis using the HFSS solver on the mushroom's unit cell. This allowed us to compute the tangential wavenumber (k_x) associated with the TM polarized wave supported by the mushroom MTS. The calculated k_x values were then applied to equations (5.2) and (5.3) to derive X_O and X_{PM} for varying patch sizes l, as shown in Fig. 5.3. Notably, X_O exhibit an exponential behavior as a function of l. This phenomenon can be explained by (5.3), where increasing the value of l leads to a greater capacitive X_{PM} that approaches the inductive value of X_{WM}^{-}, resulting in resonance and consequently a significant increase in X_O.

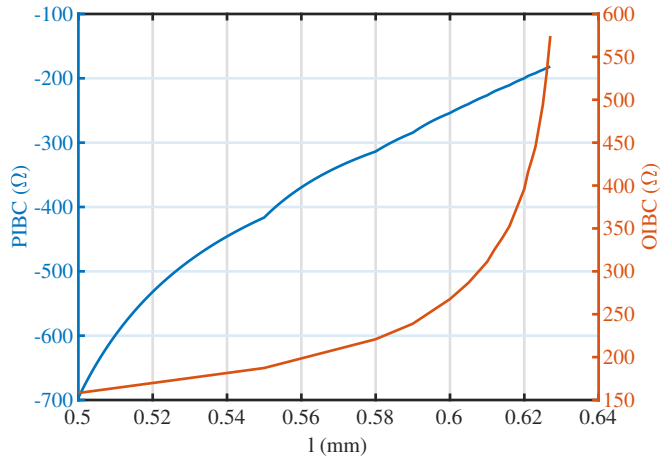

Figure 5.3: X_O and X_{PM} values of mushroom's unit cell as a function of parameter l.

5.3.2 Simulation Setup

To assess the accuracy of the impedance modulation models, full-wave simulations using HFSS were performed on several modulated MTS designs, with the setup illustrated in Fig. 5.4. The MTS LWAs were designed to meet specific target values for the leakage constant (α_x) and the

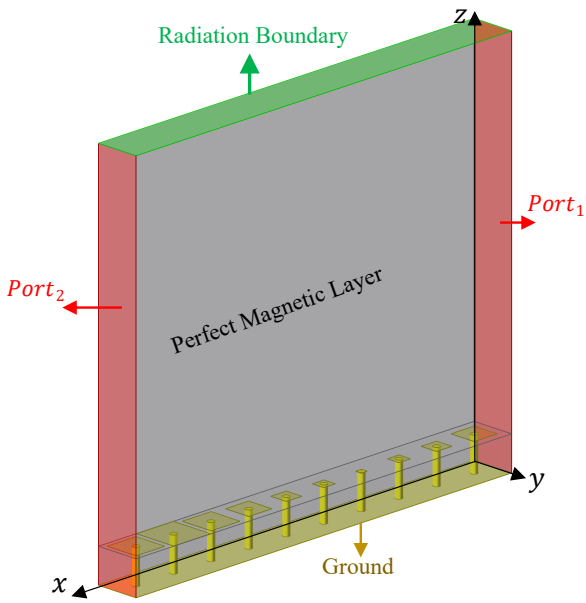

Figure 5.4: Simulation setup.

propagation constant (β_x), as detailed in Table 4.1. The values of α_x were derived by first calculating the surface wave input power (P_{in}) entering through $Port_1$ and the output power (P_{out}) exiting through $Port_2$. These values were then substituted into equation (5.12), which defines the relationship between α_x and P_{in} and P_{out}. The parameter L, representing the length of the MTS, was kept constant at 3λ. For the calculation of β_x, the simulated field data were exported and processed using the "generalized pencil-of-function method" to extract its value [94].

$$P_{out} = P_{in}\left(1 - e^{-2\alpha L}\right) \tag{5.12}$$

5.3.3 Opaque IBC Results

Using the OIBC model we created nine broadside radiating MTS-LWAs, with details provided in Table 5.1. The results show that the OIBC model is reasonably accurate in predicting the leakage properties when low ($\beta_x \leq 1.2k_0$) and mid ($\beta_x \leq 1.3k_0$) wavenumber values are used in the MTS design. However, it tends to overestimate α_x when designing for higher values ($\alpha_x \geq 9$) within this range. Notably, the MTS-LWA effectively suppresses the OSB, as indicated by S_{11} being below -15 dB. On the other hand, for higher operating wavenumber values ($\beta_x \leq 1.4k_0$), the OIBC model becomes significantly inaccurate, and strong OSB effects are observed when designing for high α_x.

Table 5.1: Performance summary of modulated MTS based on OIBC model

Sr.	*Predicted*		*Simulated*				
No.	$\boldsymbol{\alpha}$	$\boldsymbol{\beta/k_0}$	$\boldsymbol{\alpha}$	$\boldsymbol{\Delta\alpha(\%)}$	$\boldsymbol{\beta/k_0}$	$\boldsymbol{\Delta\beta(\%)}$	$\boldsymbol{S_{11}(dB)}$
1	3	1.198	2.99	1.84%	1.176	1.83%	-27
2	6	1.2	5.9	2.42%	1.185	1.17%	-23
3	9	1.2	7.3	19.6%	1.189	1.11%	-22
4	3	1.3	3.7	-22%	1.29	0.86%	-28
5	6	1.3	6.1	-0.5%	1.31	-1.26%	-26
6	9	1.3	7.5	17%	1.32	-1.67%	-22
7	3	1.43	0.5	83%	1.427	2.62%	-35
8	6	1.43	5	17.6%	1.416	1.15%	-14
9	9	1.43	0.3	94.4%	1.39	1.15%	-4.6

Table 5.2: Performance summary of modulated MTS based on PIBC model

Sr.	*Predicted*		*Simulated*				
No.	$\boldsymbol{\alpha}$	$\boldsymbol{\beta/k_0}$	$\boldsymbol{\alpha}$	$\boldsymbol{\Delta\alpha(\%)}$	$\boldsymbol{\beta/k_0}$	$\boldsymbol{\Delta\beta(\%)}$	$\boldsymbol{S_{11}(dB)}$
1	3	1.198	3.1	-3.75%	1.174	1.75%	-25
2	6	1.2	5.5	8.92%	1.21	0.17%	-18
3	9	1.2	7	22.3%	1.196	1.75%	-15
4	3	1.3	3.2	-6.6%	1.29	2.0%	-34
5	6	1.3	5.7	-5%	1.319	2.2%	-21
6	9	1.3	7.5	16.6%	1.326	1.45%	-15
7	3	1.429	3.2	-5.8%	1.398	2.62%	-21
8	6	1.429	5.5	6.07%	1.4	1.15%	-23
9	9	1.43	6.5	28.2%	1.397	1.15%	-19

5.3.4 Penetrable IBC Results

We repeated the simulations using the PIBC model, with a performance summary provided in Table 5.2. Similar accuracy patterns were observed for this model at low and mid β_x values. In this range, the PIBC slightly overestimates α_x compared to the OIBC model. However, the PIBC demonstrates significantly better accuracy than the OIBC model when the MTS-LWA operates at higher dispersive wavenumber values, with notably stronger suppression of the

OSB.

To provide further insight, we plotted the impedance profiles predicted by both models alongside the corresponding synthesized unit cell geometry profiles, characterized by the parameter l, for the target values $\alpha = 3$ and $\beta = 1.43k_0$. For the OIBC model, the synthesized l values exhibited minimal variation across the modulation period, leading to an almost uniform MTS structure. Consequently, the simulated α value was substantially lower than the predicted value. In contrast, the PIBC model produced a well-defined modulation profile for l, aligning closely with the expected values. The simulation results verified the improved accuracy of the α prediction using the PIBC model. Notably, PIBC model was significantly more accurate than OIBC model in a comparable analysis for MTS LWAs realized using metallic patches on a grounded slab (without vias).

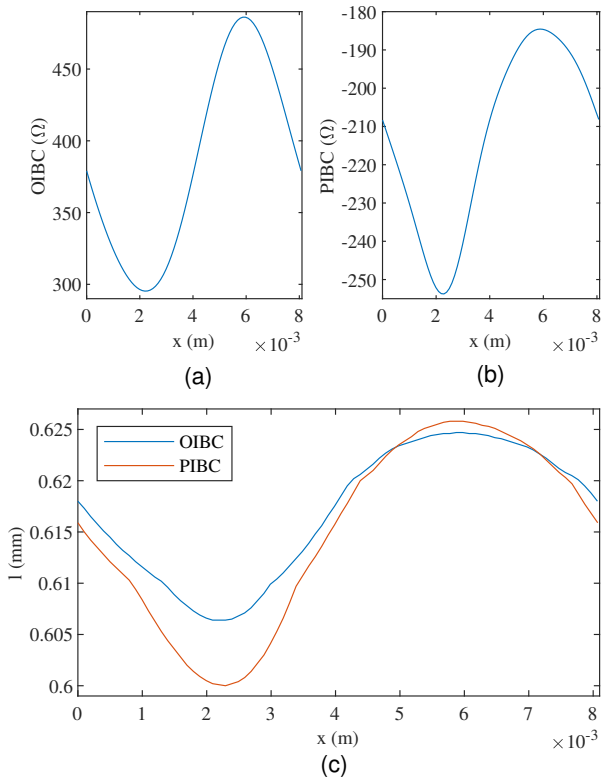

Figure 5.5: Mushroom MTS designed for $\alpha = 3$ and $\beta = 1.43k_0$. (a) Opaque IBC profile (b) Penetrable IBC profile (c) Synthesized unit cell parameter l profiles.

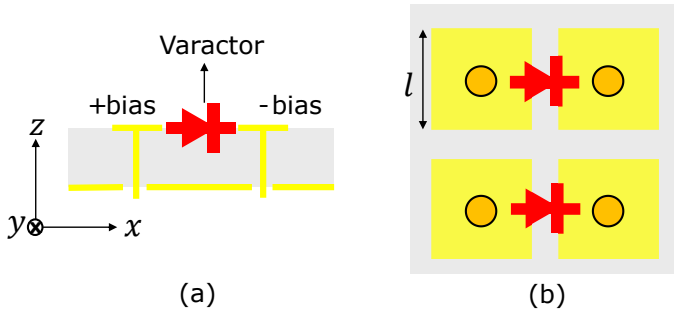

Figure 5.6: Geometry of reconfigurable Mushroom MTS.

5.4 Design and Analysis of Reconfigurable Muhsroom MTS

To create a reconfigurable version of the mushroom MTS, varactors are placed between adjacent patches, with one patch connected to a positive voltage source and the other to a negative source. In effect, the unit cell of the proposed MTS consists of two mushroom structures, as illustrated in Fig. 5.6. There are two primary approaches for designing reconfigurable MTS LWAs [95]. In the first approach, the patch geometry remains fixed, and impedance variation is achieved by adjusting the capacitance of the varactors. For each target beam angle, specific bias voltages are applied to individual varactors to implement the impedance profile corresponding to that angle. This approach offers a large scanning range and consistent aperture efficiency. However, the unique biasing required for each element results in a complex biasing network. In the second approach, each varactor receives the same bias voltage for any given beam scan angle, simplifying the biasing network. Here, impedance modulation is achieved by varying the patch geometry. As the varactor capacitance is adjusted, the operating wavenumber of the MTS LWA changes, thereby altering the radiating beam angle.

5.4.1 Unit cell and Impedance Maps

As a first step, impedance maps for the reconfigurable mushroom MTS are created by varying the varactor capacitance (C), calculated using the eigenmode setup approach outlined earlier. The parameters of the mushroom structure remain the same as in the static case, with the patch size fixed at $l = 0.32$ mm. Fig. 5.7 illustrates the impedance values (X_O and X_{PM}) of the reconfigurable mushroom as a function of C. Notably, the OIBC impedance X_O increases exponentially with the rise in C. Additionally, as expected for the reconfigurable case, the capacitive PIBC impedance X_{PM} is effectively controlled by variations in C.

5.4.2 Reconfigurable Mushroom MTS LWA

In the final part of this study, we present a reconfigurable MTS LWA designed for continuous beam scanning from $-30°$ to $30°$. Based on the analysis of the static mushroom MTS, the design operates at a low wavenumber of $1.2k_0$, where the OIBC and PIBC models are reasonably accurate and generate similar impedance profiles. For each beam angle, an impedance profile

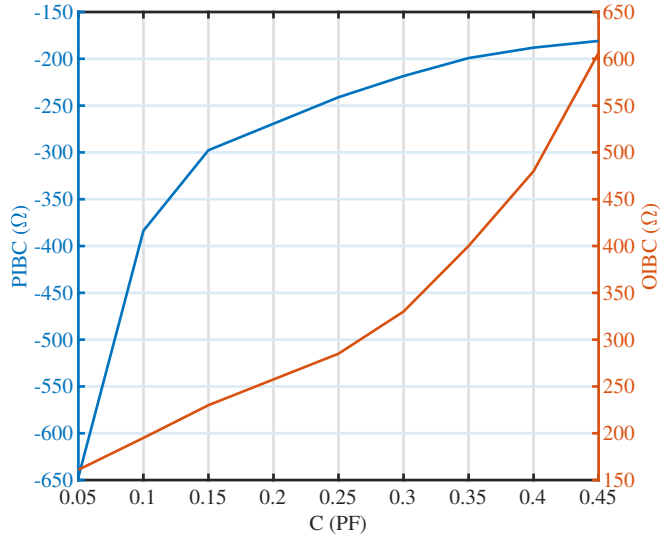

Figure 5.7: X_O and X_{PM} values of reconfigurable mushroom's unit cell as a function of parameter C.

is synthesized using our design procedure and realized through the reconfigurable mushroom MTS, following the impedance map shown in Fig. 5.7. The beam angle is determined by the modulation period. The length of the MTS along the x-axis is set to 16λ, primarily to limit simulation time, though in principle, longer MTS structures can be designed. In practical applications, the unit cell would also be repeated along the y-axis. For this length of (uniformly modulated) LWA, the target leakage constant is set to 6 m^{-1} to achieve a maximum radiation efficiency of 81%.

Fig. 5.8 shows the simulated realized gain pattern of the proposed mushroom MTS LWA. Similar to the static MTS case, a slight misalignment was observed between the target and simulated beam angles. Consequently, the MTS unit cell parameters were adjusted to achieve the desired target, requiring only two rounds of simulation-based optimization. Importantly, the radiation beam at broadside does not exhibit any OSB effects, which is crucial for our design. This result validates both the accuracy of our models and the effectiveness of the impedance synthesis approach.

5.5 Conclusion

We presented a systematic approach for designing reconfigurable mushroom MTS LWAs. By employing two impedance models, we demonstrated the ability to accurately predict and control the electromagnetic behavior of mushroom MTS structures. Our proposed reconfigurable MTS-LWA achieved continuous beam-scanning across a wide angular range without encountering OSB-related radiation nulls at broadside, validating the accuracy of the impedance-based design

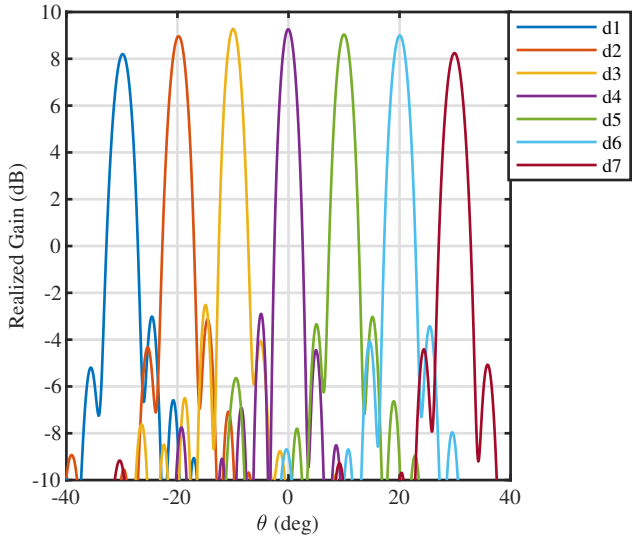

Figure 5.8: Simulated realized gain patterns for different states of reconfigurable mushroom MTS LWA. Here, $d1 = 6.73$, $d2 = 7.405$, $d3 = 8.3$, $d4 = 9.504$, $d5 = 10.47$, $d6 = 12.349$ and $d7 = 14.832$ with units in mm.

approach. Additionally, the integration of biasing vias within the reconfigurable LWA design addresses critical design challenges at mmWave frequencies, paving the way for more efficient high-frequency MTS-LWAs in future applications.

Chapter 6

Conclusions

6.1 Summary of Work

This thesis has presented the development of metasurface-based devices for wireless communication applications. The proposed devices can effectively collect wireless signal power and convert it into guided surface waves, which are then transported across the communication environment, bypassing obstacles before radiating toward the intended direction. Additionally, we demonstrated advanced functionalities, such as coverage for radio blind spots, physical-layer frequency multiplexing, multi-beam creation for MIMO channels, and electronic beam scanning. To achieve these results, several technical challenges were addressed and resolved, as detailed in Chapters 2 through 6 of this thesis. The following text summarizes the key conclusions drawn from this work.

Chapter 2 addressed the design of MTS-based SW-SPW couplers, with a particular focus on achieving efficient conversion of arbitrary propagating waveforms into SWs, while also enabling customized beamforming in the reciprocal SW-SPW case. The design method relied on modulated impedance surfaces. First, an analytical model was developed, establishing a direct relationship between arbitrary fields—described by the magnitude and phase distribution across the aperture—and the local impedance boundary conditions. This model allowed us to analyze constant-average, non-uniform sinusoidal impedance modulation for finite-length MTS.

For the design process, we introduced a simple yet effective routine for MTS synthesis, aimed at generating a target output field distribution. A key part of this approach was the derivation of novel designer's equations, linking the local impedance modulation index and period to the field's attenuation and phase constants. From these parameters, the final impedance profile was synthesized using a closed-form expression, enabling a direct design procedure. The effectiveness of this synthesis method was demonstrated through multiple MTS designs for various applications, all realized with metallic patches on a dielectric substrate.

Full-wave simulations confirmed the high conversion efficiency of these designs and their ability to produce the desired radiation patterns. Notably, this method was applied to develop a SW-based MTS-RIS for SRE applications. In this design, the first section of the MTS efficiently converted incoming wireless EM signals into SWs, while another section radiated a beam toward the intended user, demonstrating the system's versatility and effectiveness.

In Chapter 3, we expanded on the work from Chapter 2, focusing on the creation of MTS capable of receiving or transmitting propagating waves at any angle. We demonstrated the effectiveness of non-uniform modulation techniques in achieving high conversion efficiency. In

Chapter 2, the modulation function was based on a sinusoidal form due to its simplicity, allowing us to establish a direct design procedure. However, sinusoidally modulated impedance surfaces (SMIR) are known to suffer from open stopbands at broadside and the formation of undesired side-lobes when pointing towards forward angles.

To address these limitations, we developed an analytical model for the SW-SPW coupler using a Fourier series formulation to analyze any periodic impedance boundary modulation. Through this model, we identified the source of degradation in SMIR due to higher-order Floquet-wave modes. Subsequently, we proposed a solution based on sinusoidal modulation with two harmonics, demonstrating through our model that this approach is sufficient to suppress unwanted modes. The resulting MTS-based SW-SPW designs, developed from the synthesized impedance profiles, successfully suppressed the open stopband at broadside in both receiving and transmitting scenarios. Similarly, for forward angles, the suppression of higher-order modes was achieved.

Additionally, we demonstrated that by using sinusoidal modulation with three harmonics, we could further extend the forward angle range. Importantly, these new impedance modulation functions allowed us to derive closed-form expressions for creating constant-average, non-uniform impedance profiles for finite-length MTS. The analytical nature of the design process led to smoother impedance traces, making the realization of these designs with metallic patches on a dielectric substrate more feasible. Full-wave simulations of the patch-type MTS validated the high conversion efficiency and beamforming capabilities for both challenging broadside and forward angles.

The limitations of the SW-SPW coupling techniques presented in Chapters 2 and 3 are the following: they consider only linearly polarized waves and account solely for SPWs impinging along the direction of the modulation period, without addressing other incidence angles.

In Chapter 4, the SW-based MTS reflectors developed in previous chapters were leveraged to achieve innovative functionalities for wireless system applications. First, we introduced the design of an MTS capable of efficiently collecting wireless signals at a specified angle over a broad frequency range. These signals were converted into SWs, which were then re-radiated at frequency-dependent angles, enabling frequency multiplexing. Second, we demonstrated an MTS design that could bend SPWs around obstacles, facilitating signal rerouting across different planes. For both functionalities, we employed simple and effective design algorithms that manipulated and controlled the dispersion characteristics of SWs on the MTS.

The proposed concept was implemented using standard microstrip technology, featuring metallic patches on a grounded dielectric substrate, and accurately modeled using penetrable impedance boundary conditions (PIBC). The design process involved two key steps. First, the modulation parameters of the PIBC were defined based on the desired SW-SPW conversion at the center frequency, as well as the dispersion characteristics across the operating bandwidth. Second, the dimensions of the patch elements were optimized through a detailed numerical dispersion analysis of the unit cell. Validation was performed using full-wave simulations in the HFSS simulator, confirming the accuracy of the patch-type MTS design. Additionally, an MTS design featuring a sharp 90° bend was presented, capable of receiving an impinging SPW on one plane and reradiating the captured power from the perpendicular plane. Full-wave simulations demonstrated the MTS's ability to guide SWs around obstacles in the environment, further validating its effectiveness.

Chapter 5 addressed the challenges of adapting the MTS SPW-SW couplers developed in Chapters 2 and 3 for reconfigurable applications. To achieve this, we developed a reconfigurable meta-element using a voltage-controlled varactor embedded between two mushroom plates, with the mushroom's vertical pins serving as biasing lines. Impedance models were derived to describe the EM behavior of static, modulated mushroom MTS designed for SW to SPW conversion. Extensive full-wave simulations were conducted to evaluate the models' ability to accurately predict leakage and phase constants for radiating SPWs across various design targets.

Building on these findings, varactor properties were incorporated into the design process, enabling the development of a reconfigurable MTS-based SW-LWA with continuous beam-scanning capabilities. Full-wave simulations confirmed that the MTS-LWA achieved continuous beam-scanning over a broad angular range without encountering OSB-related radiation nulls at broadside, thus validating the robustness of the impedance-based design approach. Furthermore, the integration of biasing vias within the reconfigurable LWA design effectively addressed critical design considerations at mmWave frequencies, establishing a foundation for efficient, high-frequency MTS-LWAs in future applications. Notably, in the broader context of our SW-MTS RIS system, the proposed reconfigurable MTS could serve as the transmitter section, offering combined benefits of SW-based signal steering around obstacles and reconfigurable signal rerouting.

6.2 Future Directions

This thesis explored various aspects of metasurface technology, including analytical models, design methodologies, implementation, and numerical evaluations, all aimed at creating advanced devices for smart radio environment applications. Through this work, a robust foundation has been established, enabling a broad range of potential applications. However, there are many aspects of the research presented in this thesis that deserve further attention. Below, we outline some of the potential future research directions that could build upon this work.

In Chapter 2, we presented a systematic approach for synthesizing an isotropic impedance profile through sinusoidal modulation, achieving high SPW-SW conversion efficiency and SW-based beamforming. A key contribution was the derivation of an equation that established a direct relationship between design parameters and target field characteristics. Extending this method to dual-polarized and circularly polarized waves, commonly required in practical applications, would be a valuable direction for future research. For these cases, deriving direct design equations would require working with anisotropic impedance boundary conditions, presenting new challenges and opportunities in the design of versatile, polarization-adaptive metasurfaces. The presented analysis method can be extended to account for cases where the impinging SPW arrives from a direction different from that of the impedance modulation. This extension would allow the MTS to receive electromagnetic signals from any elevation and azimuthal angle relative to the metasurface.

In Chapter 3, we addressed the canonical issue of OSB-related radiation nulls at broadside in modulated impedance surfaces and LWAs, successfully resolving it through sinusoidal modulation with multiple harmonics. Extending this approach for dual-polarized MTS designs would be highly beneficial, especially for applications requiring enhanced polarization versatil-

ity. Additionally, our approach was implemented for metallic patches on a grounded dielectric substrate, where we found that two harmonics sufficed to achieve precise field control. For other implementation technologies, characterized by different Green's functions, further rigorous analysis would be necessary to determine the optimal number of modulation harmonics required to achieve comparable field control and performance.

In Chapter 4, we developed a broadband SW-based MTS capable of wide frequency beam-scanning for SRE applications. This design was realized using metallic patches on a grounded dielectric substrate. Exploring alternative implementation technologies with higher dispersion properties could be beneficial, especially for the transmitter section, to achieve even larger frequency-scanning capabilities. However, this approach would likely require a matching section to effectively interface the transmitter and receiver sections. Additionally, in the case of bent MTS designs, a conformal MTS approach could enhance performance by ensuring better alignment with the desired curvature, reducing transmission loss and increasing efficiency.

In Chapter 5, we developed a reconfigurable MTS for continuous beam-scanning applications, with an emphasis on precise impedance boundary-based modeling of a reconfigurable unit cell where a varactor was embedded within a mushroom structure. Future work could explore designing a more complex unit cell with an asymmetrical configuration, which would reduce the number of varactors needed along one principal axis, thereby simplifying the design and potentially enhancing efficiency. Additionally, a multi-layered unit cell could be investigated to achieve anisotropic boundary conditions, offering finer control over the polarization and propagation characteristics of the reconfigurable MTS. This approach could unlock new design possibilities for high-performance, adaptable metasurfaces tailored to complex operational requirements.

Bibliography

[1] R. W. Ziolkowski and N. Engheta, *Introduction, history, and selected topics in fundamental theories of metamaterials.* John Wiley Sons, Ltd, 2006, ch. 1, pp. 1–41. [Online]. Available: https://onlinelibrary.wiley.com/doi/abs/10.1002/0471784192.ch1

[2] S. Maci, "Electromagnetic metamaterials and metasurfaces: A historical journey," *IEEE Antennas and Propagation Magazine*, vol. 66, no. 3, pp. 84–101, 2024.

[3] F. Capolino, *Applications of metamaterials.* Boca Raton, FL, USA: CRC press, 2017.

[4] F. Yang and Y. Rahmat-Samii, "Introduction to surface electromagnetics," in *Surface Electromagnetics.* Cambridge, UK: Cambridge University Press, 2019, ch. 1, pp. 1–29.

[5] V. Asadchy, D.-H. Kwon, and S. Tretyakov, "Analytical modeling of electromagnetic surfaces," in *Surface Electromagnetics.* Cambridge, UK: Cambridge University Press, 2019, ch. 2, pp. 30–65.

[6] C. L. Holloway and E. F. Kuester, "Using generalized sheet transition conditions (gstcs) in the analysis of metasurfaces," in *Surface Electromagnetics.* Cambridge, UK: Cambridge University Press, 2019, ch. 3, p. 66–123.

[7] C. A. Balanis, "Artificial impedance surfaces," in *Balanis' Advanced Engineering Electromagnetics.* John Wiley Sons, Ltd, 2023, ch. 16, pp. 943–1021. [Online]. Available: https://onlinelibrary.wiley.com/doi/abs/10.1002/9781394180042.ch16

[8] A. Epstein and G. V. Eleftheriades, "Huygens metasurfaces via the equivalence principle: design and applications," *J. Opt. Soc. Am. B*, vol. 33, no. 2, pp. A31–A50, Feb 2016. [Online]. Available: https://opg.optica.org/josab/abstract.cfm?URI=josab-33-2-A31

[9] O. Quevedo-Teruel, H. Chen, A. Díaz-Rubio, and et al., "Roadmap on metasurfaces," *Journal of Optics*, vol. 21, no. 7, p. 073002, Jul. 2019. [Online]. Available: http://dx.doi.org/10.1088/2040-8986/ab161d

[10] E. Martini, F. Caminita, and Maci, Stefano, "Double-scale homogenized impedance models for periodically modulated metasurfaces," *EPJ Appl. Metamat.*, vol. 7, p. 12, 2020. [Online]. Available: https://doi.org/10.1051/epjam/2020010

[11] G. Minatti, D. González-Ovejero, E. Martini, and S. Maci, "Modulated metasurface antennas," in *Surface Electromagnetics*. Cambridge, UK: Cambridge University Press, 2019, ch. 7, pp. 231–271.

[12] D. Neshev and I. Aharonovich, "Optical metasurfaces: new generation building blocks for multi-functional optics," *Light: Science & Applications*, vol. 7, no. 1, p. 58, Aug 2018. [Online]. Available: https://doi.org/10.1038/s41377-018-0058-1

[13] W. L. Barnes, A. Dereux, and T. W. Ebbesen, "Surface plasmon subwavelength optics," *Nature*, vol. 424, no. 6950, pp. 824–830, Aug. 2003.

[14] J. B. Pendry, L. Martín-Moreno, and F. J. Garcia-Vidal, "Mimicking surface plasmons with structured surfaces," *Science*, vol. 305, no. 5685, pp. 847–848, 2004. [Online]. Available: https://www.science.org/doi/abs/10.1126/science.1098999

[15] J. He, T. Dong, B. Chi, and Y. Zhang, "Metasurfaces for terahertz wavefront modulation: a review," *Journal of Infrared, Millimeter, and Terahertz Waves*, vol. 41, no. 6, pp. 607–631, Jun 2020. [Online]. Available: https://doi.org/10.1007/s10762-020-00677-3

[16] N. Yu, P. Genevet, M. A. Kats, F. Aieta, J.-P. Tetienne, F. Capasso, and Z. Gaburro, "Light propagation with phase discontinuities: Generalized laws of reflection and refraction," *Science*, vol. 334, no. 6054, pp. 333–337, 2011. [Online]. Available: https://www.science.org/doi/abs/10.1126/science.1210713

[17] C. Pfeiffer and A. Grbic, "Metamaterial huygens' surfaces: Tailoring wave fronts with reflectionless sheets," *Phys. Rev. Lett.*, vol. 110, p. 197401, May 2013. [Online]. Available: https://link.aps.org/doi/10.1103/PhysRevLett.110.197401

[18] C. Yepes, M. Faenzi, S. Maci, and E. Martini, "Perfect non-specular reflection with polarization control by using a locally passive metasurface sheet on a grounded dielectric slab," *Applied Physics Letters*, vol. 118, no. 23, p. 231601, 06 2021.

[19] V. S. Asadchy, M. Albooyeh, S. N. Tcvetkova, A. Díaz-Rubio, Y. Ra'di, and S. A. Tretyakov, "Perfect control of reflection and refraction using spatially dispersive metasurfaces," *Phys. Rev. B*, vol. 94, p. 075142, Aug 2016. [Online]. Available: https://link.aps.org/doi/10.1103/PhysRevB.94.075142

[20] N. Mohammadi Estakhri and A. Alù, "Wave-front transformation with gradient metasurfaces," *Phys. Rev. X*, vol. 6, p. 041008, Oct 2016. [Online]. Available: https://link.aps.org/doi/10.1103/PhysRevX.6.041008

[21] J. P. S. Wong, A. Epstein, and G. V. Eleftheriades, "Reflectionless wide-angle refracting metasurfaces," *IEEE Antennas and Wireless Propagation Letters*, vol. 15, pp. 1293–1296, 2016.

[22] A. Díaz-Rubio, V. S. Asadchy, A. Elsakka, and S. A. Tretyakov, "From the generalized reflection law to the realization of perfect anomalous reflectors," *Science Advances*, vol. 3, no. 8, p. e1602714, 2017. [Online]. Available: https://www.science.org/doi/abs/10.1126/sciadv.1602714

[23] Y. Ra'di, D. L. Sounas, and A. Alù, "Metagratings: Beyond the limits of graded metasurfaces for wave front control," *Phys. Rev. Lett.*, vol. 119, p. 067404, Aug 2017. [Online]. Available: https://link.aps.org/doi/10.1103/PhysRevLett.119.067404

[24] L. Nama, Nilotpal, S. Bhattacharyya, and P. K. Jain, "A metasurface-based, ultrathin, dual-band, linear-to-circular, reflective polarization converter: Easing uplinking and downlinking for wireless communication," *IEEE Antennas and Propagation Magazine*, vol. 63, no. 4, pp. 100–110, 2021.

[25] H. F. Ma, G. Z. Wang, G. S. Kong, and T. J. Cui, "Broadband circular and linear polarization conversions realized by thin birefringent reflective metasurfaces," *Opt. Mater. Express*, vol. 4, no. 8, pp. 1717–1724, Aug 2014. [Online]. Available: https://opg.optica.org/ome/abstract.cfm?URI=ome-4-8-1717

[26] X. Ni, N. K. Emani, A. V. Kildishev, A. Boltasseva, and V. M. Shalaev, "Broadband light bending with plasmonic nanoantennas," *Science*, vol. 335, no. 6067, pp. 427–427, 2012. [Online]. Available: https://www.science.org/doi/abs/10.1126/science.1214686

[27] C. Pfeiffer and A. Grbic, "Millimeter-wave transmitarrays for wavefront and polarization control," *IEEE Transactions on Microwave Theory and Techniques*, vol. 61, no. 12, pp. 4407–4417, 2013.

[28] ——, "Metamaterial huygens' surfaces: Tailoring wave fronts with reflectionless sheets," *Phys. Rev. Lett.*, vol. 110, p. 197401, May 2013. [Online]. Available: https://link.aps.org/doi/10.1103/PhysRevLett.110.197401

[29] N. Mohammadi Estakhri and A. Alù, "Wave-front transformation with gradient metasurfaces," *Phys. Rev. X*, vol. 6, p. 041008, Oct 2016. [Online]. Available: https://link.aps.org/doi/10.1103/PhysRevX.6.041008

[30] S. Sun, Q. He, S. Xiao, Q. Xu, X. Li, and L. Zhou, "Gradient-index meta-surfaces as a bridge linking propagating waves and surface waves," *Nature Materials*, vol. 11, no. 5, pp. 426–431, May 2012.

[31] C. Qu, S. Xiao, S. Sun, Q. He, and L. Zhou, "A theoretical study on the conversion efficiencies of gradient meta-surfaces," *Europhysics Letters*, vol. 101, no. 5, p. 54002, mar 2013. [Online]. Available: https://dx.doi.org/10.1209/0295-5075/101/54002

[32] S. N. Tcvetkova, D.-H. Kwon, A. Díaz-Rubio, and S. A. Tretyakov, "Near-perfect conversion of a propagating plane wave into a surface wave using metasurfaces," *Phys. Rev. B*, vol. 97, p. 115447, Mar 2018.

[33] S. N. Tcvetkova, S. Maci, and S. A. Tretyakov, "Exact solution for conversion of surface waves to space waves by periodical impenetrable metasurfaces," *IEEE Transactions on Antennas and Propagation*, vol. 67, no. 5, pp. 3200–3207, 2019.

[34] S. N. Tcvetkova, E. Martini, S. A. Tretyakov, and S. Maci, "Perfect conversion of a tm surface wave into a tm leaky wave by an isotropic periodic metasurface printed on a grounded dielectric slab," *IEEE Transactions on Antennas and Propagation*, vol. 68, no. 8, pp. 6145–6153, 2020.

[35] S. Maci, G. Minatti, M. Casaletti, and M. Bosiljevac, "Metasurfing: Addressing waves on impenetrable metasurfaces," *IEEE Antennas and Wireless Propagation Letters*, vol. 10, pp. 1499–1502, 2011.

[36] E. Martini, M. Mencagli, D. González-Ovejero, and S. Maci, "Flat optics for surface waves," *IEEE Transactions on Antennas and Propagation*, vol. 64, no. 1, pp. 155–166, 2016.

[37] F. Elek, B. B. Tierney, and A. Grbic, "Synthesis of tensor impedance surfaces to control phase and power flow of guided waves," *IEEE Transactions on Antennas and Propagation*, vol. 63, no. 9, pp. 3956–3962, 2015.

[38] M. Bosiljevac, M. Casaletti, F. Caminita, Z. Sipus, and S. Maci, "Non-uniform metasurface luneburg lens antenna design," *IEEE Transactions on Antennas and Propagation*, vol. 60, no. 9, pp. 4065–4073, 2012.

[39] E. Martini and S. Maci, "Modulated metasurfaces for microwave field manipulation: Models, applications, and design procedures," *IEEE Journal of Microwaves*, vol. 2, no. 1, pp. 44–56, 2022.

[40] G. Minatti, M. Faenzi, E. Martini, F. Caminita, P. De Vita, D. González-Ovejero, M. Sabbadini, and S. Maci, "Modulated metasurface antennas for space: Synthesis, analysis and realizations," *IEEE Transactions on Antennas and Propagation*, vol. 63, no. 4, pp. 1288–1300, 2015.

[41] G. Minatti, F. Caminita, E. Martini, and S. Maci, "Flat optics for leaky-waves on modulated metasurfaces: Adiabatic floquet-wave analysis," *IEEE Transactions on Antennas and Propagation*, vol. 64, no. 9, pp. 3896–3906, 2016.

[42] G. Minatti, F. Caminita, E. Martini, M. Sabbadini, and S. Maci, "Synthesis of modulated-metasurface antennas with amplitude, phase, and polarization control," *IEEE Transactions on Antennas and Propagation*, vol. 64, no. 9, pp. 3907–3919, 2016.

[43] G. Minatti, E. Martini, and S. Maci, "Efficiency of metasurface antennas," *IEEE Transactions on Antennas and Propagation*, vol. 65, no. 4, pp. 1532–1541, 2017.

[44] F. Caminita, E. Martini, G. Minatti, M. Sabbadini, and S. Maci, "Low-profile dual-polarized isoflux antennas for space applications," *IEEE Transactions on Antennas and Propagation*, vol. 69, no. 6, pp. 3204–3213, 2021.

[45] M. Faenzi, N. Graziuso, E. Martini, and S. Maci, "Design methods for dual polarized metasurface antennas: Three simple approaches," *IEEE Antennas and Propagation Magazine*, vol. 64, no. 4, pp. 37–50, 2022.

[46] D. González-Ovejero, G. Minatti, G. Chattopadhyay, and S. Maci, "Multibeam by metasurface antennas," *IEEE Transactions on Antennas and Propagation*, vol. 65, no. 6, pp. 2923–2930, 2017.

[47] M. Teniou, H. Roussel, N. Capet, G.-P. Piau, and M. Casaletti, "Implementation of radiating aperture field distribution using tensorial metasurfaces," *IEEE Transactions on Antennas and Propagation*, vol. 65, no. 11, pp. 5895–5907, 2017.

[48] M. Bodehou, K. A. Khalifeh, S. N. Jha, and C. Craeye, "Direct numerical inversion methods for the design of surface wave-based metasurface antennas: Fundamentals, realizations, and perspectives," *IEEE Antennas and Propagation Magazine*, vol. 64, no. 4, pp. 24–36, 2022.

[49] B. H. Fong, J. S. Colburn, J. J. Ottusch, J. L. Visher, and D. F. Sievenpiper, "Scalar and tensor holographic artificial impedance surfaces," *IEEE Transactions on Antennas and Propagation*, vol. 58, no. 10, pp. 3212–3221, 2010.

[50] S. Pandi, C. A. Balanis, and C. R. Birtcher, "Design of scalar impedance holographic metasurfaces for antenna beam formation with desired polarization," *IEEE Transactions on Antennas and Propagation*, vol. 63, no. 7, pp. 3016–3024, 2015.

[51] A. Araghi, M. Khalily, P. Xiao, and R. Tafazolli, "Holographic-based leaky-wave structures: Transformation of guided waves to leaky waves," *IEEE Microwave Magazine*, vol. 22, no. 6, pp. 49–63, 2021.

[52] M. Di Renzo, A. Zappone, M. Debbah, M.-S. Alouini, C. Yuen, J. de Rosny, and S. Tretyakov, "Smart radio environments empowered by reconfigurable intelligent surfaces: How it works, state of research, and the road ahead," *IEEE Journal on Selected Areas in Communications*, vol. 38, no. 11, pp. 2450–2525, 2020.

[53] E. Basar, M. Di Renzo, J. De Rosny, M. Debbah, M.-S. Alouini, and R. Zhang, "Wireless communications through reconfigurable intelligent surfaces," *IEEE Access*, vol. 7, pp. 116 753–116 773, 2019.

[54] D. Dardari and D. Massari, "Using metaprisms for performance improvement in wireless communications," *IEEE Transactions on Wireless Communications*, vol. 20, no. 5, pp. 3295–3307, 2021.

[55] K.-K. Wong, K.-F. Tong, Z. Chu, and Y. Zhang, "A vision to smart radio environment: Surface wave communication superhighways," *IEEE Wireless Communications*, vol. 28, no. 1, pp. 112–119, 2021.

[56] A. Shojaeifard, K.-K. Wong, K.-F. Tong, Z. Chu, A. Mourad, A. Haghighat, I. Hemadeh, N. T. Nguyen, V. Tapio, and M. Juntti, "Mimo evolution beyond 5g through reconfigurable intelligent surfaces and fluid antenna systems," *Proceedings of the IEEE*, vol. 110, no. 9, pp. 1244–1265, 2022.

[57] A. Oliner and A. Hessel, "Guided waves on sinusoidally-modulated reactance surfaces," *IRE Transactions on Antennas and Propagation*, vol. 7, no. 5, pp. 201–208, 1959.

[58] A. M. Patel and A. Grbic, "A printed leaky-wave antenna based on a sinusoidally-modulated reactance surface," *IEEE Transactions on Antennas and Propagation*, vol. 59, no. 6, pp. 2087–2096, 2011.

[59] M. Faenzi, G. Minatti, D. González-Ovejero, F. Caminita, E. Martini, C. Della Giovampaola, and S. Maci, "Metasurface antennas: New models, applications and realizations," *Scientific reports*, vol. 9, no. 1, p. 10178, 2019.

[60] A. Hessel and A. Oliner, "A new theory of wood's anomalies on optical gratings," *Applied optics*, vol. 4, no. 10, pp. 1275–1297, 1965.

[61] Y. Fan, J. Wang, H. Ma, J. Zhang, D. Feng, M. Feng, and S. Qu, "In-plane feed antennas based on phase gradient metasurface," *IEEE Transactions on Antennas and Propagation*, vol. 64, no. 9, pp. 3760–3765, 2016.

[62] D.-H. Kwon and S. A. Tretyakov, "Arbitrary beam control using passive lossless metasurfaces enabled by orthogonally polarized custom surface waves," *Phys. Rev. B*, vol. 97, p. 035439, Jan 2018.

[63] D.-H. Kwon, "Modulated reactance surfaces for leaky-wave radiation based on complete aperture field synthesis," *IEEE Transactions on Antennas and Propagation*, vol. 68, no. 7, pp. 5463–5477, 2020.

[64] H. Lee and D.-H. Kwon, "Large and efficient unidirectional plane-wave–surface-wave metasurface couplers based on modulated reactance surfaces," *Phys. Rev. B*, vol. 103, p. 165142, Apr 2021.

[65] J. Budhu, L. Szymanski, and A. Grbic, "Design of planar and conformal, passive, lossless metasurfaces that beamform," *IEEE Journal of Microwaves*, vol. 2, no. 3, pp. 401–418, 2022.

[66] V. G. Ataloglou and G. V. Eleftheriades, "Arbitrary wave transformations with huygens' metasurfaces through surface-wave optimization," *IEEE Antennas and Wireless Propagation Letters*, vol. 20, no. 9, pp. 1750–1754, 2021.

[67] E. Abdo-Sánchez, M. Chen, A. Epstein, and G. V. Eleftheriades, "A leaky-wave antenna with controlled radiation using a bianisotropic huygens' metasurface," *IEEE Transactions on Antennas and Propagation*, vol. 67, no. 1, pp. 108–120, 2019.

[68] Zucchi, Marcello and Vernì, Francesco and Righero, Marco and Vecchi, Giuseppe, "Current Based Automated Design of Realizable Metasurface Antennas With Arbitrary Pattern Constraints," *IEEE Transactions on Antennas and Propagation*, vol. 71, no. 6, pp. 4888–4902, 2023.

[69] Giusti, Federico, Martini, Enrica, and Maci, Stefano, "Complete open-stopband suppression using sinusoidally modulated anisotropic metasurfaces," *IEEE Transactions on Antennas and Propagation*, 2023.

[70] M. Casaletti, "Guided waves on scalar and tensorial reactance surfaces modulated by periodic functions: A circuital approach," *IEEE Access*, vol. 7, pp. 68 823–68 836, 2019.

[71] A. Mehdipour, J. W. Wong, and G. V. Eleftheriades, "Beam-squinting reduction of leaky-wave antennas using huygens metasurfaces," *IEEE Transactions on Antennas and Propagation*, vol. 63, no. 3, pp. 978–992, 2015.

[72] H. Du, Z. Li, M. Chen, and J. Wang, "A broadband fixed-beam leaky-wave antenna," *IEEE Transactions on Antennas and Propagation*, vol. 71, no. 6, pp. 5434–5439, 2023.

[73] J. Chen, W. Yuan, C. Zhang, W. X. Tang, L. Wang, Q. Cheng, and T. J. Cui, "Wideband leaky-wave antennas loaded with gradient metasurface for fixed-beam radiations with customized tilting angles," *IEEE Transactions on Antennas and Propagation*, vol. 68, no. 1, pp. 161–170, 2020.

[74] G. Zhang, Q. Zhang, Y. Chen, and R. D. Murch, "High-scanning-rate and wide-angle leaky-wave antennas based on glide-symmetry Goubau line," *IEEE Transactions on Antennas and Propagation*, vol. 68, no. 4, pp. 2531–2540, 2020.

[75] K. Achouri and C. Caloz, "Space-Wave routing via surface waves using a metasurface system," *Scientific Reports*, vol. 8, no. 1, p. 7549, May 2018.

[76] D.-H. Kwon and S. A. Tretyakov, "Arbitrary beam control using passive lossless metasurfaces enabled by orthogonally polarized custom surface waves," *Phys. Rev. B*, vol. 97, p. 035439, Jan 2018.

[77] J. Budhu, "Near-perfect space-wave to surface-wave coupler enabled conformal space wave transporting metasurfaces," *IEEE Transactions on Antennas and Propagation*, vol. 72, no. 3, pp. 2540–2554, 2024.

[78] D. Sievenpiper, J. Schaffner, H. Song, R. Loo, and G. Tangonan, "Two-dimensional beam steering using an electrically tunable impedance surface," *IEEE Transactions on Antennas and Propagation*, vol. 51, no. 10, pp. 2713–2722, 2003.

[79] D. Sievenpiper, "Forward and backward leaky wave radiation with large effective aperture from an electronically tunable textured surface," *IEEE Transactions on Antennas and Propagation*, vol. 53, no. 1, pp. 236–247, 2005.

[80] C. Liu, F. Yang, S. Xu, and M. Li, "Reconfigurable metasurface: A systematic categorization and recent advances," *Electromagnetic Science*, vol. 1, no. 4, pp. 1–23, 2023.

[81] H.-H. Lv, Q.-L. Huang, J.-Q. Hou, and X.-W. Shi, "Fixed-frequency beam-steering leaky-wave antenna with switchable beam number," *IEEE Antennas Wireless Propag. Lett.*, vol. 19, no. 12, pp. 2077–2081, 2020.

[82] D. Kampouridou and A. Feresidis, "Tunable multibeam holographic metasurface antenna," *IEEE Antennas Wireless Propag. Lett.*, vol. 21, no. 11, pp. 2264–2267, 2022.

[83] A. H. Panaretos and D. H. Werner, "Leaky-wave antennas based on capacitively tuned modulated reactance surfaces," *IEEE Antennas Wireless Propag. Lett.*, vol. 15, pp. 678–681, 2016.

[84] D. Yang and S. Nam, "Frequency reconfigurable beam scanning squarely modulated reactance surface antenna with period and surface reactance control," *IEEE Access*, vol. 11, pp. 72 552–72 561, 2023.

[85] S. Paulotto, P. Baccarelli, F. Frezza, and D. R. Jackson, "A novel technique for open-stopband suppression in 1-D periodic printed leaky-wave antennas," *IEEE Transactions on Antennas and Propagation*, vol. 57, no. 7, pp. 1894–1906, 2009.

[86] M. Wang, H. F. Ma, H. C. Zhang, W. X. Tang, X. R. Zhang, and T. J. Cui, "Frequency-fixed beam-scanning leaky-wave antenna using electronically controllable corrugated microstrip line," *IEEE Trans. Antennas Propag.*, vol. 66, no. 9, pp. 4449–4457, 2018.

[87] T. Arshed, S. Maci, and E. Martini, "Enhancing reflecting intelligence surface using surface-wave engineering," in *2024 IEEE INC-USNC-URSI Radio Sci. Meeting (Joint with AP-S Symposium)*, 2024, pp. 138–138.

[88] A. B. Yakovlev, M. G. Silveirinha, O. Luukkonen, C. R. Simovski, I. S. Nefedov, and S. A. Tretyakov, "Characterization of surface-wave and leaky-wave propagation on wire-medium slabs and mushroom structures based on local and nonlocal homogenization models," *IEEE Trans. Microw. Theory Techn.*, vol. 57, no. 11, pp. 2700–2714, 2009.

[89] F. Caminita, E. Martini, and S. Maci, "Exact solution for anysotropic, periodically modulated boundary conditions excited by a surface wave," in *Proc. 9th Eur. Conf. Antennas Propag*, 2015.

[90] C. A. Balanis, *Antenna theory: analysis and design.* Fourth Edition, Hoboken, NJ, New Jersey: Wiley-Interscience, 2014.

[91] A. Chakraborty, B. Das, and G. Sanyal, "Determination of phase functions for a desired one-dimensional pattern," *IEEE Transactions on Antennas and Propagation*, vol. 29, no. 3, pp. 502–506, 1981.

[92] S. Maci and A. Cucini, "Fss-based ebg surfaces," in *Electromagnetic Metamaterials.* Hoboken, NJ, USA: John Wiley Sons, Ltd, 2006, ch. 13, pp. 351–376. [Online]. Available: https://onlinelibrary.wiley.com/doi/abs/10.1002/0471784192.ch13

[93] A. Norris and A. Osipov, "Far-field analysis of the malyuzhinets solution for plane and surface waves diffraction by an impedance wedge," *Wave Motion*, vol. 30, no. 1, pp. 69–89, 1999. [Online]. Available: https://www.sciencedirect.com/science/article/pii/S0165212598000493

[94] Y. Hua and T. Sarkar, "Generalized pencil-of-function method for extracting poles of an em system from its transient response," *IEEE Trans. Antennas Propag*, vol. 37, no. 2, pp. 229–234, 1989.

[95] J. García-Fernández, F. Caminita, C. Della Giovampaola, E. Martini, and S. Maci, "Reconfigurable metasurface antenna based on a single control signal," in *2023 IEEE Int. Symp. Antennas Propag. USNC-URSI Radio Sci. Meeting (USNC-URSI)*, 2023, pp. 629–630.